

STRENGTHENING OF AUTOCLAVED AERATED  
CONCRETE (AAC) MEMBERS USING BASALT FABRICS  
WITH AN INORGANIC MATRIX

by

ALAA A. ABD ALI

A dissertation submitted to the

School of Graduate Studies

Rutgers, The State University of New Jersey

In partial fulfillment of the requirements

For the degree of

Doctor of Philosophy

Graduate Program in Civil and Environmental Engineering

Written under the direction of

Husam Najm

And approved by

---

---

---

New Brunswick, New Jersey

MAY, 2018

## **ABSTRACT OF THE DISSERTATION**

Strengthening of Autoclaved Aerated Concrete (AAC) Members Using Basalt Fabrics  
with an Inorganic Matrix

By

ALAA A. ABD ALI

Dissertation Director:

HUSAM NAJM

Autoclaved Aerated Concrete (AAC) is a lightweight porous cementitious material, made from cement, fine silica sand, water, aluminum powder, and quicklime. AAC which has a density of 400 to 600 kg/m<sup>3</sup> can be considered as inorganic foam. This material is attractive for use as building elements due to their light weight as compared to normal concrete, fire resistance, ease of construction, energy efficiency, and sound insulation. In most of these applications, the precast structural elements made of AAC are subjected compression and bending forces. Since the bending strength of AAC is very low, its flexural capacity is improved by using steel wire mesh and small size rebars. However, due to the weak bond between AAC and steel wires and small bars and potential corrosion, needed strength increases cannot be obtained. This dissertation studies the use of basalt fabric composite for enhancing the flexural strength of AAC beams and panels. It also evaluates the effect of higher temperatures on the flexural strength of plain and strengthened AAC beams. The basalt fibers were applied to the AAC using an inorganic matrix to preserve the fire resistance capability of both AAC and the basalt fibers. An experimental investigation was conducted to evaluate the capability of an inorganic matrix to fully develop the strength

capacity of the basalt fiber in tension. Several series of strengthened AAC beams were tested in flexure following ASTM C 1452-06. Results show that the matrix is capable of providing the required bond between the basalt fibers and AAC. The strength capacity of basalt fibers was fully developed for tows and fabrics basalt reinforcement, and significant increase of flexural strength was achieved. The strengthening also reduced the loss of strength at elevated temperatures compared to plain beams. An analytical study was performed to predict the failure load in flexure. The failure load was predicted using three methods: elastic analysis, ultimate stress analysis, and non-linear analysis. The results of the analytical methods showed that the flexural strength of basalt fiber reinforced AAC beams can be reasonably predicted using the analytical models. The hand impregnation technique used to apply the matrix is conducive for easy field applications. The results show that the potential of significantly increasing the bending capacity of AAC panels making it a viable the system for practical applications. It is anticipated that the increase in strength will lead to longer spans and less thickness in exterior wall panels and roofing elements.

## **ACKNOWLEDGEMENTS**

To begin, I would like to thank God for gracing my life with opportunities, and for providing me the strength, and the ability during my journey of study. I would like to extend my gratitude to Dr. Husam Najm for his unlimited support and direction, not only on the academic level but the personal level as well. His door was open for me whenever I needed advice.

I would like to express my sincere gratitude to Prof. P.N Balaguru for the continuous support of my Ph.D. study and research, also for his immense knowledge. His kind guidance helped me in all the time of study and writing of this dissertation.

I would like to thank Prof. Christopher Uchrin and Prof. Yook- Kong Yong for taking time to be my dissertation committee, and for their valuable comments.

I am also grateful to HCED for providing the opportunity and the financial support that was needed to conduct my research.

I would like to especially thank Mr. Salah Hameed for his help during the research. Also Dr. Mohamed Arafa for his advises.

I would like to thank my friends for accepting nothing less than excellence from me. Last but not the least, I would like to thank my family: my Mom, sons, and to my brothers and sister for supporting me spiritually throughout writing this thesis and my life in general.

# Table of Contents

ABSTRACT OF THE DISSERTATION .....	ii
Acknowledgements.....	iv
Table of Figures .....	x
List of Tables .....	xvi
CHAPTER I.....	1
INTRODUCTION .....	1
1.1 Background.....	1
1.2 Scope of Research.....	2
1.3 Research Objectives.....	3
CHAPTER II.....	4
LITERATURE REVIEW .....	4
2.1 History of AAC.....	4
2.2 History of basalt fiber .....	5
2.3 History of inorganic matrix.....	7
2.4 Manufacturing of AAC.....	8
Stage1: Assembling the raw materials, weighed, and mix them .....	9
Stage2: Adding the desirable expansion agent .....	10
Stage3: Expansion of AAC, pre-curing, and cutting to certain sizes.....	12
Stage4: Final curing utilizing an autoclave.....	14

Stage5: Packaging in ballet and shipping .....	15
2.5 Practical application of AAC .....	16
2.6 Thermal Performance of AAC.....	18
CHAPTER III .....	24
properties of aac, basalt fibers, and the nano-inorganic matrix .....	24
3.1 MATERIAL PROPERTIES .....	24
3.2 Properties of autoclaved aerated concrete (AAC) .....	24
3.2.1 Material properties of AAC from the ACI523.4R-09.....	31
3.2.2 Strength reduction factors according to ACI523.4R-09 .....	34
3.2.3 Thermal and acoustical characteristics of AAC.....	37
3.3 Properties of basalt fibers.....	38
3.4 Properties of the matrix.....	43
3.4.1 Organic resins .....	43
3.4.2 Inorganic resin .....	46
CHAPTER IV .....	56
experimental PROGRAM.....	56
4.1 Phase I: (Plain and Reinforced AAC Beams).....	56
4.1.1 Specimens details and identification.....	56
4.1.2 Series Identification .....	57
4.1.3 Preparation of specimens and test set-up.....	60

4.1.4 Test specimens for the inorganic matrix .....	63
4.2 Phase II: Plain and Reinforced AAC Beams for Thermal Tests.....	65
4.2.1 Specimens details and identification.....	65
CHAPTER V .....	67
Phase I: test results and discussion .....	67
5.1 Tests of the flexural strength of the inorganic matrix.....	67
5.2 Compressive strength of the inorganic matrix .....	70
5.3 Tests of AAC Plain specimens .....	74
5.4 AAC Beam Specimens Strengthened with Basalt Tows .....	76
5.5 AAC Beam Specimens Strengthened with Basalt Fabrics .....	81
5.6 Ductility of AAC beams .....	89
CHAPTER VI.....	91
Phase II: THERMAL test results and discussion.....	91
6.1 Research significance for thermal performance .....	92
6.2 Preparation and Testing of Specimens.....	93
6.3 Furnace Specification and Heating Processes.....	96
6.4 Test set up and procedure for heated beams in flexure.....	99
6.5 Results and Discussion .....	102
6.5.1 Effect of high temperatures on the compressive strength.....	102
6.5.2 AAC Compressive Strength – Prediction Model.....	108

6.5.3 Effect of high temperatures on the flexural strength of AAC.....	110
6.5.4 AAC beams strengthened with basalt tows (Series S4BT).....	114
6.6 OBServations from thermal test .....	118
CHAPTER VII.....	120
7.1 ANALYTICAL MODELING .....	120
7.2 Flexural Behavior of FRP-Reinforced AAC beams .....	120
7.3 Method I - Linear stress distribution (elastic analysis).....	121
7.3.1 Assumptions for this approach: .....	121
7.3.2 Analysis equations for rectangular section of AAC strengthened with basalt FRP .....	121
7.4 Method II - Rectangular Stress Distribution (Whitney’s stress block approach) .....	127
7.4.1 Assumptions for this Method II.....	128
7.4.2 Analysis equations for rectangular section of AAC strengthened with basalt FRP .....	128
7.5 Non-linear Distribution Analysis – Method III .....	132
CHAPTER VIII .....	141
<b>8.1 CONCLUSIONS</b> .....	141
<b>8.2 RECOMMENDATIONS:</b> .....	144
references .....	144
APPENDIX A—DESIGN EXAMPLES .....	151

Example 1: Design of an AAC floor panel .....	153
Example 2: Design of an AAC shear wall .....	164
Example 3: Design of load-bearing vertical wall panel subjected to eccentric gravity and out-of-plane wind loads.....	168
APPENDIX B—DESIGN EXAMPLES .....	179
Example 1: Design of an AAC floor panel .....	179
Example 2: design of an AAC shear wall .....	191
Example 3: design of an AAC diaphragm .....	197
Example 4: Design of load-bearing vertical wall panel subjected to eccentric gravity and out-of-plane wind loads.....	205

## TABLE OF FIGURES

Figure 2. 1 Variable types of basalt fiber (sudaglass.com).....	6
Figure 2. 2 Manufacturing process to produce AAC blocks. (www.hebel-usa.com).....	9
Figure 2. 3 Autoclaved aerated concrete texture .....	11
Figure 2. 4 Forty times magnified Autoclaved aerated concrete showing the average diameter of the air voids. ....	12
Figure 2. 5 Autoclaved Aerated Concrete (AAC) mix in forms during the rising process (Tanner 2003).....	13
Figure 2. 6 Cutting AAC into desired shapes (Tanner 2003) .....	14
Figure 2. 7 Autoclaved aerated concrete forming machine (www.diytrade.com).....	15
Figure 2. 8 Shipping of AAC (Tanner 2003).....	16
Figure 2. 9 Variable samples of AAC elements (ACI 526).....	17
Figure 2. 10 Residual compressive strength of AAC (Ayudhya 2011). ....	21
Figure 2. 11 Residual splitting strength of AAC after heating (Ayudhya 2011).....	22
Figure 2. 12 b relative compressive and splitting strength of AAC specimens as a function of the elevated temperature (Tanaçan 2009). ....	22
Figure 2. 13 Strength ratio Vs. Temperature for Basalt, Carbon, and Glass fiber (Sim and Park 2005).....	23
Figure 2. 14 Effect of increasing temperature on the residual strength of basalt and glass fiber (Bhat et al. 2014) .....	23
Figure 3. 1 AAC used as an exterior non-bearing wall in Najaf, Iraq .....	26
Figure 3. 2 Compressive strength setup for AAC.....	27

Figure 3. 3 (a) The direction of rising of AAC specimens and applied a load of flexural,	
(b) compressive strength test. ....	28
Figure 3. 4 Basalt fabric used in the current study .....	42
Figure 3. 5 Maximum continuous-use of thermoplastic resins (Mazumdar, 2001).....	45
Figure 3. 6 Time to flashover for different resin systems (Lyon, 1997).....	47
Figure 3. 7 Residual warp direction flexural strength of crossply laminates after thermal exposure (Lyon, 1997) .....	48
Figure 3. 8 Peak Loads after wet-dry exposure (Garon 2000).....	50
Figure 3. 9 Peak Loads after Scaling Exposure (Garon 2000) .....	50
Figure 3. 10 Polysialate as graffiti proof coating (Nazier 2004) .....	53
Figure 3. 11 Applying the inorganic matrix using hand lay-up technique .....	54
Figure 4. 1 Strengthening of AAC beam end areas. ....	60
Figure 4. 2 Preparing and applying the inorganic matrix for AAC beams .....	61
Figure 4. 3 Flexural Test Setup.....	63
Figure 4. 4 Cut the concrete beams in the middle.....	64
Figure 5. 1 Re-attached the cut concrete beams using inorganic matrix. ....	68
Figure 5. 2 Flexural test of the concrete beams attached to the inorganic matrix. ....	68
Figure 5. 3 Failure mode in cut attached faces concrete beams.....	69
Figure 5. 4 Failure mode in cast attached faces concrete beams. ....	69
Figure 5. 5 Preparing the inorganic matrix cubes. ....	71
Figure 5. 6 testing of inorganic cubes in compressive machine .....	72
Figure 5. 7 Compressive strength for different mixes (Wongpa 2010) .....	73

Figure 5. 8 Flexural behavior of Plain specimens.....	74
Figure 5. 9 Load versus deflection of AAC beams with basalt tows.....	77
Figure 5. 10 Failure of AAC beams with five tows.....	79
Figure 5. 11 Failure of AAC beams with five tows and shear enhancement.....	80
Figure 5. 12 Load versus deflection of specimens reinforced with 0.5 in wide basalt fabric and specimens reinforced with five basalt tows. ....	82
Figure 5. 13 Shear failure of the specimen without shear enhancement. ....	83
Figure 5. 14 Support crushing of specimen without U-wrap.....	84
Figure 5. 15 Load versus deflection of AAC beams reinforced with 2 inches basalt fabric. ....	85
Figure 5. 16 Load versus deflection of AAC beams reinforced with 2 inches wide basalt fabric. ....	86
Figure 5. 17 Load deflection of 4 inches X 6 inches AAC beams reinforced with 2 inches and 3.5 inches basalt fabric.....	87
Figure 5. 18 Shear failure of AAC beams reinforced with two layers of basalt fabric 3.5 inches wide.....	88
Figure 5. 19 Load deflection curve for specimens with 4 inches fabric width.....	89
Figure 6. 1 Furnace used in this experiment.....	97
Figure 6. 2 Heating performance rate for the furnace used to heated the specimens .....	98
Figure 6. 3 Specimen dimension and load application for AAC Series S3P and S4BT. ....	100
Figure 6. 4 Specimen dimension and load application for AAC Series S1P and S2CP. ....	101
Figure 6. 5 Variation of the relative compressive strength of AAC as a function of temperature from this study and other studies .....	105

Figure 6. 6 20x magnifying picture for AAC cubes at different temperatures .....	106
Figure 6. 7 (a). AAC cubes in the furnace at 1000 °C before being tested in compression .....	107
Figure 6. 8 Spalling and cracking in cubes after heated for 1000 °C and cool by air.....	107
Figure 6. 9 Variation of compressive strength with Temperature for AAC .....	109
Figure 6. 10 Load-deflection curves for plain AAC beams series S3P .....	113
Figure 6. 11 Variation of flexural strength with temperature for series (S1P, S2CP, and S3P).....	114
Figure 6. 12 Variation in failure load of plain and basalt reinforced AAC beams in flexure as a function of temperature.....	116
Figure 6. 13 Load versus deflection for reinforced AAC beams as a function of temperature .....	117
Figure 7. 1 Linear stress distribution approach.....	122
Figure 7. 2. Whitney’s block for rectangular distribution .....	129
Figure 7.3. Stress-strain curve of AAC used in the nonlinear analysis (Desayi 1964)..	133
Figure 7.4. stress strain curves for normal concrete .....	138
Figure 7.5. Compressive stress versus strain for Shipment 1 (Tanner 2003). .....	139
Figure 7. 6. Compressive stress versus strain for Contec Shipment 2 (Tanner 2003)....	139
Figure 7.7. Compressive stress versus strain for Babb Shipment 3 (Cancino 2003).....	140
Figure A. 1 Elevation of floor panel .....	153
Figure A. 2 Cross section for AAC panel.....	154

Figure A. 3 Cross section of panel to calculate uncracked transformed moment of inertia using one layer of basalt fiber.....	156
Figure A. 4 Cracked transformed section of the floor panel.....	158
Figure A. 5 Free body diagram of the floor panel. ....	162
Figure A. 6 AAC shear wall elevation.....	164
Figure A. 7 Plan view of the AAC shear wall with basalt fiber enhancement .....	165
Figure A. 8 Section of AAC bearing wall.....	169
Figure A. 9 Force interaction for 8 inches AAC bearing wall with one layer of basalt fiber as reinforcement.....	172
Figure A. 10 Horizontal section through 1 ft wide strip of uncracked AAC bearing wall.....	175
Figure A. 11 Horizontal section through 1 ft wide strip of cracked AAC bearing wall.	176
Figure B. 1 Elevation of the floor panel. ....	180
Figure B. 2 Cross section of the panel. ....	180
Figure B. 3 Cross section of the panel to calculate the uncracked transformed moment of inertia using two layers of steel. Actual thickness, h, is 9.5 in. ....	182
Figure B. 4 Cracked, transformed section of the floor panel.....	183
Figure B. 5 Floor panel divided into end zones ( $l_n/6$ from support) and intermediate zones ( $l_n/3$ from centerline).....	187
Figure B. 6 Free-body diagram of the floor panel. Only tensile steel showed for clarity .....	188
Figure B. 7 the Free body of the corner of AAC roof panel at support. ....	190
Figure B. 8 AAC shear wall elevation. ....	192

Figure B. 9 Plan view of AAC shear wall and flexural reinforcement. ....	193
Figure B. 10 Plan view of a wall with ACI nomenclature, a free-body diagram of the wall, and strain distribution. Wall is rotated for ease of reading. ....	193
Figure B. 11 Plan view of the diaphragm. ....	198
Figure B. 12 Section through short dimension of the diaphragm. ....	198
Figure B. 13 Section through long dimension of the diaphragm. ....	199
Figure B. 14 Section through the grouted key .....	200
Figure B. 15 Detail of joint between panel and bond beam.....	201
Figure B. 16 Truss model for the diaphragm. ....	202
Figure B. 17 Equilibrium of Nodes 1 and 2 in truss model. ....	202
Figure B. 18 Equilibrium of Nodes 3 and 4 in truss model. ....	203
Figure B. 19 Section of AAC bearing wall to be designed.....	206
Figure B. 20 force interaction for 8 in. nominal AAC is bearing wall with two 0.236 in. (6 mm) diameter bars as longitudinal reinforcement. ....	208
Figure B. 21 Horizontal section through 1 ft wide strip of uncracked AAC bearing wall. ....	210
Figure B. 22 Horizontal section through 1 ft wide strip of cracked AAC bearing wall. ....	211

## LIST OF TABLES

Table 3. 1 ASTM Specification C1693-11 Autoclaved Aerated Concrete (ASTM, 2011)	25
Table 3. 2 Test results for compressive tests of AAC cubs.	29
Table 3. 3 Ratios between measured modulus of rupture at ASTM C1386 density and splitting tensile strength* (Fouad and Dembrowski 2005)	33
Table 3. 4 Fire rating for walls, panels, and Roofs (www.aerconaac.com)	38
Table 3. 5 Comparative technical characteristics of a filament made from E-glass, basalt, and Silica (www.sudaglass.com).	40
Table 3. 6 Heat release test results for OSU (Giancaspro, 2004)	44
Table 3. 7 Typical thermosetting resin (Mazumdar 2001)	44
Table 3. 8 Typical thermoplastic resin (Mazumdar, 2001)	46
Table 3. 9 Heat release test results for OSU (Giancaspro 2004)	52
Table 3. 10 NBS smoke test results (Giancaspro 2004)	52
Table 4. 1 Phase I specimen types and geometry	59
Table 4. 2 Summary of specimen details and geometry for Phase II	66
Table 5. 1 Test results of the plain AAC beams with 18 inches span	76
Table 5. 2 Test results of the plain AAC beams with 12 inches span	76
Table 5. 3 Summery of the test results of AAC beam specimens	90
Table 6. 1 Summary of the properties of the various test series in the experimental program	95
Table 6. 2 Heating process and total holding time in furnace	98

Table 6. 3 Summary of the test results for the compressive strength for this study and from previous studies .....	105
Table 6. 4 Variation of flexural strength with temperature .....	112
Table 6. 5 Comparison between plain and reinforced AAC beams in flexure. ....	116
Table 7. 1 Comparison of maximum loads from test data and from elastic analysis for different series of the AAC beams in flexure. ....	126
Table 7. 2. Comparison of maximum loads from test data and from the strength analysis (Method II ) for different series of the AAC beams in flexure .....	131
Table 7.3. Comparison of maximum loads from test data and from non-linear analysis (Method III) for different series of the AAC beams in flexure.....	137
Table 7. 4. Difference in maximum load from analytical prediction and lab tests for the three analytical methods.....	138
Table A. 1 Values for interaction diagram.....	173
Table B. 1 Values for interaction diagram.....	209

# CHAPTER I

## INTRODUCTION

### 1.1 Background

Autoclaved Aerated Concrete (AAC) is an ultra-lightweight cementitious material with a low density approximately three to five times less than normal concrete. The extra low density is achieved by the formation of non-connecting, macroscopic cells distributed uniformly within the AAC material. Chemical reactions between the aluminum powder and the alkaline slurry produce hydrogen gas bubbles that are kept in the matrix and subsequently increase its volume (Wittmann 1983). This material's use has grown widely since it was developed first time in Sweden in 1929. Due to its significant contribution to structure dead load reduction, AAC has widely accepted to use as main structural elements like lintels and floor panels by reinforcing it using wire mesh. On the other hand, its low compressive strength (about 300 to 1100 psi), and low shear strengths, however, limit its spans and load carrying capacity. A detailed study of the characteristics of AAC material like porosity, pore sizes, and other characteristics was done by Shi and Fouad (2005). Due to its high porosity, the AAC is not a durable material. However, AAC's durability can be enhanced by protecting it with natural stone, veneer, or siding. Recently, in the United States, there have been many studies that focused on the use of AAC elements as structural members. Nasim Uddin et al. (2007) examined the behavior of combined AAC as a sandwich panel with the carbon fiber reinforced polymer (CFRP) using vacuum-assisted resin transfer modeling. The researchers were able to obtain a 50 % increase in flexural capacity and 300% increase in shear capacity. Memari et al. (2010) used glass fiber reinforced polymer (GFRP) instead of CFRP to enhance the strength capacity of the AAC

panels. These researchers reported a 70% increase in the flexural capacity. In these studies, fire resistance of the panels was compromised because of the organic polymers used for adhesion. Tanner (2003) developed a comprehensive testing program consist of two phases. The first phase of that testing program was intended to determine the behavior of AAC shear walls subjected to reversed cyclic lateral loads, and The second phase of the testing program involved the design, construction, and testing, under reversed cyclic lateral loads, of a full-scale, two-story AAC assemblage specimen.

## **1.2 Scope of Research**

The primary aim of this research is to investigate the use of basalt fabrics and tows as tension and shear reinforcement to enhance the strength of AAC elements and improve their performance. An inorganic nano-composite material was used to achieve a bond between the AAC beams and the basalt fabrics and tows. Both basalt fibers and the matrix have superior fire resistance compared to AAC. The effectiveness of the inorganic binder to bond the basalt fibers to AAC, as well as load transfer between the fibers and the core, will be evaluated. An experimental as well as an analytical investigation of the contribution of fiber reinforcement to strength, stiffness, and thermal resistance of AAC will be the main focus of this research.

### **1.3 Research Objectives**

The main objectives of this research are the following:

1. Understanding the behavior of AAC under applied loads.
2. Perform an experimental study to evaluate the effectiveness of basalt fibers to strengthen AAC beams in bending as well as their effectiveness at higher temperatures.
3. Evaluate the use of an inorganic matrix to bond the fiber material to AAC
4. Use analytical methods to predict the flexural response of the fiber-reinforced AAC beams.
5. Develop design guidelines for design for AAC panels strengthened with basalt fibers.

## CHAPTER II

### LITERATURE REVIEW

#### 2.1 History of AAC

The use of autoclaved aerated concrete (AAC) as a construction material is not far away in the history timeline as the other masonry construction materials like stone and CMU. People used the masonry as the main construction material in early civilizations in Mesopotamia and Egypt while the AAC promoted in the nineteenth century. The applications of using AAC were same as masonry except the AAC was lighter in term of the weight. The earliest specification, developed by American society for testing and material international (ASTM international), for the design of AAC was just released in 1998. This specification was including the structural design of AAC bearing walls under load and without load.

In Europe, the first patent for the manufacture of AAC was granted in 1929 to a Swedish architect called Johann Erickson. He got his patent to use aluminum powder in moist cured, and autoclaved concretes. He first discovered AAC in 1923 almost accidentally while he was working on some aerated concrete samples, he placed them in an autoclaved to speed the curing process. In 1942, factory production of AAC started in Sweden; then due to its unique properties like light weight and thermal isolation, it expanded to other countries in Western Europe soon after like Denmark in 1937, Germany in 1942, and United Kingdom in 1951. In the present, there is about 100 production site in 18 European countries producing around 17 million cubic yards of AAC per year. To promote the interests of producers in Europe, the European Autoclaved Aerated Concrete Association (EAACA) was created in 1988.

In the United States, AAC recently being come in the early 1990's. In the southeast of the country the AAC production was started, then it has slowly been spreading in its use to other parts of the United States. In the present, there is two sites produce the AAC. The first producer is Xella Aircrete North America Inc. (Hebel) which has plants located in Texas, Georgia, and Mexico as well. The second one is AERCON Company which has a plant in Haines City, Florida. Currently, there are no available data about the exact annual production of AAC in the United States, but the production capacity of the largest North American producer of AAC (Hebel's Georgia Facility) is approximately 2.7 billion cubic feet per year ([www.xella-usa.com](http://www.xella-usa.com)). To promote the use of AAC in the United States, the autoclaved aerated concrete products association (AACPA) was established.

## **2.2 History of basalt fiber**

The first attempts to produce basalt filament from the melt were made in the United States in 1932. During the World War II, and continuing into the 1950s, research in several countries advanced the science and technology of basalt fiber manufacture, but without any commercial products were produced. In the past few decades, most of the research and the commercialization of basalt fiber products has occurred in Russia and the former republic of the Soviet Union.

The use of basalt fiber first was extensively in defense and aeronautical applications, but after knowing the excellent performance of this material in term of strength, heat resistance, high modulus, and resistance to chemical attack, these properties make this material promising to use in many composite applications. In construction and infrastructure applications, the researchers found out this material is attractive to use as replacing of steel bars or strengthening and upgrading existed concrete structures. In present days, the basalt

fiber is available in many shapes like bars, roving, fabric, and wide variety types of fabric as shown in Figure 2.1.



**Figure 2. 1 Variable types of basalt fiber (sudaglass.com)**

### **2.3 History of the inorganic matrix**

In the 1970's a French scientist, Joseph Davidovits developed a new class of inorganic "plastics" in response to several fire outbreaks in France (Davidovits 1979). The material that he found was a certain group of inorganic mineral compositions that shared similar hydrothermal conditions that control the synthesis of organic phenolic plastics such as high pH values, concentrated alkali, thin set at atmospheric pressure and temperatures below 300°F.

The new material family of materials was given the name Geopolymer because of the geologic origin of the main components and how the materials share properties with other naturally occurring minerals such as feldspathoids, feldspars, and zeolites. These properties include thermal stability, smooth surfaces, and hardness, weather resistant and high temperature resistant up to over 2000°F. Unlike the naturally occurring minerals, the Geopolymers are polymers meaning they can be transformed, tooled, and molded. They are created in a similar manner to thermosetting organic resins and cement by polycondensation. The inorganic polymer can be formulated with or without the use of additional performance enhancing fillers or reinforcement. Applications of the material are found in automobile and aerospace industries, civil engineering and plastics/ceramics.

## 2.4 MANUFACTURING OF AAC

Autoclaved aerated concrete (AAC) is made purely from natural raw materials. However, it is composed of Portland cement, quicklime, water, and finely ground sand. The sand can be replaced partially, or totally by fly ash (Clusid 1999). These materials used to manufacture the AAC should pass through many processes to get the AAC blocks with the desirable sizes as shown in Figure 2.2. These processes can be elaborated in five stages:

- Stage1: Assembling the raw materials, weighed, and mix them.
- Stage2: Adding the desirable expansion agent.
- Stage3: Expansion of AAC, pre-curing, and cutting to certain sizes.
- Stage4: Final curing is utilizing an autoclave.
- Stage5: Packaging in ballet and shipping.

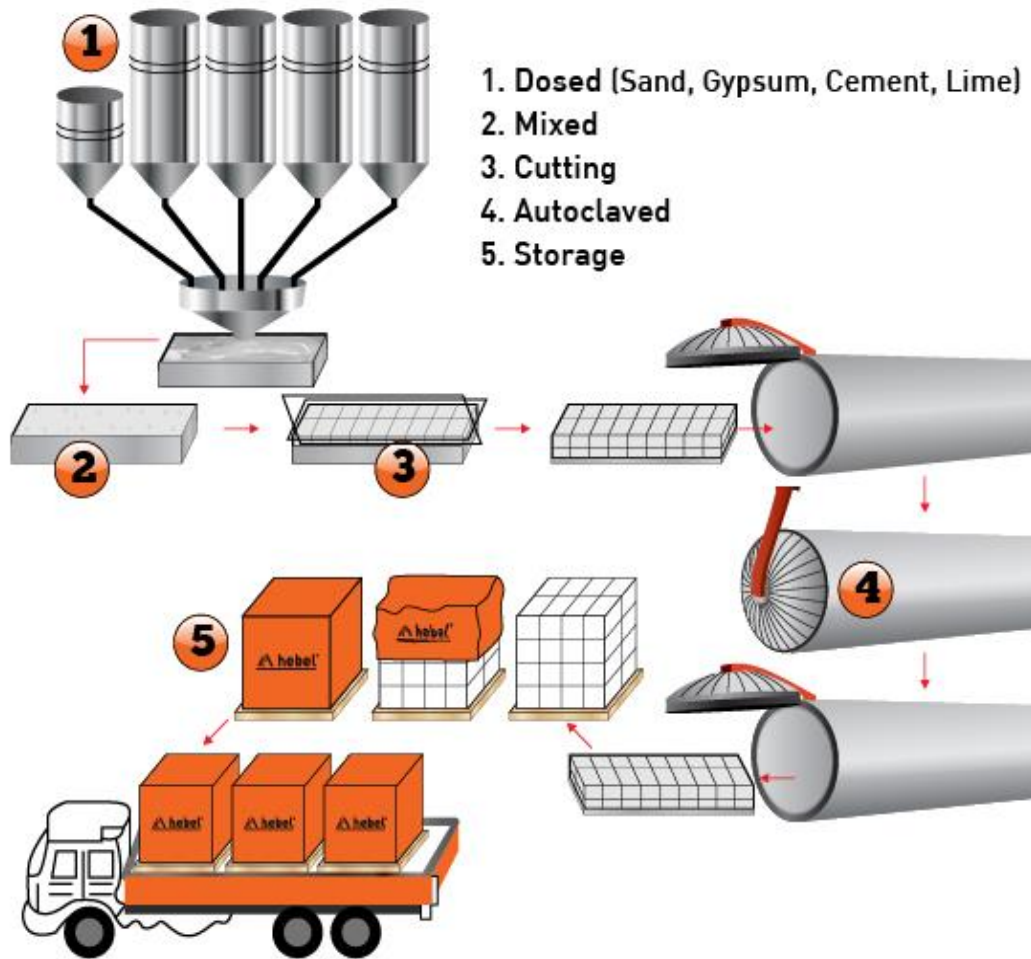


Figure 2. 2 Manufacturing process to produce AAC blocks. ([www.hebel-usa.com](http://www.hebel-usa.com))

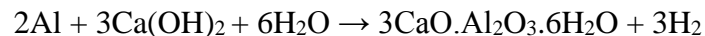
***Stage1: Assembling the raw materials, weighed, and mix them***

The processes of producing AAC blocks start with the raw materials of silica, cement, lime, and water. The silica, which is used for the aggregate, is made from finely ground quartz. Fine sand can be used in place of silica. Also, fly ash, slag, or mine tailings which are the ground up remains from mining operations, can be used as aggregate in combination with the silica. These materials are the fine aggregate of the concrete mix. The aggregate needs

to be a fine gradation, not a coarse or large material because a larger aggregate interferes with the internal structure created by the microscopic bubbles produced in Stage 2. For that, the aggregate is ground to the required fineness in a ball mill. Portland cement is used, just as it is used in normal concrete mixes. Portland cement is the binding agent which holds the aggregate together. It reacts with water in a process called hydration and then hardens, bonding all the aggregates together to form a solid material. All these are mixed with water to form the base AAC mixture. The raw components are then mixed together with water in a large container to form a slurry.

***Stage 2: Adding the desirable expansion agent***

An expansion agent is added to the concrete mix (slurry) as it is poured into forms to increase its volume. In autoclaved aerated concrete, the expansion agent that is used is aluminum powder or paste. The aluminum reacts with the calcium hydroxide and water in the mixture creating millions of tiny hydrogen bubbles as shown in Figure 2.3. In Figure 2.4, the air voids were magnified 40 times, and the diameter of these bubbles was measured using a digital microscope, and they were ranging between (0.1 – 0.3) mm. In general, this process can be shown by the following chemical equation (Pytlik & Saxena 1992):



Aluminum Powder + Hydrated Lime → Tricalcium Hydrate + Hydrogen

The hydrogen gas that is formed in this process bubbles up out of the mixture and is replaced by air (Wittmann 1983). The hydrogen, which is known as a lighter gas, rises and is replaced by air which is a denser gas that gets into the mix as the hydrogen foams up out of the material. The aluminum expansion agent is thoroughly mixed into the batch so that

it is evenly distributed during the mixing process. The creation of hydrogen bubbles causes the mix to expand, increasing the volume of the mixture approximately two to five times its normal volume. The volume inside the form increase is dependent upon the amount of aluminum powder/paste that is already introduced to react with the calcium hydroxide in the mixture. The less expansion that is induced will produce a higher strength material (more dense) versus the maximum amount of expansion induced, which produces a lower strength material (less dense). The microscopic voids created by the gas bubbles give AAC its light weight and other beneficial material properties, such as its high thermal resistance properties.



**Figure 2. 3 Autoclaved aerated concrete texture**

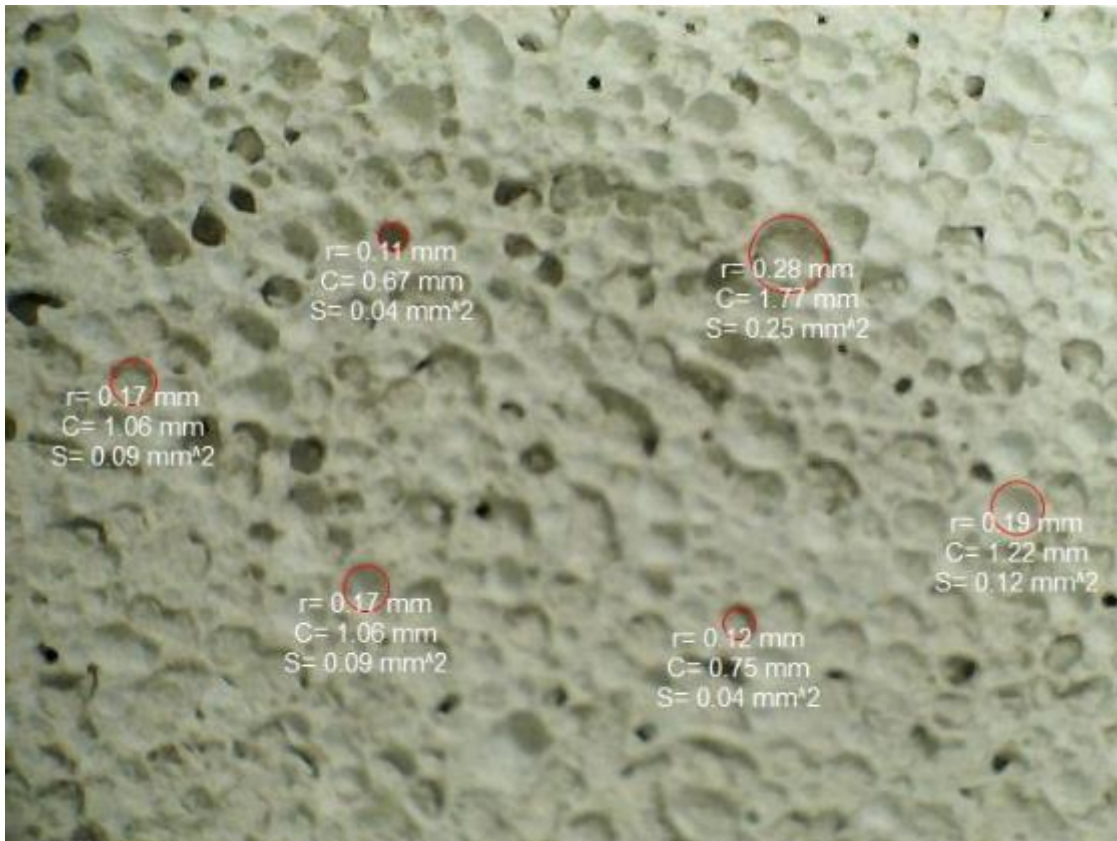


**Figure 2. 4 Forty times magnified Autoclaved aerated concrete showing the average diameter of the air voids.**

*Stage3: Expansion of AAC, pre-curing, and cutting to certain sizes*

After the addition of the expansion agent, the mix is poured into metal molds where it is allowed to expand as shown in Figure 2.5. If a plank or panel is being cast, then steel reinforcement is placed in the mold prior to pouring the mix into the mold. The steel reinforcement is used to give tension strength to the lightweight concrete material. However, they can use as floor panel or lintel. When the mix is poured into the forms, commonly 20 feet x 4 feet x 2 feet thick (Pytlik & Saxena 1992), it first expands and then is allowed to pre-cure for several hours. The pre-curing stage is to allow enough time such that the block can maintain its shape outside of its mold. The pre-cured block can then be cut, utilizing a device that uses thin wires, into the desired shapes as shown in Figure 2.6.

Standard AAC masonry can be found with nominal dimensions of 8 inches deep by 24 inches long with a varying thickness of 4 inches to 12 inches. The larger blocks are cut into solid masonry blocks similar to concrete masonry units (CMUs). Unlike CMU, AAC masonry units are cut from the larger block rather than being formed individually. The production of a plank, which can have reinforcement cast in, is not cut from a large block. The waste that is produced from cuttings or any leftover bits can be reused in the original mixture as aggregate after being finely ground.



**Figure 2. 5 Autoclaved Aerated Concrete (AAC) mix in forms during the rising process (Tanner 2003)**

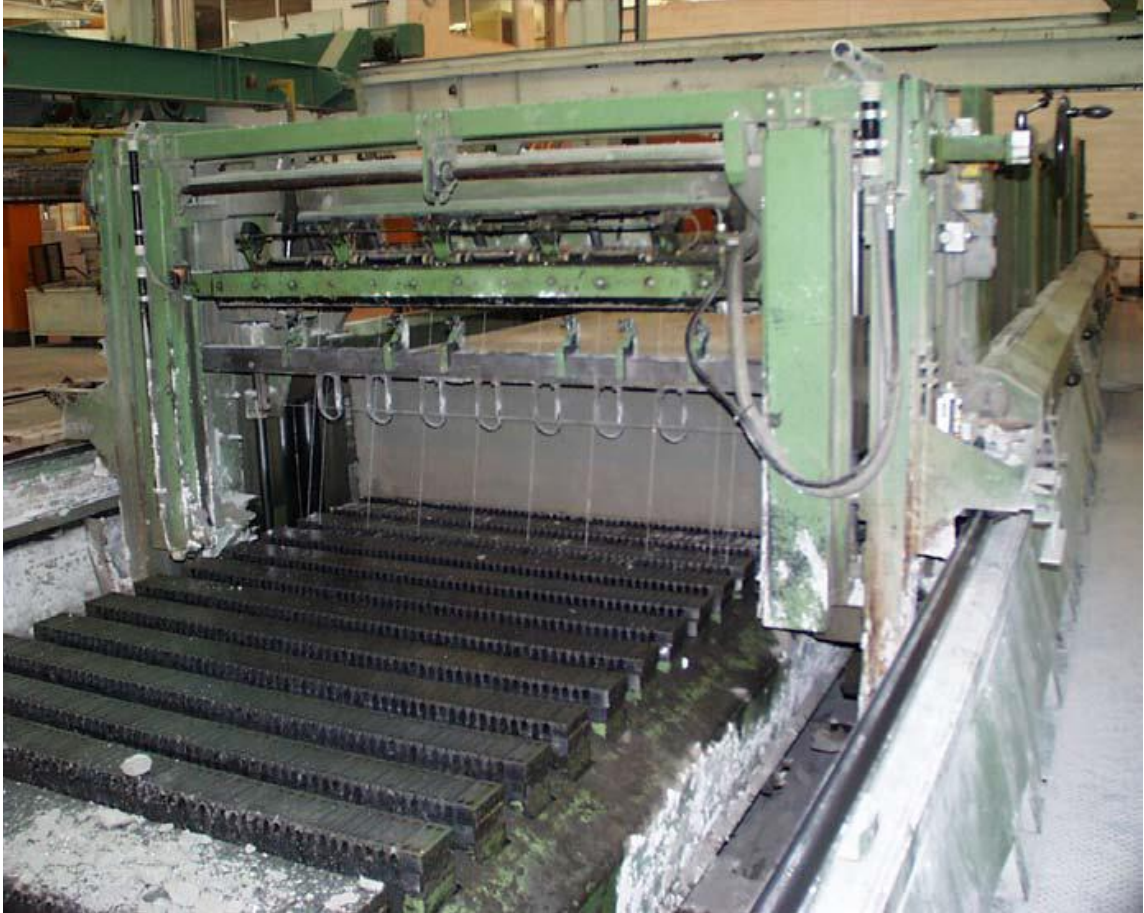


**Figure 2. 6 Cutting AAC into desired shapes (Tanner 2003)**

***Stage4: Final curing utilizing an autoclave***

In this stage, the AAC blocks are subjected to a strong pressurized heated steam to cure the autoclaved aerated concrete as shown in Figure 2.7. In fact, curing is the process by which the concrete mixture hardens through hydration (chemical process between cement and water), with the autoclave the blocks are cured with steam at high pressures. The pressure, temperature, and moisture are closely controlled for the twelve hours of curing time. The monitoring of proper pressure, temperature, and moisture allows for the optimum conditions for which hydration can occur. During this process, the autoclave is heated to

374 degrees Fahrenheit and pressurized to 12 atmospheres of pressure, “quartz sand reacts with calcium hydroxide and evolves to calcium silica hydrate which accounts for the material's physical strength properties (Wittmann 1983)”.



**Figure 2. 7 Autoclaved aerated concrete forming machine (www.diytrade.com)**

***Stage5: Packaging in ballet and shipping***

After the curing time is finished, which is typically takes approximately twelve hours (Pytlik & Saxena 1992), the cured blocks are removed from the autoclave, packaged, and shipped. Figure 2.8 shows AAC being transported to a construction site. The various literature states that after AAC is autoclaved it can be immediately shipped and used for construction, it is assumed that the cooling step is not expressed as a period of time where the material is set aside for the express purpose to cool down, but as the period of time

when the material is being packaged. At this point in the process, the autoclaved aerated concrete units are ready for use in the construction process. Currently, in the United States, the greatest production and use of AAC is in the southeast.



**Figure 2. 8 Shipping of AAC (Tanner 2003)**

## **2.5 PRACTICAL APPLICATION OF AAC**

Because of its unique properties in terms of lightweight, ease of cut, forming in different shapes, and thermal isolation, the AAC material has a wide variety use is construction field as shown in Figure2.9. Tradition elements include masonry-type units (blocks), floor panels, roof panels, wall panels, lintels, beams. Non-traditional elements include special shapes such as arches. These elements can be used in many applications including residential, commercial and industrial construction. Reinforced wall panels can be used as cladding systems as well as loadbearing and non-loadbearing interior and exterior wall systems. Reinforced floor and roof panels can be efficiently used to provide the horizontal diaphragm system while supporting the necessary gravity loads.

The standard units in AAC structural systems are AAC shear walls and floor diaphragms. Shear walls may be constructed of modular blocks or panels oriented horizontally or vertically. Modular blocks are 8 inches in height and are 24 inches long. Wall panels are 24 inches in height and may have lengths up to 240 inches. The thickness of blocks and panels is variable, with a common thickness of 8 inches to 10 inches. Floor panels have a width of 24 inches and are produced in lengths up to 240 inches. The height of floor and roof panels is variable, with a common thickness of 8 inches to 10 inches.



**Figure 2.9 Variable samples of AAC elements (ACI 526).**

Welded wire reinforcement in AAC panels consists of longitudinal wires, parallel to the axis of the panel and transverse, or cross-wires. The longitudinal wire is generally 0.3 inches in diameter and cross-wires are generally 0.2 inches in diameter. Typical spacing for longitudinal wires in a heavily reinforced mesh is 3 inch, while typical spacing for longitudinal wires in a lightly reinforced mesh is 10 inches. Typical spacing for cross-wires is 20 inches in either mesh.

Individual AAC units are bonded together by thin-bed mortar. Joints are approximately 1/32 in. to 1/8 in. thick. Thin-bed mortar is a mix of Portland cement, fine silica sand, polymers such as latex or vinyl ester, and admixtures such as water-retention admixtures. The compressive strength of the thin-bed mortar is greater than that of the AAC itself. The compressive strength of the thin-bed mortar is approximately 2 ksi, which is greater than the maximum compressive strength of the AAC.

## **2.6 THERMAL PERFORMANCE OF AAC**

The light weight Autoclaved Aerated Concrete (AAC) offers kind of specific, feasible properties in perspective of sustainable development in the field of building industry. The structural design and mechanical properties of the Autoclaved Aerated Concrete (AAC) influence thermal performance for buildings. The technologies that have been used to produce the AAC are energy efficient and it has less consumption for the raw material as a compare to the other technologies that produce other construction material, which can be assigned to extra low density and environmentally friendly formula of AAC and waste free for the row material (Domingo 2008). In previous studies, increasing the temperature gradually from room temperature up to 1000 C° with degrading the compressive strength

and splitting strength dramatically Figure 2.10 and Figure 2.11 respectively. Although, both the compressive and splitting strength were increased slightly up to 100 C°, they lost about 85% from the original strength (Ayudhya 2011). In an experiment, reported that the flexural strength of lightweight concrete and other mechanical properties were start deteriorated at 150 C°. Even though the reduction in strength at temperatures between (150-300) C° was not considerable, the other concrete mixture was continued losing compressive strength significantly after 300°C, however, the heating duration has not affected the reduction in strength (Bingol, A. F., & Gul, R. 2004). In another study, thermal insulation and fire resistant have been tested with different levels of moisture content, however, the AAC specimens losses their mass and mechanical properties for the temperature of 500 C° and above (Keyvani 2014). In a different study, the unstressed residual and unstressed strength of AAC examined at an elevated temperature up to 965 C° and considering the effect of different cooling systems (in the air and water). The reported results showed the volume of the AAC slightly increased at low temperature due to the thermal expansion of AAC; then it shrinks depending on the heating level. The reduction in volume was about 10 % from the original volume. Moreover, the strength reduced gradually with increasing the temperature, and if the cooling system effect is disregarded, the temperature rise will not have a significant effect on the strength of the AAC for approximately up to 700–800 C° Figure 2.12 (Tanaçan 2009). Investigation of the amount of deterioration in the flexural strength of AAC beams subjected to high temperature events can be used as a guide to judge whether the AAC structures should be retrofitted or replaced. Moreover, based on the available literature, there were few experimental investigations related to the flexural strength of AAC material at elevated temperatures.

The behavior of basalt fibers and its strength at high temperature should be known for the safe design and retrofit of AAC beams. Studies conducted on the performance of basalt fibers under increased temperatures showed that basalt fibers are resistant to high temperatures and the loss of strength and stiffness is small up to 400 °C. Sim and Park (2005) investigated the effects of high temperatures on the performance of basalt fibers. Their results showed that the basalt fibers kept about 90 % of the initial tensile strength values after exposure to 600 °C for 2 hours Figure 2.13. Other studies (Bhat et al. 2014) showed that basalt fibers lose most of its tensile strength at 500 °C. The test results in this study showed significant loss of strength of the basalt fibers above 400 °C. Hamed et al. (2010), studied the lateral out-of-plane structural behavior of AAC walls strengthened with bidirectional glass fiber and unidirectional carbon fiber. The experimental results of this study showed increasing in the capacity of the strengthened walls by 2 to 2.5 times the control walls, and all the walls failed first by crushing of the AAC material in midspan which may lead to sustain large displacement after crushing point. Tanner et al. (2005) developed a comprehensive testing program to determine the behavior of AAC shear walls subjected to reversed cyclic lateral loads. Uddin et al. (2007) examined the behavior of combined AAC as a sandwich panel with the carbon fiber reinforced polymer (CFRP) using vacuum-assisted resin transfer modeling. In these studies, fire resistance of the panels was compromised because of the organic polymers used for adhesion.

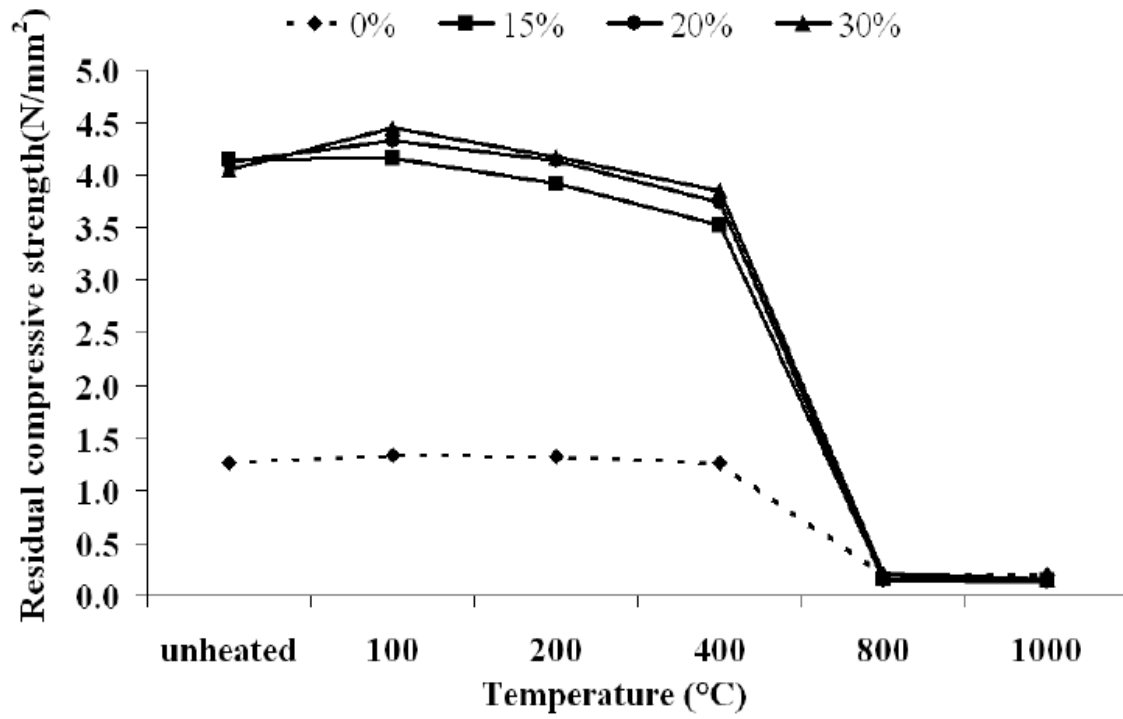


Figure 2. 10 Residual compressive strength of AAC (Ayudhya 2011).

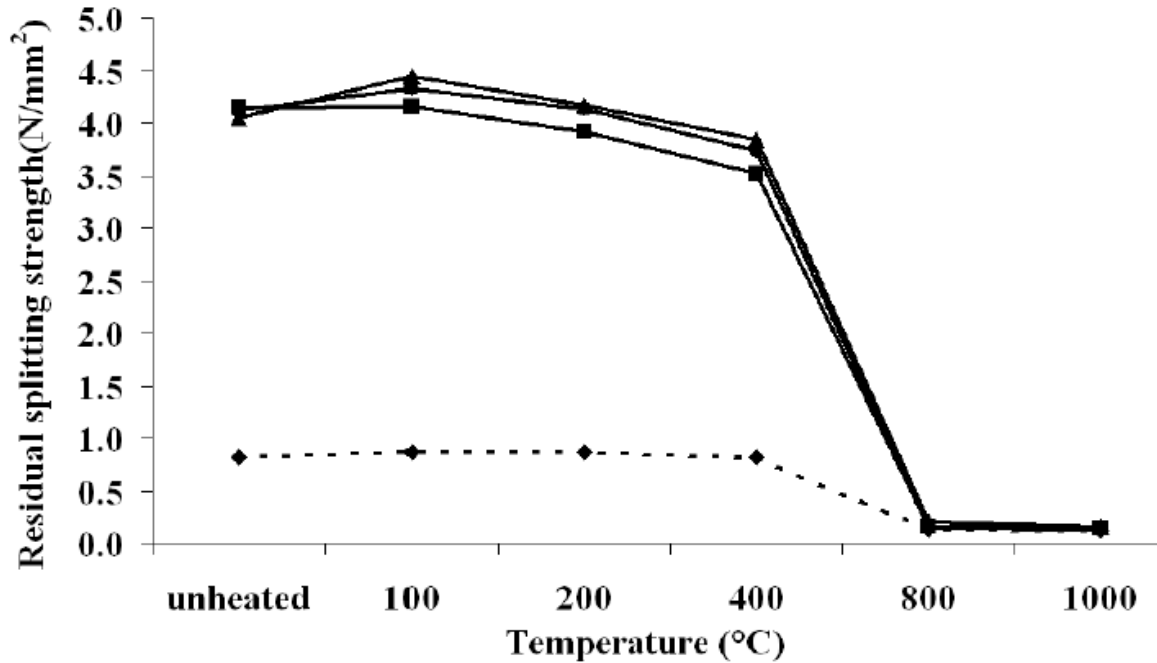


Figure 2. 11 Residual splitting strength of AAC after heating (Ayudhya 2011).

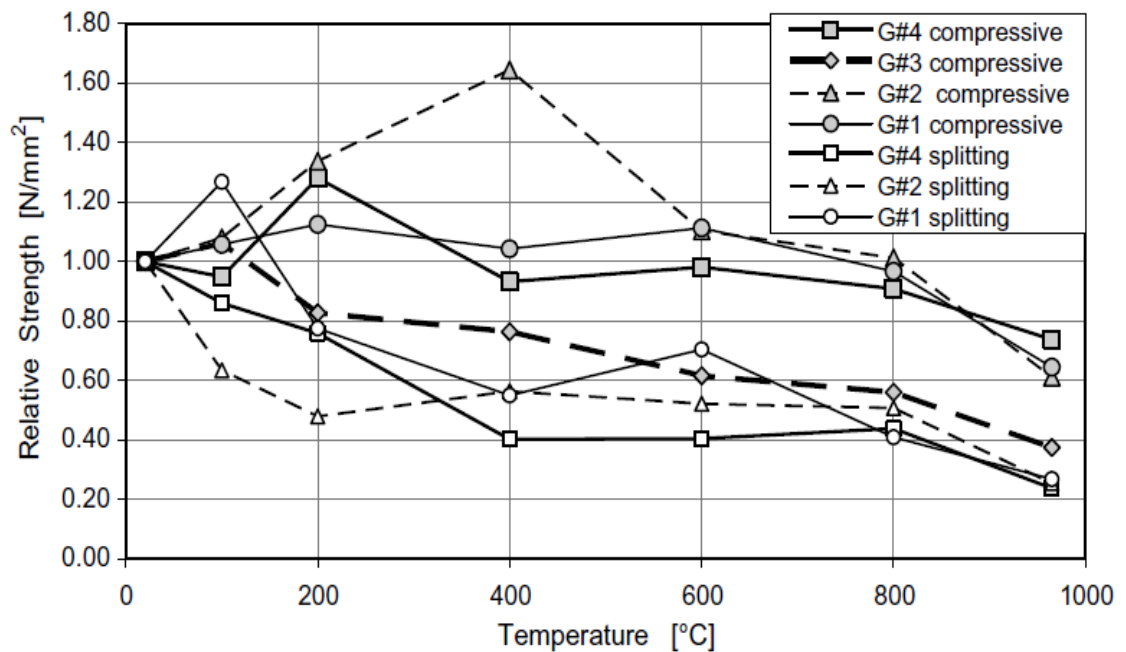


Figure 2. 12 relative compressive and splitting strength of AAC specimens as a function of the elevated temperature (Tanaçan 2009).

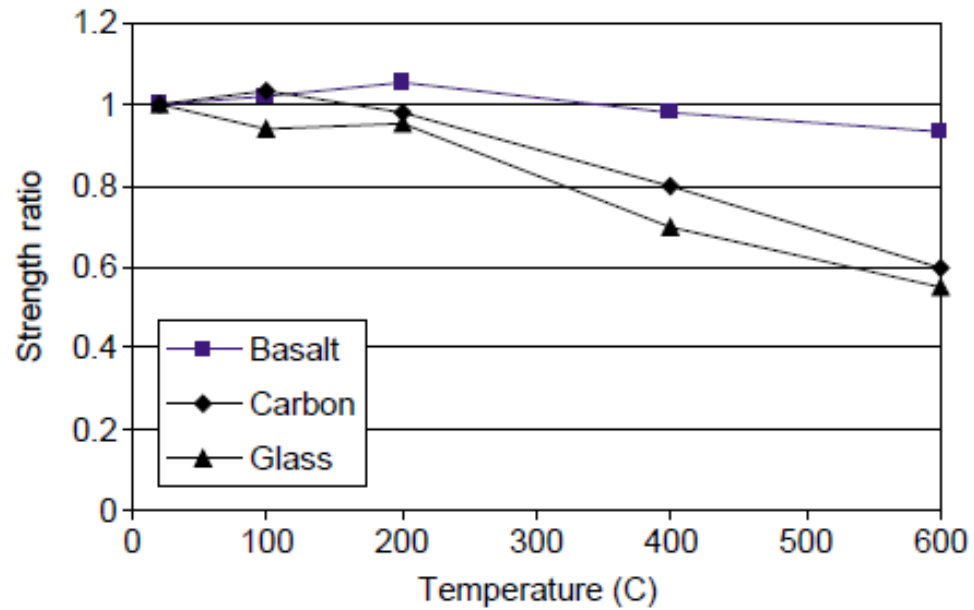


Figure 2. 13 Strength ratio Vs. Temperature for Basalt, Carbon, and Glass fiber (Sim and Park 2005)

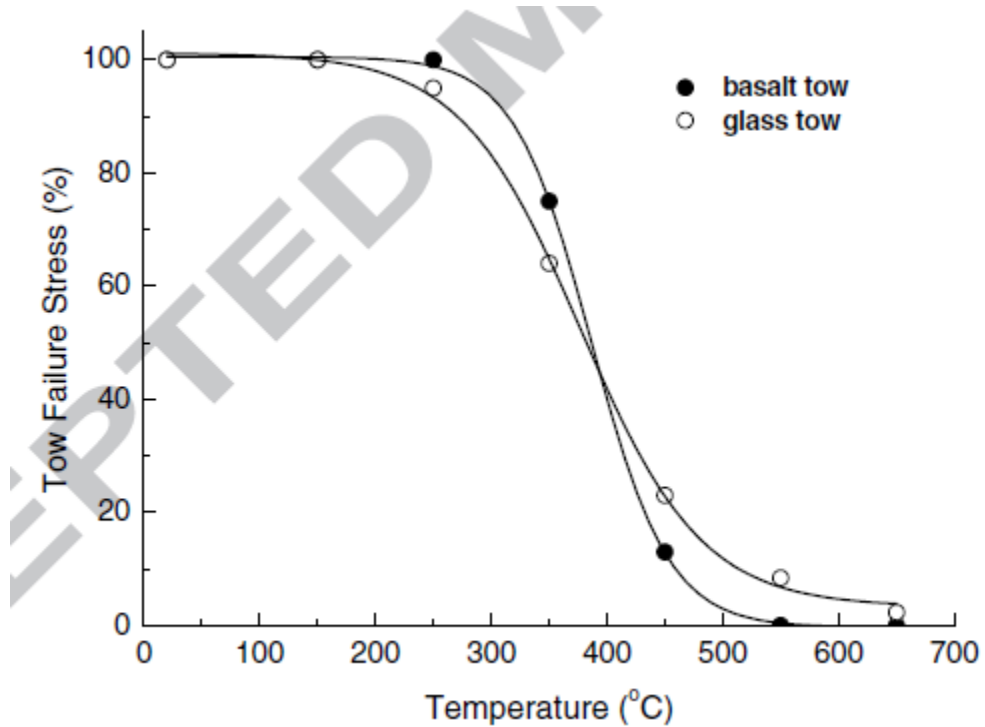


Figure 2. 14 Effect of increasing temperature on the residual strength of basalt and glass fiber (Bhat et al. 2014)

## CHAPTER III

### **PROPERTIES OF AAC, BASALT FIBERS, AND THE NANO-INORGANIC MATRIX**

#### **3.1 MATERIAL PROPERTIES**

The research program will include an experimental program designed to evaluate the behavior of plain AAC concrete as well as AAC concrete reinforced with basalt fibers. The research program will also include evaluation of plain AAC beams and fiber-reinforced AAC beams under thermal loads. The test program designed for this research was developed exclusively for the enhancing the strength of autoclaved aerated concrete (AAC) using basalt fabric/tows bonded to AAC using an inorganic matrix. For that, two test phases are developed and will be discussed in this experimental program. The first phase will include specimens with 18 inches span length, and the second phase will include large scale specimens with 44 inches span length. Both phases were discussed and elaborated in the following sections.

This chapter will first provide information and description of the properties of autoclaved aerated concrete (AAC), basalt fiber, and the inorganic matrix that will be used in the study.

#### **3.2 PROPERTIES OF AUTOCLAVED AERATED CONCRETE (AAC)**

The specific compressive strength of autoclaved aerated concrete is illustrated according to ASTM C1693-11 as shown in Table 3.1. The compressive strength of AAC is ranging between (290 – 870 psi), and the dry bulk density is ranging between (25 – 44 lb/ft<sup>3</sup>). This compressive strength is lower than the usual specific compressive of CMU which is normally 1500 psi. Even though, the compressive strength of AAC material is less than the

compressive strength of CMU by two to three times, the strength is adequate for a low-rise construction. For buildings constructed with multiple floors, the higher a building is constructed, the more load the bottom portions of the structure must support. As a reason, of the lower strength of masonry, compared to steel or concrete, a masonry structure would need bigger members sizes at the lower portion of the building to support the same loads and remain stable. This is why load-bearing masonry structures, and especially AAC, are not very tall when compared to buildings of steel and or concrete. The compressive strength of AAC is also sufficient for the other construction uses, for example, partitions or curtain walls, as shown in Figure 3.1.

Table 3. 1 ASTM Specification C1693-11 Autoclaved Aerated Concrete (ASTM, 2011)

Strength Class	Compressive Strength, psi (MPa) min	Nominal Dry Bulk Density, lb/ft <sup>3</sup> (kg/m <sup>3</sup> )	Density Limits, lb/ft <sup>3</sup> (kg/m <sup>3</sup> )	
			Lower Limit >	Upper Limit ≤
AAC-2	290 (2.0)	25 (400)	22 (350)	28 (450)
AAC-3	435 (3.0)	31 (500)	28 (450)	34 (550)
		37 (600)	34 (550)	41 (650)
AAC-4	580 (4.0)	31 (500)	28 (450)	34 (550)
		37 (600)	34 (550)	41 (650)
AAC-5	725 (5.0)	37 (600)	34 (550)	41 (650)
		44 (700)	41 (650)	47 (750)
AAC-8	870 (6.0)	37 (600)	35 (560)	41 (650)
		44 (700)	41 (650)	47 (750)

<sup>A</sup> The average drying shrinkage requirement of all strength classes is  $\leq 0.02\%$ .



Figure 3. 1 AAC used as an exterior non-bearing wall in Najaf, Iraq

In this study, the AAC blocks were obtained from AERCON Company. According to ASTM C 1693, AAC blocks are divided into five classes: AAC-2, AAC-3, AAC-4, AAC-5, and AAC-6. Class AAC-4 was used in this investigation. The actual dimensions of this AAC blocks were 3.9 inches x 7.9 inches x 23.9 inches, and it stocked in ballets with 120 blocks in each ballet. The dry density of the AC-4 block is 31 lb/ft<sup>3</sup>. Moreover, the direction of rising of these blocks was parallel to the long direction of the blocks. The standard 3.9 inches x 7.9 inches x 23.9 inches block was cut using water saw into two equal blocks. The compressive strength test was performed on 3.9 inches x 3.9 inches x 3.9 cube prism in

accordance with ASTM C1693-11 using one million pound Forney testing machine as shown in Figure 3.2. The cube specimens were air-dried for 14 days and tested. A total of four series of cubes were tested in compression. To ensure uniformity, the four series were obtained from four different blocks. Each series had three cubes. The average compression strength of the twelve cubes tested was 584 psi. The load was applied continuously on this test without stopping or shocking at the constant force controlled rate of  $4000 \pm 200$  lb/min. In previous research (Snow 1999), it was found that the test results are significantly influenced by the loading direction in relation to the direction of AAC paste rise. In the current investigation, the load was applied in the direction perpendicular to the direction of AAC paste rise as shown in Figures 3.3 (a) and (b). Flexible capping was applied at both ends of the prisms to ensure uniform load distribution during the test



Figure 3. 2 Compressive strength setup for AAC.

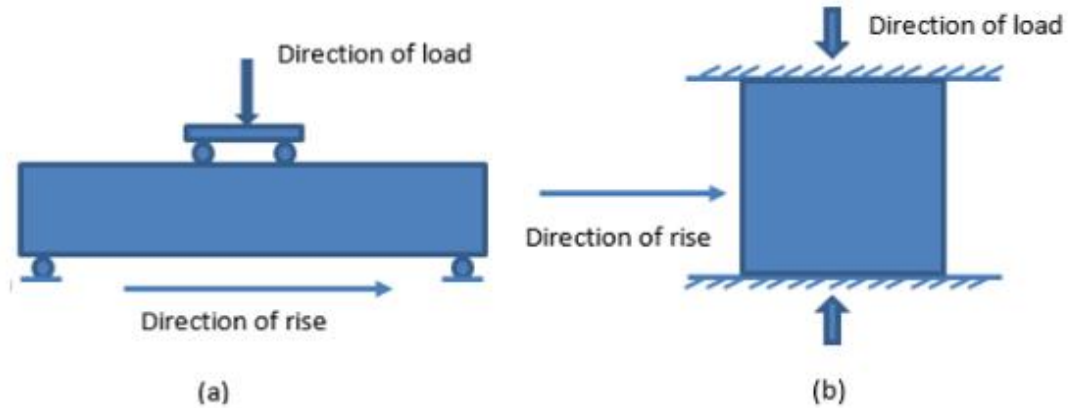


Figure 3. 3 (a) The direction of rising of AAC specimens and applied a load of flexural, (b) compressive strength test.

The results that have gotten from the compressive test for the four series of AAC cubes were listed in Table 3.2. Each series in the Table 3.2 was showing the results of three cubes have been taken from one AAC block. The block divided into three thirds and each cube taken from one third. The minimum individual compressive strength record was 556.4 psi in series II, while the maximum record was 613.3 psi in series IV. The maximum average compressive strength was in both series II, and series IV, (586.8 psi, and 586.22 psi) respectively with average COV (4.5 %, and 4 %) respectively. The minimum average compressive strength was in series I, 579.2 psi with average COV 3.2 %. The differences in compressive strength for both maximum and minimum groups was 7.6 psi, corresponding less than 1.3 %. The maximum standard deviation was 26.4 psi in series II, and the minimum was 18.3 psi in series I. All the four series showed consistent results. For that, all the results from the four series were adopted to estimate the average compressive strength of the AAC. The average compressive strength of was 583.8 psi with average standard deviation equal to 21.7 psi, and average COV equal to 3.7 %. In conclusion, all

the individual and average results have been obtained from the test were relevance to use toward getting the average compressive strength.

Table 3. 2 Test results for compressive tests of AAC cubs.

serie s #	cube no.	Widt h b (in)	Height h (in)	Area (in <sup>2</sup> )	Maximum load (lb)	Compressive Stress (psi)	Ave. stress (psi)	Standard deviation (psi)	CO V %
serie s I	C1	3.93	3.87	15.2 1	8900	585.2	579.2	18.3	3.2
	C2	3.95	3.92	15.4 8	8650	558.6			
	C3	3.92	3.92	15.3 7	9125	593.8			
serie s II	C4	3.93	3.91	15.3 7	8550	556.4	586.8	26.4	4.5
	C5	3.93	3.92	15.4 1	9300	603.7			
	C6	3.92	3.93	15.4 1	9250	600.4			
serie s III	C7	3.92	3.85	15.0 9	9125	604.6	582.8	18.9	3.2

	C8	3.87	3.91	15.1 3	8650	571.6				
	C9	3.88	3.92	15.2 1	8700	572.0				
serie s IV	C10	3.91	3.93	15.3 7	8825	574.3	586.2 2	23.5	4.0	
	C11	3.93	3.91	15.3 7	8775	571.1				
	C12	3.93	3.9	15.3 3	9400	613.3				
Average=							583.8	psi		

The compressive strength calculated for each specimen using the following formula

$$\text{Compressive strength, } f = \frac{P}{A}$$

Where:

$f$  = compressive strength of the specimens (psi)

$A$  = gross cross-sectional area of the specimen, in<sup>2</sup>

$P$  = maximum load, lb, indicated by the testing

### 3.2.1 Material properties of AAC from the ACI523.4R-09

The material properties also estimated using the equations from ACI523.4R-09. These equations used to calculate the modulus of elasticity of AAC, splitting tensile strength of AAC, modulus of rupture of AAC, and shear strength of AAC.

The modulus of elasticity has been tested in UAB (Dembowski 2001; Fouad and Dembowski 2005a). The orientation of applying a load in these studies was perpendicular and parallel to the direction of rising. The results showed higher modulus of elasticity for perpendicular orientation. According to another study (Tanner 2003), the modulus of elasticity calculated in both parallel and perpendicular to the direction of rising; however, the modulus of elasticity was similar in this study for both parallel and perpendicular orientation. In these studies, the modulus of elasticity plotted versus the compressive strength, however, the linear regression gives Eq. 3.1, with a correlation coefficient  $R^2$  of 0.97. It is suggested to calculate the modulus of elasticity as a nonlinear function of the compressive strength, as shown in Eq. 3.2.

$$E = 300f_{AAC} + 105000 \quad (3.1)$$

$$E = 6500f_{AAC}^{0.6} \quad (3.2)$$

For example, the compressive strength of the AAC has used in this study was 584 psi. For that, the modulus of elasticity using the linear equation is:

$$E = 300 * 584 + 105000 = 280,200 \text{ psi}$$

While using the nonlinear equation

$$E = 6500 * 584^{0.6} = 297,000 \text{ psi}$$

The nonlinear equation adopted in this study and the modulus of elasticity that used was 297 ksi.

In the same way, there is two equation to determine the splitting tensile strength for AAC according to (ACI523.4R-09) is:

$$f_t = 0.05f_{AAC} + 30 \quad (3.3)$$

$$f_t = 2.4\sqrt{f_{AAC}} \quad (3.4)$$

Where  $f_t$  and  $f_{AAC}$  in psi

For example, the splitting tensile strength of AAC with 584 psi compressive strength is:

$$f_t = 0.05 * 584 + 30 = 59.2 \text{ psi}$$

$$f_t = 2.4\sqrt{584} = 58 \text{ psi}$$

The relationship between the splitting tensile strength and modulus of rupture were studied (Fouad and Dembowski 2005a). The data reported using two methods, “Method 1” and a “Method 2.” Method 1 is a RILEM method involving midpoint loading with an a/d ratio (shear span to depth) of 1.25. Method 2 is a modified ASTM C78 method with two third-point loads and an a/d of 1.75. (Dembowski 2001; Snow 1999). A relationship between the splitting tensile strength and modulus of rupture was determined by using Eq. 3.5, and comparing it to the modulus of rupture.

$$f_t = 2\rho - 10.3 \quad (3.5)$$

Where  $\rho$  in lb/ft<sup>3</sup> and  $f_t$  in psi

Table 3.3 shows values of modulus of rupture reported by (Fouad and Dembowski 2005a) for different classes and corresponding oven-dry densities of AAC. Using a moisture content of 10%, the corresponding density for those specimens was calculated. Using Eq.

3.5, the splitting tensile strength of those specimens at that same density was also calculated. The average ratio between the reported modulus of rupture and the calculated splitting tensile strength is 2.26, with a coefficient of variation (COV) of 19%. For design purposes, a ratio of 2.0 is proposed to provide a simple yet conservative equation (Eq. 3.6) (Argudo 2003)

**Table 3.3 Ratios between measured modulus of rupture at ASTM C1386 density and splitting tensile strength\* (Fouad and Dembrowski 2005)**

Oven-dry density, lb/ft <sup>3</sup> (kg/m <sup>3</sup> )	Calculated density at 10% MC, lb/ft <sup>3</sup> (kg/m <sup>3</sup> )	Calculated $f_t$ at 10% MC, psi (MPa)	Measured $f_r$ at ~10% MC, psi (MPa)	$f_r/f_t$
32.2 (516)	35.2 (565)	60.2 (0.41)	123.0 (0.85)	2.04
38.0 (610)	41.8 (670)	73.4 (0.51)	202.0 (1.39)	2.75
42.0 (674)	46.2 (741)	82.2 (0.57)	162.0 (1.12)	1.97

\*Estimated using oven-dry density for different classes of AAC (Fouad and Dembrowski 2005a).

$$f_r = 2f_t \quad (3.6)$$

As proposed in Eq. 3.6, the modulus of rupture  $f_r$  can be expressed as twice the splitting tensile strength  $f_t$ . Substituting Eq. 3.6 into Eq. 3.4, Eq. 3.7 is obtained giving the modulus of rupture as a function of the compressive strength (Argudo 2003; Tanner 2003).

$$f_r = 4.8\sqrt{f_{AAC}} \quad (3.7)$$

Where  $f_{AAC}$  and  $f_r$  are in psi

For example, the splitting tensile strength of AAC with 584 psi compressive strength is:

$$f_r = 4.8\sqrt{584} = 116 \text{ psi}$$

Also, an experimental test for the modulus of rupture investigated in this study, and it has discussed in chapter 4.

Moreover, the shear capacity of the AAC has been investigated (Argudo 2003). In the normal concrete, the ACI318 suggested that unit strength is one-third of the mean diagonal tensile strength. In the same basis, the shear capacity of the AAC can be rewritten in terms of the splitting tensile strength  $f_t$  for use with AAC elements. The corresponding shear capacity  $V_{AAC}$  is given by Eq. 3.8 for members subjected to shear and flexure only, and by Eq. 3.9 for members subjected to axial compression as well (Argudo 2003).

$$V_{AAC} = \frac{f_t}{3} b_w d \quad (3.8)$$

$$V_{AAC} = \frac{f_t}{3} \left(1 + \frac{N_u}{2000A_g}\right) b_w d \quad (3.9)$$

Now, substitute Eq. 3.4 into. Eq. 3.8 and Eq. 3.9, then Eq. 3.10 and Eq. 3.11, are obtained as:

$$V_{AAC} = 0.8\sqrt{f_{AAC}} b_w d \quad (3.10)$$

$$V_{AAC} = 0.8\sqrt{f_{AAC}} \left(1 + \frac{N_u}{2000A_g}\right) b_w d \quad (3.11)$$

Where  $V_{AAC}$  is in lb and  $f_{AAC}$  is in psi.

For example, the shear strength for AAC section with 584 psi compressive strength, and cross section 4 inches X 4inches is:

$$V_{AAC} = 0.8\sqrt{584} \times 4 \times 4 = 309 \text{ lb}$$

### 3.2.2 Strength reduction factors according to ACI523.4R-09

In most cases, the actual strength of members in the field less than the nominal value. For that, the Strength-reduction factors ( $\phi$ -factors) are used as an attempt to address the many

factors that can cause this reduction in the nominal value. Differences between actual and nominal strengths can be caused by statistical variations in material strength, statistical variations in member dimensions and placement of reinforcement, and systematic errors in the equations used to calculate nominal capacity. Strength-reduction factors address such causes, as well as the nature and probable consequences of failure. For example, brittle failure modes are assigned a lower strength-reduction factor than ductile ones. Section 9.3 of ACI 318-05 presents these strength-reduction factors as:

- Tension-controlled sections,  $\Phi = 0.9$
- Compression-controlled sections,  $\Phi = 0.65$  or  $\Phi = 0.7$
- Shear,  $\Phi = 0.75$
- Bearing,  $\Phi = 0.65$

In the ACI523.4R-09, it is proposed to retain those same strength-reduction factors and to add additional strength-reduction factors for potential failure mechanisms that are unique to AAC panel construction. Section 9.3 of the proposed ACI 318-05 provisions presents these strength-reduction factors for AAC reinforced panels as:

- Tension-controlled sections,  $\Phi = 0.9$
- Compression-controlled sections,  $\Phi = 0.65$  or  $\Phi = 0.7$
- Shear,  $\Phi = 0.75$
- Bearing,  $\Phi = 0.65$
- Adhesion between untopped AAC floor panels,  $\Phi = 0.67$
- Truss mechanism in AAC floor and roof diaphragms,  $\Phi = 0.75$

These values can be justified as follows. For tension controlled elements, the statistical variation of flexural capacity is determined primarily by the statistical variation of the yield strength of the tensile reinforcement. Because this is the same for reinforced AAC and reinforced concrete, the same strength-reduction factor of 0.9 is proposed. In the case of plain (unreinforced) concrete or AAC, a significantly lower strength-reduction factor is assigned, because the failure mode now depends on flexural tensile resistance. Using the proposed design equations for the web-shear cracking capacity of reinforced AAC shear walls, the mean ratio of observed-to-predicted capacity is 1.15, with a COV of 13.8%, which is quite low compared with conventional concrete, and indicating that the formulas are reliable. The predicted capacities are based on the tested compressive strength. If the specified compressive strength were used rather than the tested strength, the ratio of observed to predicted capacity would be even greater because mean-tested strengths exceed the specified value. No change in strength-reduction factors for the behavior of anchors or development length is required because anchors and reinforcement are required to be embedded in the same type of grout (ASTM C476) that is commonly used around deformed reinforcement in cast-in-place sections of conventional precast concrete structures. The same strength-reduction factor of 0.65 for bearing on conventional concrete is also retained for bearing on reinforced AAC. Strength-reduction factors have been introduced for calculating the design capacity of untopped AAC floor and roof diaphragms, based on the mechanism involving adhesion across AAC joints, and on the mechanism based on a truss model for AAC floor and roof diaphragms. In adhesion of joints, a strength-reduction factor of 0.60 is proposed. This relatively low value is proposed because adhesion failure is brittle. A single strength-reduction factor is proposed for all elements of the truss model for AAC

floor and roof diaphragms to preserve equilibrium at the nodes under design resistances. The proposed factor of 0.75 is intended primarily to prevent crushing of the compression strut.

### **3.2.3 Thermal and acoustical characteristics of AAC**

As a porous material, AAC has excellent thermal and acoustical properties that result from the porosity of AAC. The fire rating of a solid 8 inches panel or modular block is 4 hours or greater as shown in Table 3.4. Also, there are no toxic gases emitted from the AAC through the fire episode. The AAC contains water in crystalline form, which acts as a heat sink, absorbing heat and changing into steam, which will escape through the cells without causing surface spalling. The thermal efficiency of a material may be measured through an R-value. The R-value is for a solid 8 inches. Class 4 AAC wall is 8 (Ytong Product Information); this is four to six times the R-value for a hollow 8 in. CMU and two to three times the R-value for an 8 in. CMU structure with 2 in. air cavity and an exterior wythe of clay masonry (Drysdale et al. All 1994). Because of its internal porosity, AAC has very low sound transmission, making it potentially useful acoustically. The sound transmission coefficient of AAC is higher than other building materials of the same weight (Ytong Product Information).

**Table 3. 4 Fire rating for walls, panels, and Roofs (www.aerconaac.com)**

Type of Element	Fire Resistance Rating	Min Thk of AERCON	Reference
Block Wall - Load Bearing	4 hr	6" Nominal	UL U919
Block Wall - Non-load Bearing	4 hr	4" Nominal	UL U919
Block Wall - Non-load Bearing	2 hr	3" Nominal	UL U919
Wall Panel - Load Bearing	4 hr	6" Nominal	UL U920
Wall Panel - Non-load Bearing	4 hr	6" Nominal	UL U920
Wall Panel - T&G Non-load Bearing	4 hr	8" Nominal	UL U920
Wall Partition - Non-load Bearing	3 hr	4" Nominal	ASTM E 119
Floor & Roof Panels	4 hr	6" Nominal	UL K909 & P932
Attached to Non-load Bearing Studs	2, 3, 4 hr	See Graphics	
Attached to Load Bearing Studs	1, 1-1/2, 2 hr	See Graphics	
Steel Column Protection	4 hr	4" Block or 8" Panel	UL X901

### 3.3 PROPERTIES OF BASALT FIBERS

In this experimental study, the fiber has been used as a reinforcing skin. The primary function of the reinforcement skins in the AAC members is to create tensile and compressive force to form a couple and generate the moment capacity of the section to resist the applied load. The fiber reinforcement is the principal constituent in a fiber-reinforced composite skin and occupies the largest volume fraction in a composite laminate comparing to the matrix. The commercially available fibers have varying properties and

consequently, affect the properties of the resulting composite (Mallick, 1993). The fibers reinforcements used in this experimental investigation was basalt fibers.

Basalt fibers are from basalt rocks through melting process at 1400 °C. Basalt fibers are environmentally safe, non-toxic, and possess high stability and insulating characteristics (Ramakrishnan 1998). Basalt Fiber Reinforced Polymer has been recently presented as a substitute for steel reinforcement for concrete structures and as external reinforcement for retrofitting of structures. Unlike Carbon Fiber Reinforced Polymer (CFRP) and Glass Fiber Reinforced Polymer (GFRP) materials, basalt fibers have not been widely used. The limitation of their use may be attributed to the deficiency of fundamental research and comprehensive testing required to establish proper design recommendations and guidelines.

The basalt fibers that used in this experiment were obtained from Sudaglass Company in Texas (<http://www.sudaglass.com>). The general properties and comparative technical characteristics of these fibers with fiber made from E-glass, and Silica are explained in Table 3.5.

**Table 3.5 Comparative technical characteristics of a filament made from E-glass, basalt, and Silica (www.sudaglass.com).**

Properties	SI Units	Basalt Filaments	Fiberglass	Silica Filament
Thermal				
Maximum application temperature	(°C)	982°	650°	1100°
Sustained operating temperature	(°C)	820°	480°	1000°
Minimum operating temperature	(°C)	-260°	-60	-170°
Thermal conductivity	(W/m K)	0.031-0.038	0.034-0.04	0.035-0.04
Melting temperature	(°C)	1450°	1120°	1550°
Virtification conductivity	(°C)	1050°	600°	1300°-1670°
Glow loss	(%)	1.91	0.32	1.75
Thermal expansion coefficient	(ppm/ °C)	8.0°	5.4°	0.05°
Physical/Mechanical				
Density	(g/cm <sup>3</sup> )	2.75	2.6	2.15
Filament diameter	(microns)	23-Sep	13-Sep	15-Sep
Tensile strength	(M Pa)	4840	3450	4750
Compression	(psi)	550,000	440,000	510,000
Elastic modulus	(G Pa)	89	77	66
Linear expansion coefficient	(x10 /K)	5.5	5	0.5

Elongation at break	(%)	3.15	4.7	1.2
Absorbtion of humidity (65%RAH)	(%)	<0.1	<0.1	<0.1
Stability at tension (20 C°)	(%)	100	100	100
Stability at tension (200 C°)	(%)	95	92	94
Stability at tension (400 C°)	(%)	82	52	80
Acoustics:				
Sound absorbtion coefficient	(%)	0.9-0.99	0.8-0.93	0.85-0.95
Electrical:				
Specific volume resistance	(ohm.m)	1*10x12	1*10x11	1*10x11
Loss angle tangent frequency	(1 MHz)	0.005	0.0047	0.0049
Relative dielectric permiability	(1 MHz)	2.2	2.3	2.3
Chemical Resistance				
% weight loss after 3 hrs boiling in:				
H2O	(%)	0.2	0.7	0.05
2n NaOH (Sodium Hydroxide)	(%)	5	6	5
2n HCl (Hydrochloric acid)	(%)	2.2	38.9	15.7

Unidirectional basalt fiber has been used in this study with UD-200-13-60 type as shown in Figure 3.4, 200 gm/m<sup>2</sup> density, and a diameter of 13 μm. Moreover, the breaking force for the basalt fiber was 960 N/cm, and the elongation at break was 6.2 %. The thickness of the fabric was 0.33 mm, and the width was 603 mm. Coupon tests were carried out according to ASTM D3039 to investigate the tensile strength and modulus of elasticity of the basalt fabric wetted with the organic and inorganic matrix.

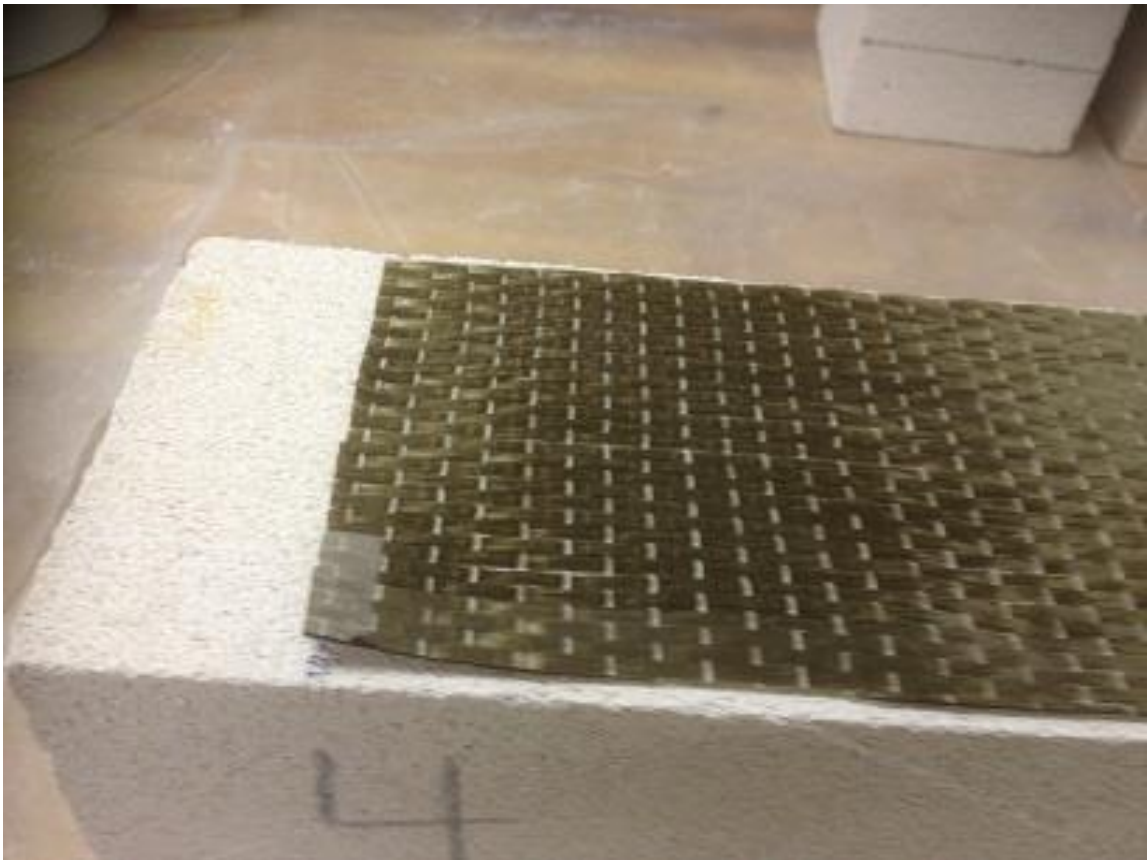


Figure 3. 4 Basalt fabric used in the current study

### **3.4 PROPERTIES OF THE MATRIX**

The principal functions of the matrix in a composite are:

- Holding the fibers together in a structural unit
- Protecting the fibers from external damage
- Transferring the loads to the fibers
- Contributing in needed properties like ductility, toughness, electrical insulation or high-temperature resistance

The chemical compatibility between matrix and fibers are important to avoid any undesired chemical reaction on the fibers' surfaces, which may affect the bond strength between the two or may even cause the disintegration of the fibers. This problem seems to be more effective in a high-temperature composite (Gibson 1994).

As a rule, matrices are divided into two main categories based on the chemical composition. They are divided into organic matrices, and inorganic matrices, each of these will be discussed in more detail.

#### **3.4.1 Organic resins**

Organic resins or polymers are the most widely used matrix material in the world of composites. Polymers can be classified into two types: thermoplastic and thermoset, according to the type of the cross-links formed between the molecules which greatly impact the effect of heat on their properties (Gibson, 1994).

Thermoset resins form three-dimensional molecular cross-links during the curing process. Consequently, once cured, the molecules cannot be melted or reshaped. The higher the

mass density of the cross-linking, the more rigid and thermally stable the resin will be. The resin may soften at high-temperatures, which may be used to create a bend or a curve. The most common used thermoset resins are epoxy, polyester, vinylester, phenolics, cyanate esters, bismaleimides, and polyimides (Gibson 1994; Mazumdar 2001). The continuous-use temperatures for these resins and some of their basic mechanical proprieties are shown in Table 3.6, Table 3.7.

**Table 3. 6 Heat release test results for OSU (Giancaspro, 2004)**

Specimen identification	Peak HRR (kW/m <sup>2</sup> )	$t_{PHRR}$ (s)	Heat release (kW·min/m <sup>2</sup> )		FAA test result (65·65) (pass/fail)	Specimen behavior/appearance
			2 min	5 min		
OSU Balsa 1 <sup>a</sup>	165	176	166	438	Fail	Ignited almost immediately
OSU Balsa 2 <sup>a</sup>	163	9	169	290	Fail	Ignited almost immediately
OSU Balsa 3 <sup>a</sup>	184	11	177	272	Fail	Ignited almost immediately
Average	171	65	171	333	All failed	All samples charred severely and/or were destroyed
Standard deviation	11.22	95.85	5.64	91.43		
OSU Reinf <sup>b</sup>	104	214	70	275	Fail	Started to flame up after about 30 s
OSU 2	53	106	21	130	Pass	Some charring; cracking of fireproofing
OSU 4	28	292	4	36	Pass	Charring and substantial cracking of fireproofing
OSU 5	11	518	-8	-7	Pass	Blisters, cracking; some charring
OSU 7	4	94	-10	-16	Pass	Blisters; slight charring near flame application point
OSU 11	3	605	-14	-23	Pass	Substantial charring (10.5 min of exposure)
Balsa (core only) <sup>c</sup>	125	125	—	40	Fail	—
GRP (no core) <sup>c</sup>	132	105	—	77	Fail	—
GRP/Balsa Core <sup>c</sup>	157	220	—	103	Fail	—

<sup>a</sup>Control sample: no reinforcement, no fireproofing.

<sup>b</sup>Reinforcement only, no fireproofing.

<sup>c</sup>Reference: U.S. Coast Guard (Grenier 1996).

**Table 3. 7 Typical thermosetting resin (Mazumdar 2001)**

Resin Material	Density, g/cc	Tensile Modulus, GPa	Tensile Strength, MPa
Epoxy	1.2-1.4	2.5-5.0	50-110
Phenolics	1.2-1.4	2.5-4.1	35-60
Polyester	1.1-1.4	1.6-4.1	35-95

Thermoplastics do not form cross-linked chains during the curing process which in turn gives them the ability to melt by heating then solidifying again by cooling. They are more flexible and tougher than the thermoset matrices. Thermoplastics can be either amorphous or semi-crystalline. They have very low creep resistance, especially in elevated temperature. Typical thermoplastics include nylon, polypropylene (PP), polycarbonate, polyether-ether ketone (PEEK), and polyphenylene sulfide (PPS) (Mazumdar, 2001). The continuous-use temperature ranges are shown in Figure 3.5, and some of the properties are shown in Table 3.8.

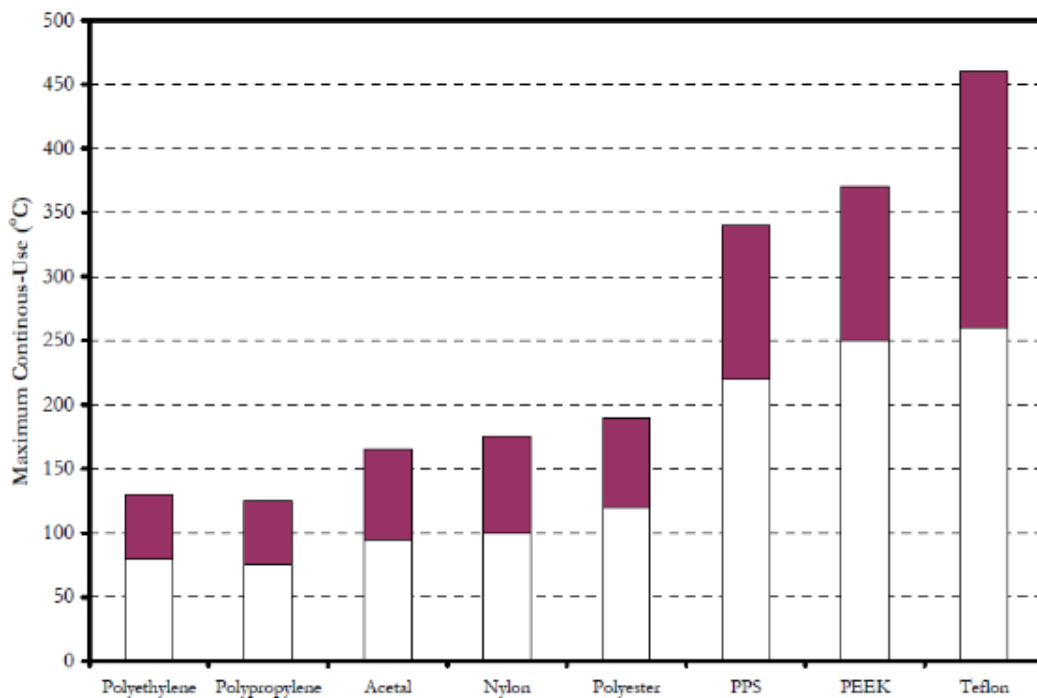


Figure 3. 5 Maximum continuous-use of thermoplastic resins (Mazumdar, 2001)

**Table 3. 8 Typical thermoplastic resin (Mazumdar, 2001)**

Resin Material	Density, g/cc	Tensile Modulus, GPa	Tensile Strength, MPa
Nylon	1.1	1.3-3.5	55-90
PEEK	1.3-1.35	3.5-4.4	100
PPS	1.3-1.4	3.4	80
Polyester	1.3-1.4	2.1-2.8	55-60
Polycarbonate	1.2	2.1-3.5	55-70
Acetal	1.4	3.5	70
Polyethylene	0.9-1.0	0.7-1.4	20-35
Teflon	2.1-2.3	-	10-35

### 3.4.2 Inorganic resin

One of the features in using inorganic resins is their ultra-high temperature resistance. In most studies, it was reported that none of the organic resins are heat resistant and that nature states that only minerals can provide heat and fire resistance. In the aftermath of many catastrophic incidents in France between 1970 and 1973 involving plastic materials, Joseph Davidovits worked on developing a promising new inorganic polymer. This polymer was based on geophysics and geochemistry so it was patent as Geopolymer and it is also known as polysialate. (Davidovits 2002).

Since the characteristics of such a new polymer are crucial for the aircraft industry, The Federal Aviation Administration (FAA) has been sponsoring research programs to evaluate the mechanical properties of Geopolymer matrix composites as part of an initiative to many research fireproof material for aircraft interiors. The best indicator for its fire resistance was the flashover time obtained from the ISO 9705 room corner test. Flashover occurs in a closed compartment when flammable gasses from incomplete material combustion are

heated to the ignition point. This puts an end to the lives of survivors peoples in a plane in aircraft post-crash scenarios. The performance of Geopolymer was compared to the different resins available, and its importance is proven in Figure 3.6 (Lyon 1997). The research was conducted at Rutgers University and elsewhere to evaluate the properties of the new polymer and its potential use.

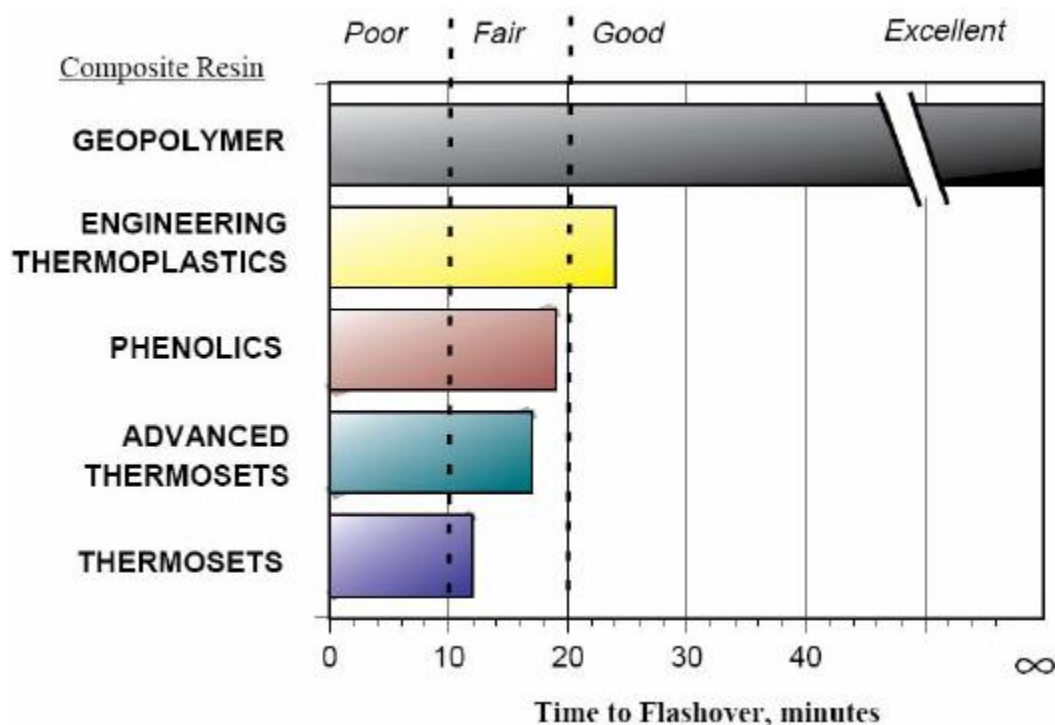


Figure 3. 6 Time to flashover for different resin systems (Lyon, 1997)

The experimental investigation at Rutgers University started with tests to evaluate the properties of an unreinforced Geopolymer matrix in tension, flexure, compression, strain capacities and surface energy. The mechanical properties of the resin reinforced with different types of fabrics like SiC and carbon were evaluated for samples subjected to temperatures from 200 to 1000°C. An example of the remaining flexural capacity of samples using different resins is shown in Figure 3.7. The optimum curing process to

minimize the void content and to maximize the volume of fibers and subsequently, the flexural strength was reported to be 80°C under 3 MPa pressure. It was found that the polysialate material were brittle and that the Geopolymer matrix was compatible with carbon and SiC fibers. It was also determined that the flexural stiffness of beams made of polysialate composites did not decrease under cyclic loading (Foden 1999).

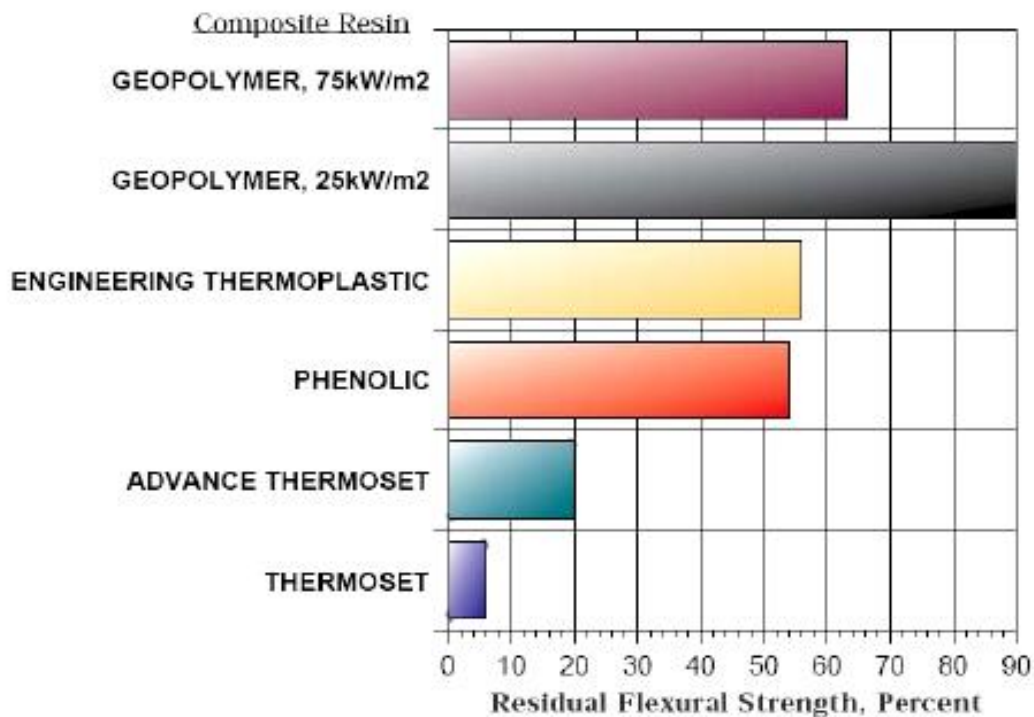


Figure 3. 7 Residual warp direction flexural strength of crossply laminates after thermal exposure (Lyon, 1997)

The influence of reinforcement type in inorganic laminate composites was evaluated. It was shown that carbon laminates using inorganic resin could achieve a flexural strength as high as 510 MPa. Because of the high alkali nature of the matrix, glass fibers degraded and the fibers fused with the matrix giving only 100 MPa. Steel wire meshes gave 140 MPa of flexural strength, but they exhibited a much more ductile behavior than carbon and glass laminates. It was shown that the wet-dry resistance mainly depended on the silica/alumina

ratio as well as the curing temperature. The reduction in silica/alumina ratio will result in a more durable matrix. The composite maintained 53% of its flexural strength and 30% from the flexural modulus after one hour exposure to 600°C. It was reported that the optimum elevated temperature for strength and durability is 150°C and strength decreased when cured to 200°C. It was also reported that the shrinkage of the resin was one of the Geopolymer drawbacks and is the cause of some mechanical capacity loss (Hammell 2000).

The application of a Geopolymer matrix widened to include its use as a protective coating for concrete structures. The durability studies of the coating included wetting and drying, freezing and thawing, and scaling. The results of the wet-dry and scaling tests are shown in Figures 3.8 and 3.9. After testing concrete beams strengthened with Geopolymer/carbon systems, it was concluded that it was feasible to strengthen concrete structures with the inorganic system. The Geopolymer is very compatible with concrete structures as the constituent materials of the coating chemically react with the concrete. The Portland cement used in concrete applications is a calcium aluminosilicate system whereas the cement in the coating is potassium aluminosilicate. Any free hydroxide in concrete will react with silica in the coating and vice versa. Because of its compatibility with concrete, delamination collapse could be eliminated with the proper design, while it is a main problem with organic systems. In addition to its dominance in terms of adhesion, it does not involve any toxic substances and leftovers can be treated as normal waste, which is a very important aspect of construction. Steel beams were also reinforced with inorganic systems. These tests showed that Geopolymer could be effectively used as a protective coating for steel but to strengthen steel, large carbon areas were needed (Garon 2000).

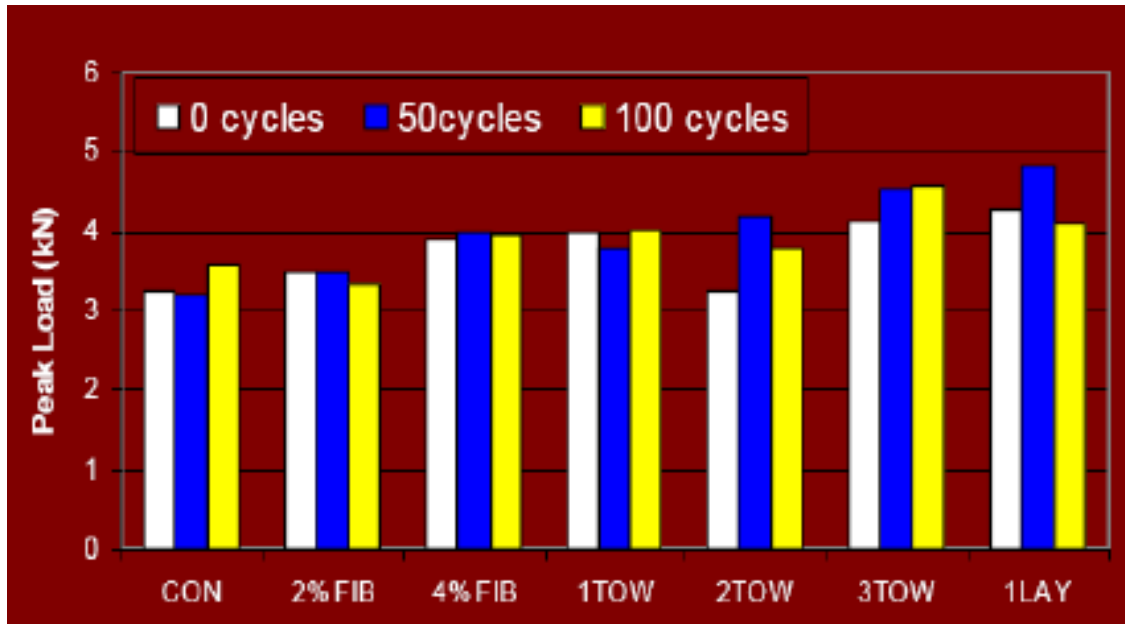


Figure 3. 8 Peak Loads after wet-dry exposure (Garon 2000)

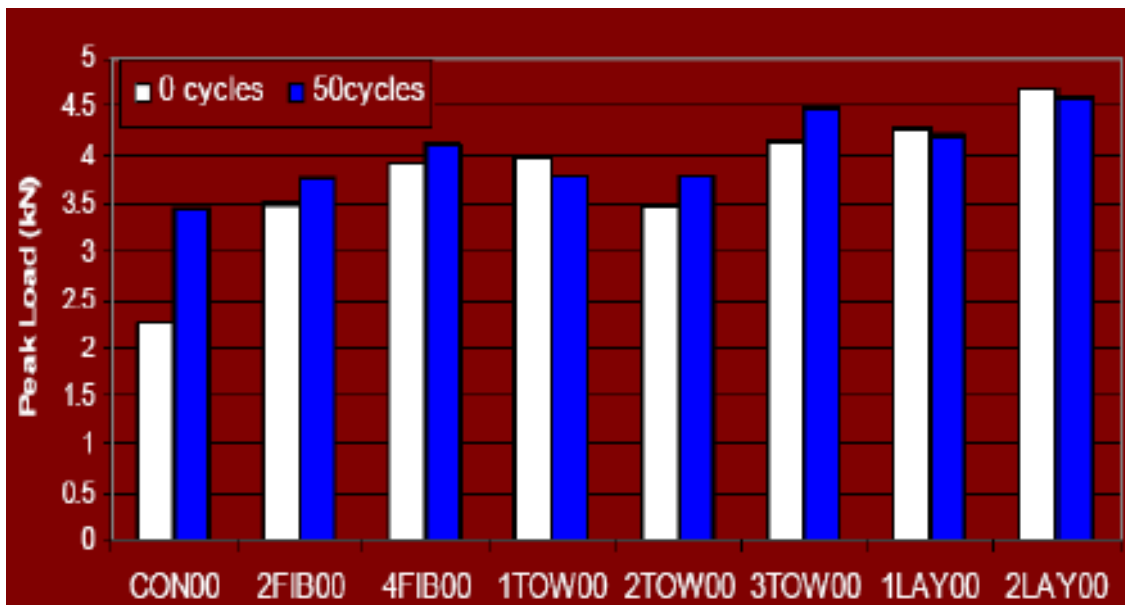


Figure 3. 9 Peak Loads after Scaling Exposure (Garon 2000)

More hybrid laminates were prepared and tested. It was concluded that during preparation that the 12K high modulus carbon was easier to handle and that more than 1 % sizing was damaging the composite strength. The optimum pressure for E-glass/Geopolymer composites was 1 MPa, and for carbon/Geopolymer composites this pressure was found to be 3 MPa. Flexural strength of E-glass composites could reach 122 MPa. The results obtained from the witness samples showed that carbon and aramid composites retained some load after the initial fracture, while E-glass composites showed no post-peak strength. This confirmed the conclusion optined by Hammell earlier that glass fibers become fused because of the alkali nature of the resin. The 12K high modulus carbon composites had a modulus of elasticity of 576 GPa. In addition to the hybrid-laminates, sandwich beams were fabricated using balsa wood as a core material and different inorganic composite skins as reinforcement. In addition, comparisons were made with similar organic-resin sandwich beams. After running some flexural tests, it was concluded that it was feasible to fabricate sandwich beams using balsa and Geopolymer based composites. High modulus carbon provided the best strength increase and that the increase in fiber area caused a consistent increase in flexural stiffness. By comparing the beams reinforced with organic composites, it was concluded that the bond between balsa wood and organic reinforcements was poor as some delamination failures occurred, which did not happen with reciprocal inorganic beams. The beams reinforced with organic skin had 70% more moment capacity and almost the same flexural stiffness. Bare balsa wood and reinforced panels were tested in the OSU and NBS smoke tests. The results, demonstrated in Tables 3.9 and 3.10, show that the bare panels and panels reinforced with organic skins failed the FAA passing criteria and only the samples reinforced with Geopolymer-based skins passed (Giancaspro 2004).

**Table 3. 9 Heat release test results for OSU (Giancaspro 2004)**

Specimen identification	Peak HRR (kW/m <sup>2</sup> )	$t_{PHRR}$ (s)	Heat release (kW·min/m <sup>2</sup> )		FAA test result (65-65) (pass/fail)	Specimen behavior/appearance
			2 min	5 min		
OSU Balsa 1 <sup>a</sup>	165	176	166	438	Fail	Ignited almost immediately
OSU Balsa 2 <sup>a</sup>	163	9	169	290	Fail	Ignited almost immediately
OSU Balsa 3 <sup>a</sup>	184	11	177	272	Fail	Ignited almost immediately
Average	171	65	171	333	All failed	All samples charred severely and/or were destroyed
Standard deviation	11.22	95.85	5.64	91.43		
OSU Reinf <sup>b</sup>	104	214	70	275	Fail	Started to flame up after about 30 s
OSU 2	53	106	21	130	Pass	Some charring; cracking of fireproofing
OSU 4	28	292	4	36	Pass	Charring and substantial cracking of fireproofing
OSU 5	11	518	-8	-7	Pass	Blisters, cracking; some charring
OSU 7	4	94	-10	-16	Pass	Blisters; slight charring near flame application point
OSU 11	3	605	-14	-23	Pass	Substantial charring (10.5 min of exposure)
Balsa (core only) <sup>c</sup>	125	125	—	40	Fail	—
GRP (no core) <sup>c</sup>	132	105	—	77	Fail	—
GRP/Balsa Core <sup>c</sup>	157	220	—	103	Fail	—

<sup>a</sup>Control sample: no reinforcement, no fireproofing.

<sup>b</sup>Reinforcement only, no fireproofing.

<sup>c</sup>Reference: U.S. Coast Guard (Grenier 1996).

**Table 3. 10 NBS smoke test results (Giancaspro 2004)**

Specimen identification	Reinforcement	Thickness of fireproofing (mm)	FAA test result		Specimen behavior/appearance
			<sup>4</sup> $D_m$	<sup>4</sup> $D_m < 200$ (pass/fail)	
NBS Balsa 1 <sup>a</sup>	—	—	26	Pass	Ignited almost immediately
NBS Balsa 2 <sup>a</sup>	—	—	31	Pass	Ignited almost immediately
NBS Balsa 3 <sup>a</sup>	—	—	25	Pass	Ignited almost immediately
Average for balsa (control) samples			27	All pass	All samples charred severely
Standard deviation for balsa (control) samples			2.84		
NBS Reinf 3k Uni <sup>b</sup>	3k Uni C	0	8	Pass	Slight charring on edges; swelling of facings
NBS Reinf 3k Woven <sup>b</sup>	3k Woven C&G	0	41	Pass	Surface turned white; slight charring on edges
NBS 3	3k Woven C&G	3	51	Pass	Moderate surface cracking
NBS 6	3k Woven C&G	6	34	Pass	Moderate surface cracking
NBS 9	3k Woven C&G	9	27	Pass	Moderate surface cracking

<sup>a</sup>Control sample: no reinforcement, no fireproofing.

<sup>b</sup>Reinforcement only, no fireproofing.

Inorganic composites were used to enhance concrete and clay brick walls in shear. The gained strength was about the same as the strength provided by organic composites. The same conclusions were found for masonry bricks reinforced for out-of-plane loadings. Extensive research was done on applying the inorganic based resin as a protective coating for concrete structures. Because of the growing graffiti problem, the Geopolymer mix could be modified to be graffiti-proof, and color pigments could be added later to the mix to give the concrete a protective and decorative coating. A demonstrative example of the

graffiti-proof nature of a Geopolymer coating is shown in Figure 3.10. The only dry cloth was used to remove the graffiti, and no special procedures were needed (Nazier 2004).



Figure 3. 10 Polysialate as graffiti proof coating (Nazier 2004)

In the current study, the inorganic matrix used consists of an alkali-alumino-silicate made of nano and micro size particles and high strength fibers that are more suitable for AAC strengthening due to the similarities of chemical make-up to AAC blocks. The final mix

design of the matrix included nano aluminosilicates for increased bonding, standard silica/alumina ratios and optimized activator dosages. The matrix was successfully applied to the basalt fiber using hand lay-up as shown in Figure 3.11.



Figure 3. 11 Applying the inorganic matrix using hand lay-up technique

This inorganic matrix was used to provide good bond mechanisms and adhesion between the AAC surface and the basalt fiber. The controlling mechanism of adhesion between the AAC block and the inorganic matrix is the chemical bonding as well as mechanical interlocking of the inorganic matrix in the irregularities and voids of the AAC surface. It

is worth noting here, that, despite the high porosity of the AAC surface, the adhesion between the basalt fabrics and tows and the AAC surface was good.

Further tests have been investigated in this study to find the mechanical properties of the inorganic matrix. Flexural strength and compressive strength have been done in this study:

## CHAPTER IV

### **EXPERIMENTAL PROGRAM**

A comprehensive experimental program was developed to evaluate the flexural performance of AAC beams. Phase I of the test program included specimen preparation and testing of plain AAC beams, AAC beams strengthened with basalt tows, and AAC beams strengthened with basalt fabrics. Two Groups of AAC beams were investigated in Phase I: Beams with 18 in long spans and beams with 48 in long spans. Phase II included specimen preparation and testing of thermal performance of plain AAC beams and AAC beams strengthened with basalt fabrics. The full details of the experimental program are discussed in the next sections.

### **4.1 PHASE I: (PLAIN AND REINFORCED AAC BEAMS)**

#### **4.1.1 Specimens details and identification**

Three groups of AAC beam specimens divided into fourteen series that include control beams, beams strengthened with basalt fabrics, and beams strengthened with basalt tows were prepared and tested in this investigation. For each series of beams, three specimens were prepared and tested. The results from individual beam tests in each series were consistent, and the average values from each series were used. The clear span length of all specimens was 18 inches. This span was governed by laboratory space restrictions. Furthermore, the shear spans were 7 inches each, and the flexural span in the middle was 4 inches for all specimens. Twelve series had a square cross-section with 4x4 inches, while the other two had a rectangular cross-section 4x6 inches. The sample designations and the details of specimens are given in Table 4.1. One group was tested without basalt

strengthening to determine the cracking moment, modulus of rupture, and to compare with the strengthened specimens. Moreover, beams with a flexural capacity greater than shear capacity were reinforced with basalt fabric in both faces of the shear span to avoid premature failure due to shear. The load required to cause support failure was also investigated in this study. Consequently, the support area was enhanced with U-wrap basalt fabric to increase the bearing capacity to all beams with a higher load than support failure load in order to obtain the maximum flexural capacity of the specimens Figure 4.1. The cross-sectional dimensions and amount of basalt reinforcement were selected in order to meet the design goal of forcing flexural behavior in the specimens.

In general, the groups were categorized into three separate sets. This classification of these groups was depended on the type of strengthening. The first group represents plain AAC specimens, and it had only one series in this group as shown in Table 4.1. The second group represents the specimens strengthened with tows, and it was subdivided into four series depending on the number of tows and on whether shear reinforcement was provided as shown in Table 4.1. The third group represents the specimens with basalt fabric reinforcement, and it was subdivided into nine series depending on the different variables such as aspect ratio, the width of fabric, and the presence shear enhancement.

#### **4.1.2 Series Identification**

The coding of the series that have been used in this test consist of four, or five sample Table 4.1. The first sample always (S) which referred to word specimen. The second sample was number, and it referred either to the number of tows or the width of the basalt fabric. The third sample either (T), or (F), and it explained if the scheme reinforcement was tows or

fabric. The fourth sample either (N), or (S), and it explained either this series enhanced for shear or not. There were four series with five sample, and the fifth sample either number two or three. If the fifth sample was two that mean this series was identical with series with the same first four samples except for the way of fabric distribution in tension face. If the fifth sample was three that means this series was identical with the series that had the same first four samples except for the depth of the specimens increased from 4 inches to 6 inches.

Examples:

The coding of the series S5TN means:

S: specimens

5: five tows

T: reinforced with tows

N: no shear enhancement

The coding of S90FS3 means:

S: specimens

90: basalt fabric with 90 mm width

F: reinforced with fabric

S: shear enhancement was provided

3: means this series was same as the series S90FS except for the depth in this series was 6 inches instead of 4 inches.

Table 4. 1 Phase I specimen types and geometry

Series description	Series ID	Strengthening type (No. of tows or fabric width ( in.))	beams width (in)	beam depth ( in.)	Shear reinforcement provided
Plain AAC	S1PN	-	4	4	NO
AAC beams strengthened with tows	S4TN	4	4	4	NO
	S5TN	5	4	4	NO
	S10TN	10	4	4	NO
	S10TS	10	4	4	YES
AAC beams strengthened with fabric	S13FN	0.5	4	4	NO
	S90FN	3.5	4	4	NO
	S90FS	3.5	4	4	YES
	S90FS2	3.5	4	4	YES
	S50FS	2	4	4	YES
	S50FS2	2	4	4	YES
	S50FS3	2	4	6	YES
	S90FS3	3.5	4	6	YES
S180FS	7	4	4	YES	



Figure 4. 1 Strengthening of AAC beam end areas.

#### 4.1.3 Preparation of specimens and test set-up

The flexural testing of all samples was conducted at Rutgers, the State University of New Jersey. Prior to testing, the AAC samples were cut from commercially available 4 X 8 X 24 inches AAC blocks using a table saw, and the actual dimensions were determined using a digital balance accurate to within  $\pm 0.1$  mm. After that, the samples were cleaned from the dust prior to applying the inorganic matrix. The hand lay-up technique was used to wet the basalt fabrics and tows. After cleaning the AAC surface, a layer of inorganic matrix applied to the AAC surface to fill all the opening cell in the AAC surface. After that, the basalt fabric wetted separately with the inorganic matrix in both sides using a paintbrush followed by a threaded roller to ensure all filament of basalt were wetted well with the

matrix as shown in Figure 5.1. The wetted fabrics were then applied to the surface of the AAC blocks. Finally, the extra inorganic matrix scraped from the exterior surface.



Figure 4. 2 Preparing and applying the inorganic matrix for AAC beams

The specimens were left three weeks to cure at ambient conditions in the laboratory environment until the inorganic matrix had been cured sufficiently. The same procedures were used to reinforce the specimens for shear. If two layers were used like in series (S180FS), the layers were first prepared and laid on top of each other. After that, placed on the AAC surface.

After the composite cured for three weeks, the specimens were tested in four-point bending with loading points spaced 4 inches apart using MTS machine as shown in Figure 5.2. Specimens were tested using span equal to 18 inches. This yielded a span-to-depth ratio of 4.5. Moreover, the load was measured using a 10 Kips load cell placed above the point loads. The load was applied slowly and continuously with deflection control until the specimen reached its ultimate load with a loading rate equal to 0.05 in/min. Furthermore, one vertical linear variable differential transformer (LVDT) with an accuracy  $\pm 1$  % from the full range attached to the mid-span of each specimen was used to measure deflections. The applied total load was recorded by the MTS computer program and was plotted versus the measured mid-span deflection. The failure mode was recorded using photographs. The dead load of the beam was neglected.

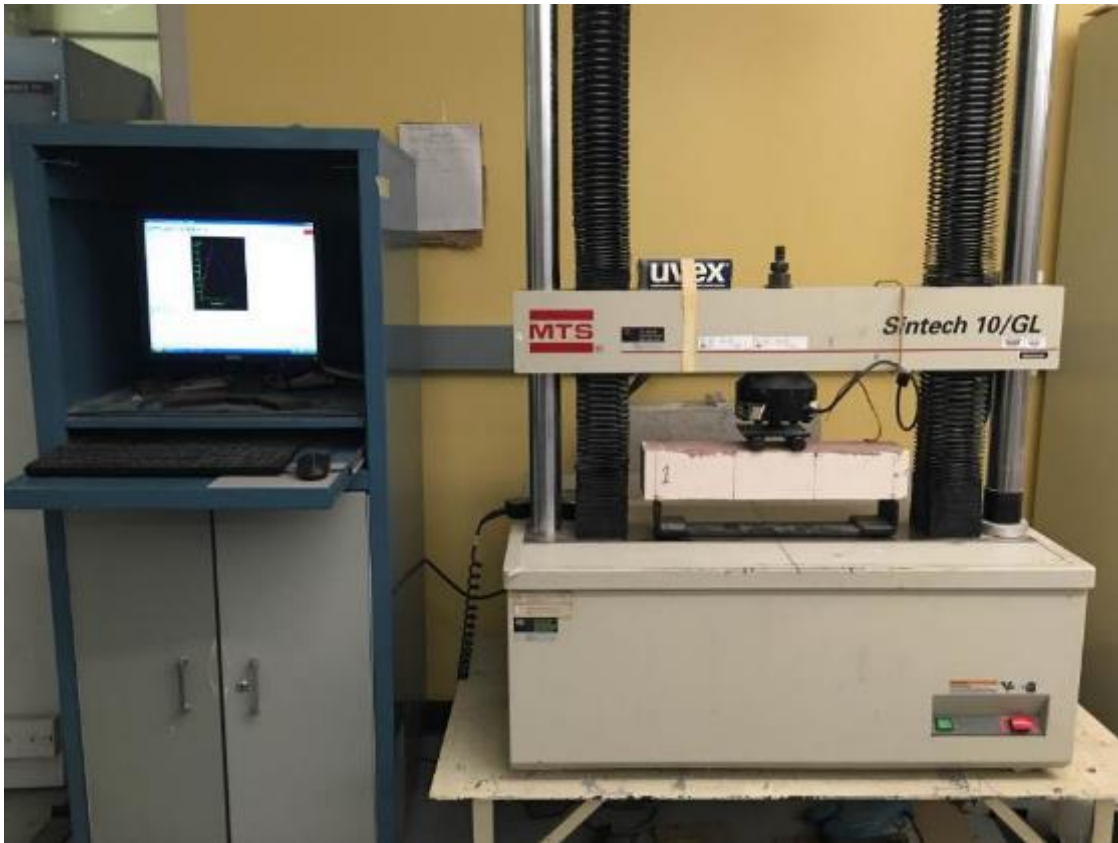


Figure 4. 3 Flexural Test Setup

#### 4.1.4 Test specimens for the inorganic matrix

Six beams divided to two groups have been prepared and tested in the civil engineering laboratory to investigate the flexural strength of the inorganic matrix used for reinforcing the AAC beams. The test specimens were 20 in long beams made of plain concrete. The beam cross section was 6 in x 6 in and the clear span was 18 in. All beams were prepared and cured according to ASTM C192/C192M. All beams were cut in the middle using water table saw as shown in Figure 4.4. The compressive strength of cylindrical concrete specimens was determined according to ASTM C39/C39M-15a. The average compressive strength of the first set of concrete beams was 6250 psi, while the second set was 7000 psi.

In the first set, the beams were re-attached together using the inorganic matrix in the same cut order (same cut faces) as shown in Figure 5.1 in Chapter V. In the second set, the beams were re-attached back to back (cast faces). The second group accounts for the effect of the roughness of the cast faces in practical applications. After all beam segments were cut and re-attached using the inorganic matrix, they were cured in a laboratory environment for three weeks. After that, the beams were tested for flexural strength according to ASTM C78/C78M-15b as shown in Figure 5.2 in Chapter V.



Figure 4. 4 Cut the concrete beams in the middle

## **4.2 PHASE II: PLAIN AND REINFORCED AAC BEAMS FOR THERMAL TESTS**

### **4.2.1 Specimens details and identification**

In this phase, five series of Autoclaved Aerated Concrete (AAC) beams has been tested at room temperature (23 °C) and after exposure to different sets of elevated temperatures. Four series of AAC beams were tested for flexural, and the fifth series was AAC cubes specimens tested in compression at room temperature and at elevated temperature up to 1000 °C. Table 4.2 summarizes the test program for Phase II. Series S1 in Table 4.2 has four plain AAC specimens S1-P1, S1-P2, S1-P3 and S1-P4. These specimens were tested at 23 C, 100 C, 200 C, and 300 C respectively. Series S2 also has six AAC beams: S2-P1, S2-P2, S2-P3, S2-P4, S2-P5, and S2-P6. These beams were coated with the inorganic matrix and were tested at 23 C, 100 C, 200 C, 300 C, 400 C, and 600 C respectively. Wall panels, lintels, and roof panels are the most common structural AAC components used in building construction and are typically reinforced with steel wire mesh. However, the tensile and flexural strength of AAC panels are very low and bonding of structural steel to AAC is weak due to the high porosity of AAC. To maintain this improved bending strength at high temperatures, basalt tows as main reinforcement, and an inorganic matrix was used for strengthening and bonding the basalt tows to the AAC beams. Testing procedure, test results and discussions for Phase II are presented in Chapter VI.

Table 4. 2 Summary of specimen details and geometry for Phase II

Series	Specimen Dimension (width X depth X span) (in)	Specimen Type	Test Type	Temperatures (°C)
S1-P1 to S1-P4	4 x 2 x 6	Plain beams	Flexure	23, 100, 200, 300
S2-CP1 to S2-CP6	4 x 2 x 6	Plain beams coated with inorganic resin	Flexure	23, 100, 200, 300, 400, 600
S3-P1 to S3-P4	4 x 4 x 12	Plain beams	Flexure	23, 100, 200, 300
S4-BT1 to S4-BT4	4 x 4 x 12	Reinforced beams with basalt tows	Flexure	23, 100, 200, 300
S5-C1 to S5-C8	4 x 4 x 4	Plain cubes	Compression	23, 100, 200, 300, 400, 600, 800, 1000

## CHAPTER V

### **PHASE I: TEST RESULTS AND DISCUSSION**

The preliminary test results obtained from the flexural tests of plain AAC beams and AAC beams strengthened with basalt fabrics, and tows are presented and discussed in this section.

#### **5.1 Tests of the flexural strength of the inorganic matrix**

The results of the flexural strength of the inorganic matrix showed that all re-attached beams failed in flexure. All failure locations in the first group (cut face attached), were in the concrete zone as shown in Figure 5.3. In the second group (cast face attached), the failure was in the concrete mortar as shown in Figure 5.4. However, there was no direct failure in the inorganic matrix. The average flexural strength of the first group was 677 psi, while in the second group was 502 psi. The flexural strength of the first group according to (ACI318-14, eq. (19.2.3.1)) was 593 psi, while for the second group was 627 psi.



Figure 5. 1 Re-attached the cut concrete beams using inorganic matrix.

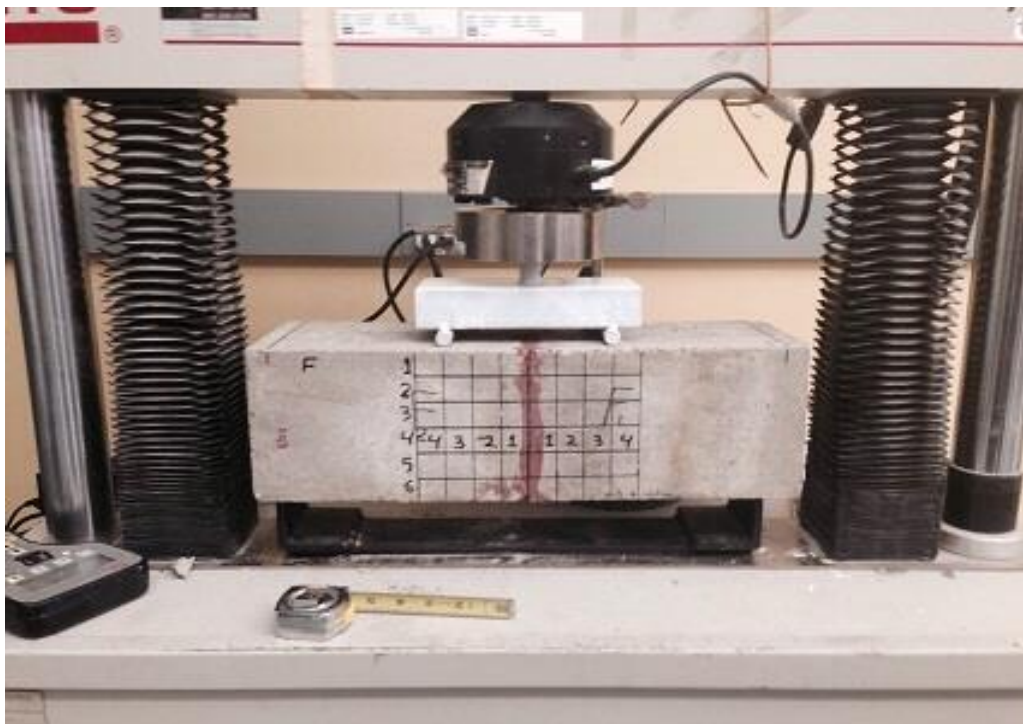


Figure 5. 2 Flexural test of the concrete beams attached to the inorganic matrix.



Figure 5. 3 Failure mode in cut attached faces concrete beams.



Figure 5. 4 Failure mode in cast attached faces concrete beams.

As a conclusion, the inorganic matrix was adequate to re-attach the concrete beams and the flexural strength of the inorganic matrix higher than the flexural strength of the concrete. In the first group, the reported flexural strength was higher than the flexural strength from ACI318 by 12.4 %, and the expected flexural strength of the inorganic matrix was higher than 677 psi. In the second group, the reported flexural strength was less than the one has been gotten from ACI318 by 20 %, but the reported data from the second group represented the strength of the mortar, and it had not represented the flexural strength of the concrete.

## **5.2 Compressive strength of the inorganic matrix**

In previous studies (Wongpa 2010), the compressive strength of an inorganic polymer depends mainly on both the ratio of SiO<sub>2</sub>/Al<sub>2</sub>O<sub>3</sub> and the types of raw material used. In addition, the compressive strength has an influence on the modulus of elasticity of the inorganic matrix, and they have suggested the following equation to estimate the modulus of elasticity. The Eq. (5.1) found that the square root of compressive strength linearly affects the elastic modulus of the inorganic matrix the same as Portland cement concrete but the slope of the relation of the inorganic matrix was lower than that of conventional concrete by about three times.

$$E = 1687\sqrt{f'_c} - 16078 \quad (5.1)$$

Where E and  $f'_c$  in MPa

On current study, one matrix was used to determine the compressive strength of the inorganic matrix. Twelve small cubes have been cast and prepared in the civil engineering lab of Rutgers University Figure 5.5. Sodium hydroxide with ratio approximately 2.5 by weight was used as the activator part of the mixture to prepare the cubes. The mixing and

curing of these inorganic cubes were performed under laboratory conditions. The dimension of each cube was 1inx1inx1in. This dimension was selected to avoid the cracks due to shrinkage of the inorganic matrix. After curing, there was significant shrinkage in the cubes, but there were not cracks occurred from shrinkage due to the continuing reaction. Compressive strength was examined at 28 days of preparing.

The reported results showed that all cubes failed in crushed as shown in Figure 5.6, and the average compressive strength of the inorganic matrix was 4520 psi with standard deviation equal to 466 psi, while the COV was 10 %. The results showed very good compatibility with the results that have been gotten by (Wongpa 2010), Figure 5.7.



Figure 5. 5 Preparing the inorganic matrix cubes.



Figure 5. 6 testing of inorganic cubes in compressive machine

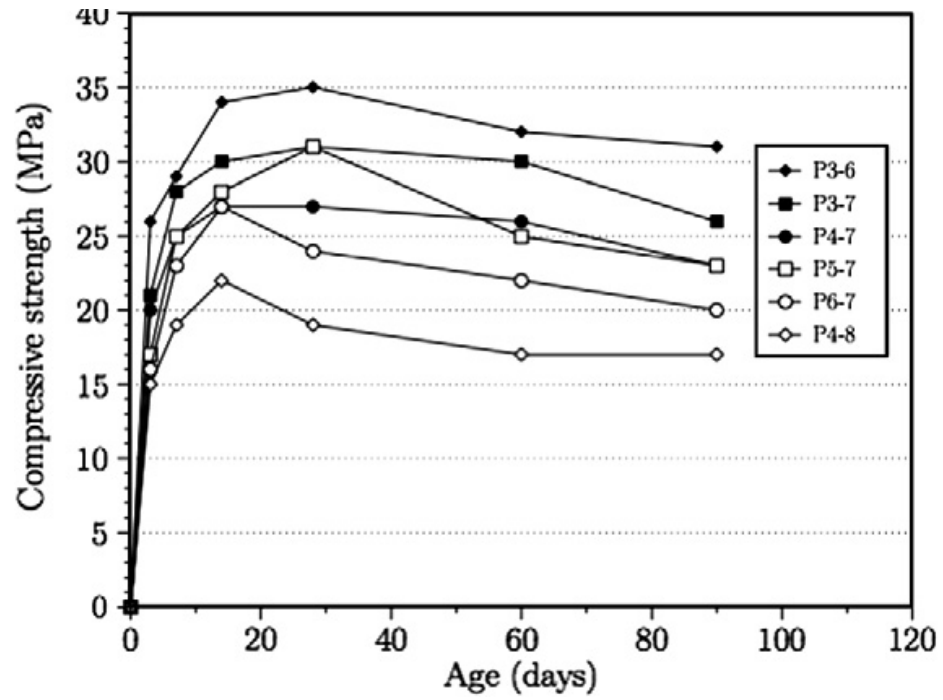


Figure 5. 7 Compressive strength for different mixes (Wongpa 2010)

### 5.3 Tests of AAC Plain specimens

Specimens SIPN are plain AAC beams or control beams (i.e., no fiber reinforcement was applied to these beams). In this series especially, four specimens have been tested with 18 inches span. All the plain specimens failed in the single flexural crack with linear behavior as expected Figure 5.8.

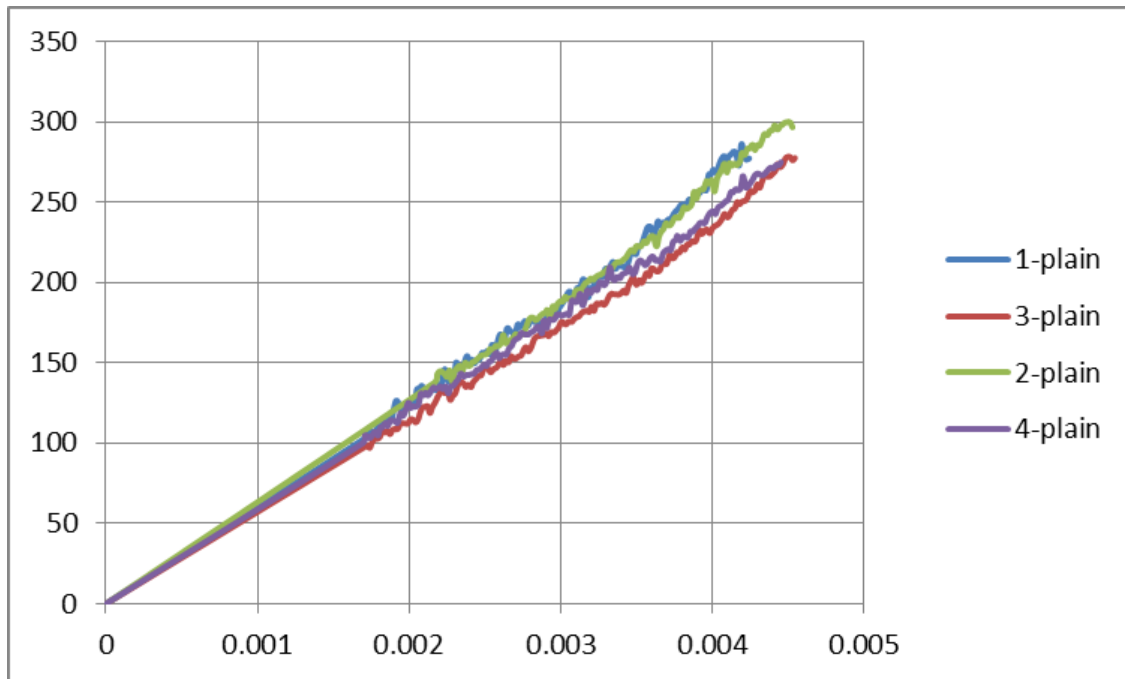


Figure 5. 8 Flexural behavior of Plain specimens

The average failure load observed in this series was 285 lb with standard deviation equal to 11.1 lb, and COV equal to 3.9 %. The average reported modulus of rupture was 84.3 psi, however, by using the ACI523 formula for modulus of rupture, the rupture stress was 116 psi. The modulus of rupture calculated from ACI523 formula was higher than the one reported in the current test by 27 %. The further test has been investigated in this study for plain AAC beams with 12 inches span to check the modulus of rupture, and the reported

results were explained and elaborated in Table 5.2. The new span was yielded span to depth ratio equal to 3. In the new series with 12 inches span, the average modulus of rupture was 109 psi. The new series was more converge with the ACI523 formula, and the formula showed 6 % increased only, however in this study the results from the beams with 18 inches span were adopted.

The ultimate mid-span deflection was reported as shown in Table 5.1, and the average deflection was 0.0048 in. The elastic deflection was calculated using the formula:

$$\Delta = \frac{Pa}{48EI} (3l^2 - 4a^2)$$

Where:

$\Delta$  = mid-span deflection (in)

P = total load measured in the lab (lb).

A = shear span (in).

E = modulus of elasticity calculated using ACI523 formula (psi).

I = moment of inertia of the section (in<sup>4</sup>).

l = total span of the beam (in).

The modulus of elasticity used in the elastic equation was calculated earlier in this study using the ACI523 formula, and it was equal to 297 ksi. The shear span was 6 inches, and the moment of inertia was 19.5 in<sup>4</sup>. The calculated elastic deflection was 0.005 in, and it showed increased by 4% only from the measured mid-span deflection.

Table 5. 1 Test results of the plain AAC beams with 18 inches span

beams #	b(in)	h(in)	Reported load(lb)	Reported deflection (in)	Cracking moment( lb.in)	Flexural stress(psi)	Average stress (psi)	type of failure
1	3.89	3.93	286	0.0042	840.1	83.90	84.3	flexural
2	3.85	3.93	300	0.0062	881.3	88.92		flexural
3	3.85	3.93	278	0.0055	816.6	82.40		flexural
4	3.87	3.91	275	0.0033	807.8	81.92		flexural

Table 5. 2 Test results of the plain AAC beams with 12 inches span

beams #	b(in)	h(in)	Reported load(lb)	Reported deflection (in)	Cracking moment( lb.in)	Flexural stress(psi)	Average stress (psi)	type of failure
5	3.9	3.93	557	0.0022	1114.0	110.97	109.0	flexural
6	3.87	3.95	587	0.0027	1174.0	116.66		flexural
7	3.87	3.92	521	0.0029	1042.0	105.13		flexural
8	3.8	3.91	500	0.0029	1000.0	103.28		flexural

#### 5.4 AAC Beam Specimens Strengthened with Basalt Tows

These specimens were subdivided into four series depending on the number of tows in the tension zone. Each series has three specimens. Only one series had shear reinforcement using basalt fabric. Due to the low shear capacity of the AAC material, the AAC beams strengthened with basalt fibers needed to be reinforced in shear to avoid premature shear failure. Shear reinforcement was achieved by applying basalt fabric on both faces of the shear spans of the beams.

The specimens in series S4TN were reinforced with four tows in the tension zone. All the specimens in series S4TN failed in flexure showing a 33 % increase in load capacity

compared to the plain AAC as shown in Table 5.3. This increase in load was good in comparison with the diminutive area of reinforcement  $0.0002 \text{ in}^2/\text{tow}$ . However, the ductility ratio increased eight times due to this strengthening. The load-deflection behavior was linear up to failure without any considerable hardening as shown in Figure 5.9. The specimens reinforced with this scheme showed the same deflection of approximately 0.0393 in.

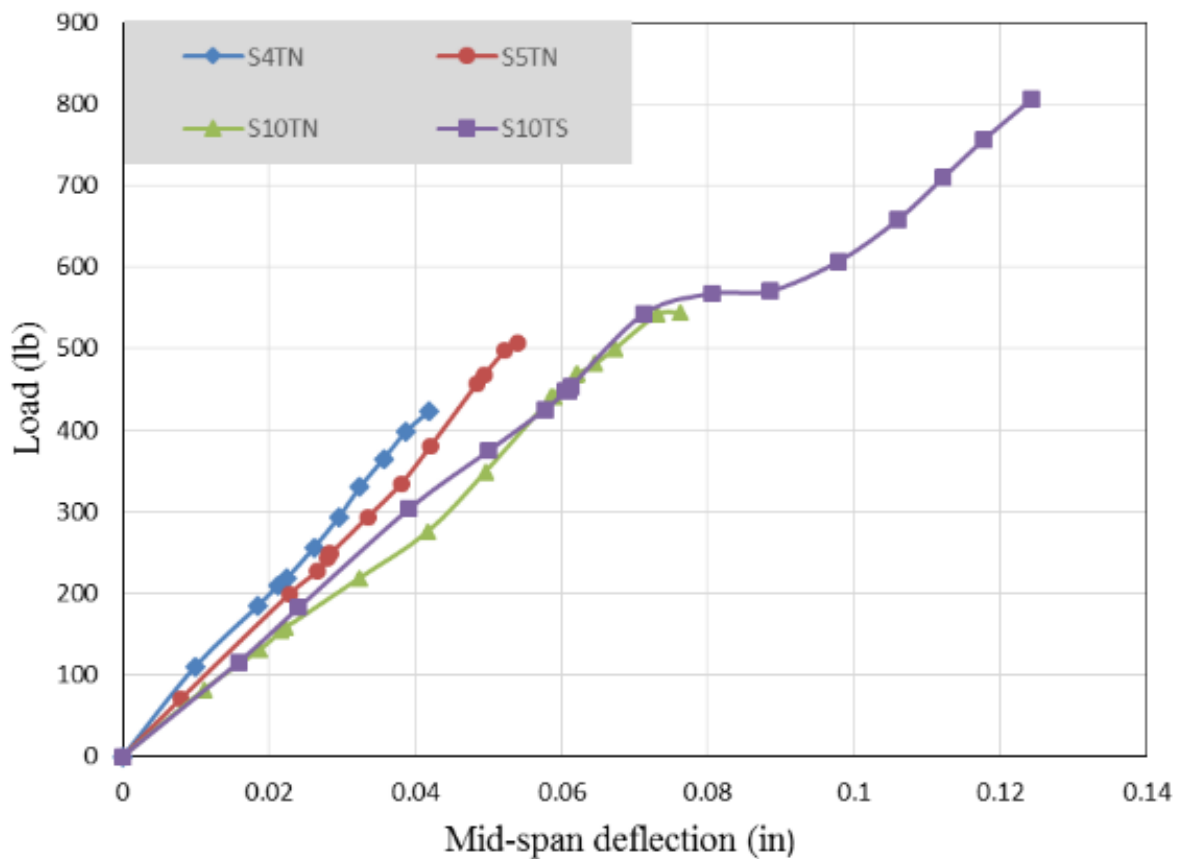


Figure 5. 9 Load versus deflection of AAC beams with basalt tows.

The specimens in series S5TN were reinforced with five tows in the tension zone. The specimens in this group showed the similar linear behavior of the load-deflection response compared to those specimens with four tows (series S4TN). However, the maximum load or the failure load for the specimens with five tows was about 27 % higher than the failure load of the specimens with four tows. Figure 5.9 shows the load versus mid span deflection of series S4TN and S5TN. These specimens also had a mid-deflection increase of 0.05118 inches as shown in Table 5.3. The failure mode of the specimens of series S5TN is shown in Figure 5.10. The specimens in series S10TN had 10 basalt tows. The observed failure mode in this series was shear mode as the specimens were strengthened for flexure only. The average failure load due to shear was 539.5 lb, and the mid-deflection was approximately 0.0787 inch as shown in Table 5.3. Based on the tests performed on those series, the maximum percent of basalt fiber can be used in the section without expecting shear crack was 0.0065 %.

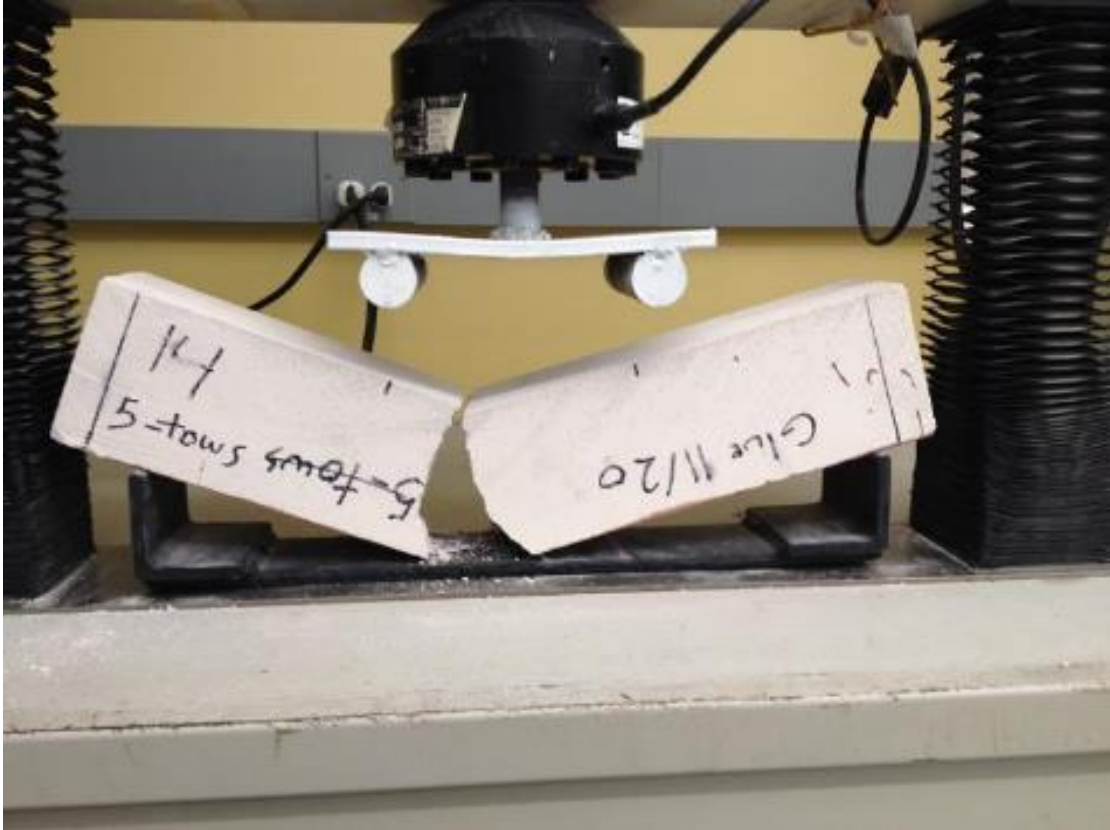


Figure 5. 10 Failure of AAC beams with five tows.

Because of its low shear strength, it was expected to have premature shear failure after increasing the number of the tows in tension. Furthermore, one of the research objectives was also to increase the strength and also provide ductility to the specimens. In order to prevent this premature failure mode, the specimens in series S10TS were strengthened in shear by adding shear reinforcement using basalt fabric. For shear strengthening of the specimens, basalt tows were used similarly to those used for tension. The fiber orientation was parallel to the main reinforcement fiber in tension. It was attached from the edge of the specimen and extended through the shear span of the specimen only. The flexural span

between the two-point loads did not have shear reinforcement to observe the cracks and mode of failure as shown in Figure 5.11.



Figure 5. 11 Failure of AAC beams with five tows and shear enhancement.

The specimens in this series performed better because of the shear reinforcement. The peak load was approximately 1011.6 lb. All the specimens failed in flexural, and they failed by cracks in the flexural span. Several cracks started after the load reached about 0.55 % from the peak load, then they propagated up until they failed. The specimens with this scheme of reinforcement showed a mid-deflection of approximately 0.17 inch which was

represented the maximum deflection in this group. The specimens in this series also showed a good ductility as illustrated in figure 5.9. Yielding can be observed at 562 lb, and it followed by slight hardening ranging from 0.07 inch to 0.09 inch. Furthermore, the load capacity of these specimens showed another increase after reaching a deflection of approximately 0.09 inch, which could be attributed to the compression hardening (due to cell collapse of AAC) and tension stiffening of basalt tows after the tension cracks were taken apart.

### **5.5 AAC Beam Specimens Strengthened with Basalt Fabrics**

Nine series of AAC beams reinforced with basalt fabrics were prepared and tested in this study. Each series has three specimens. Fabrics were easier and faster to apply; however, unlike tows, their geometry is not as straight as the tows.

The specimens in series S13FN specimens were reinforced with 0.5 inch wide basalt fabric that has approximately the same area of fibers as the five tow specimens in series S5TN. Even though the cross-sectional area of the basalt fiber in specimens with five tows and specimens with 0.5 inch width was similar, the specimens reinforced with fabrics showed less load capacity than the ones reinforced with tows. Figure 5.12 shows the load versus deflection response of AAC beams reinforced with fabrics and tows. Figure 5.12 shows that the maximum load observed in the specimens reinforced with 0.5 inch wide fabrics was approximately 418.1 lb which was about 15 % less than the maximum load observed in the specimens reinforced with five tows. This reduction in load capacity was most likely due to the difference in the orientation angle of the fibers between the tows and fabrics and the lack of straightness in the fabrics compared to tows.

The specimens in series S90FN failed in shear as expected due to the large area of fibers in the tension zone. These specimens showed a slightly better performance approximately 7 %, higher load than the specimens in series S10TN which were reinforced with ten tows without shear enhancement.

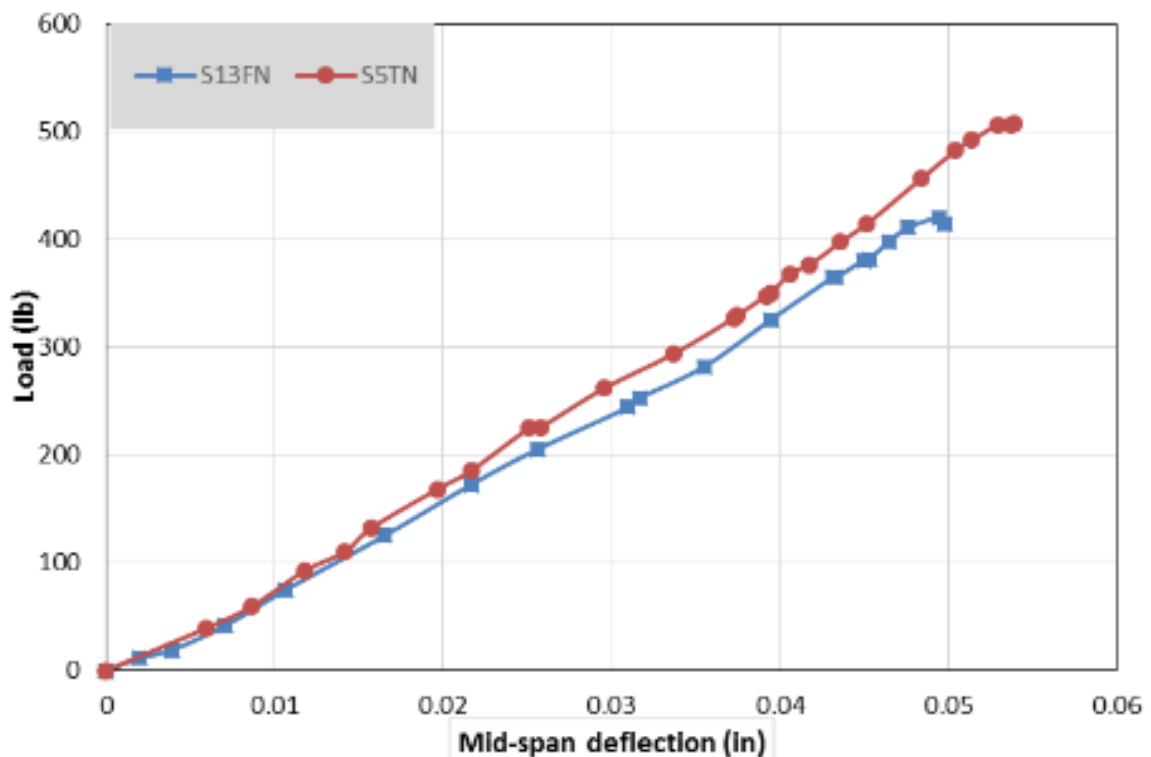


Figure 5. 12 Load versus deflection of specimens reinforced with 0.5 in wide basalt fabric and specimens reinforced with five basalt tows.

Figure 5.13 shows the failure mode observed in series S10TN in shear. The increase in maximum load could be attributed to the extra main strengthening fabric near the support area. The observed peak load in series S90FN was 580 lb, and the mid-deflection at the

peak was 0.063 inch. However, there was no significant effect on the enhancement in the compression to improve the ductility of the specimens in this group as shown in Figure 5.15. The specimens in series S90FS and the remaining series were all reinforced in shear to prevent premature shear failure. The specimens in series S90FS failed in crushing near the support after they reached 899.2 lb as shown in Figure 5.14. The behavior of the specimens was linear up to 90 % of the failure load then it hardening until failure as shown in Figure 5.15. To avoid the premature bearing failure of AAC the remaining series were reinforced with a small layer of fabric in support area to ensure well the distribution of the support stress and avoid the crushing failure of the support.

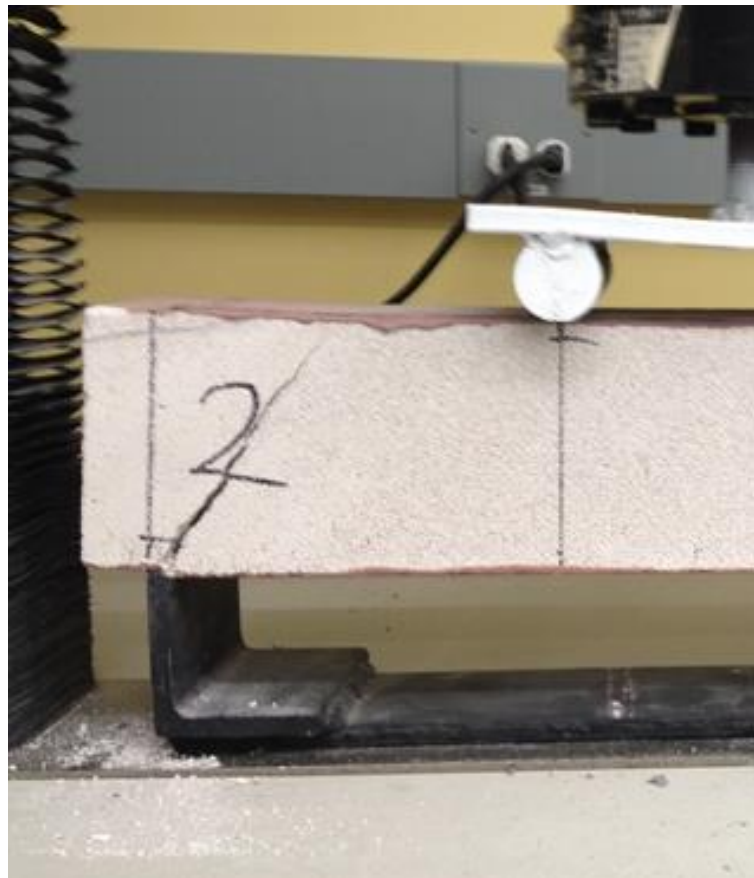


Figure 5. 13 Shear failure of the specimen without shear enhancement.

All the specimens in series S90FS2 failed in flexure. The ultimate load recorded was 1775.9 lb, and the ultimate mid-deflection was 0.196 inch as shown in Figure 5.15. The specimens in this series had the best load deflection performance for groups with the same thickness and this strengthening scheme. The specimens failed in the flexural span, and post-cracking can be observed at approximately 47 % from the ultimate load. The stiffness of the three groups (S90FN, S90FS, and S90FS2) with the same strengthening scheme was approximately the same as shown in Figure 5.15.



Figure 5. 14 Support crushing of specimen without U-wrap.

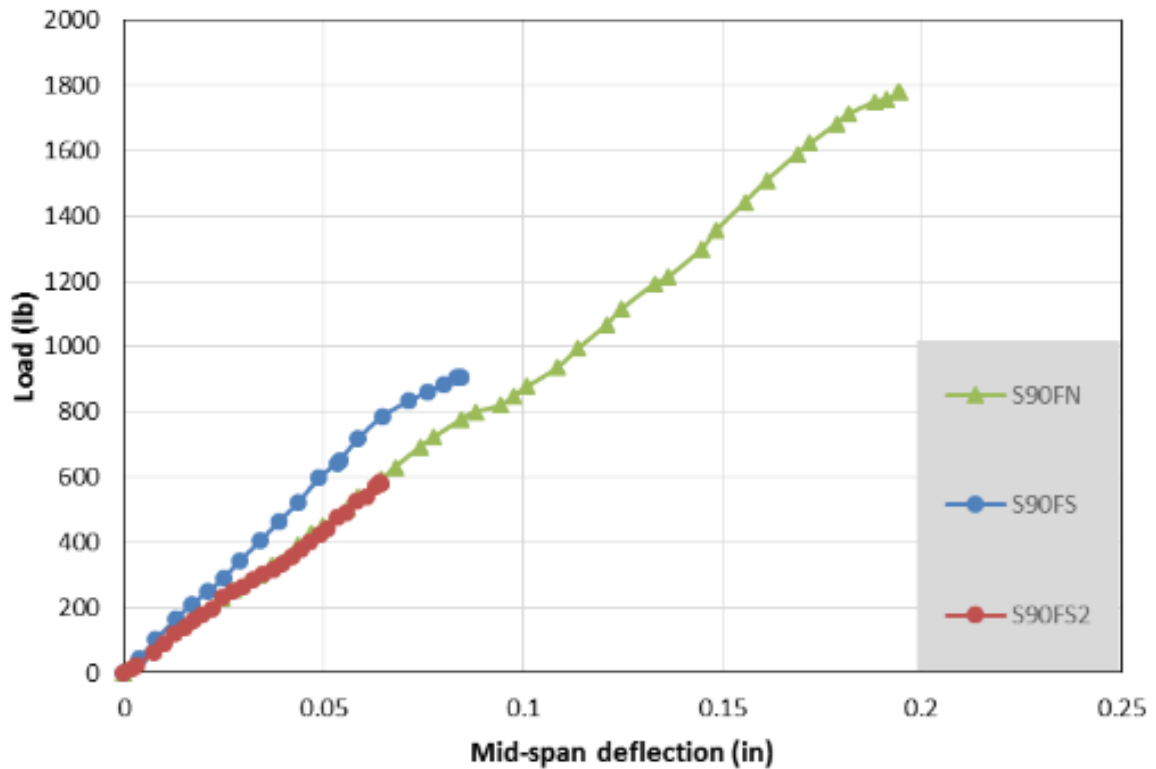


Figure 5. 15 Load versus deflection of AAC beams reinforced with 2 inches basalt fabric.

Referring to the load-deflection curve of series S50FS shown in Figure 5.16. It can be seen that the behavior of the specimens was linear up to approximately 55 % of the maximum load capacity. Beyond that, the load-deflection curve started a slight strain hardening. After that, it went up again to the observed failure load which was 1191.4 lb. The mid-deflection at the first crack was 0.067 inch, and it reached 0.143 inches at the failure point. The specimens in this series showed flexural failure in the flexural span.

In the S50FS2 series, the specimens were reinforced with 2 inches wide basalt fabric. The fabric was divided into two 1 inch wide strips. The fabric strips were both applied in the tension zone but with a space between them. All the specimens in this series failed in flexure, and their load-deflection response was similar to the other series as shown in

Figure 5.16. The observed failure load was 1213.9 lb, and the mid-deflection was 0.153 inch.

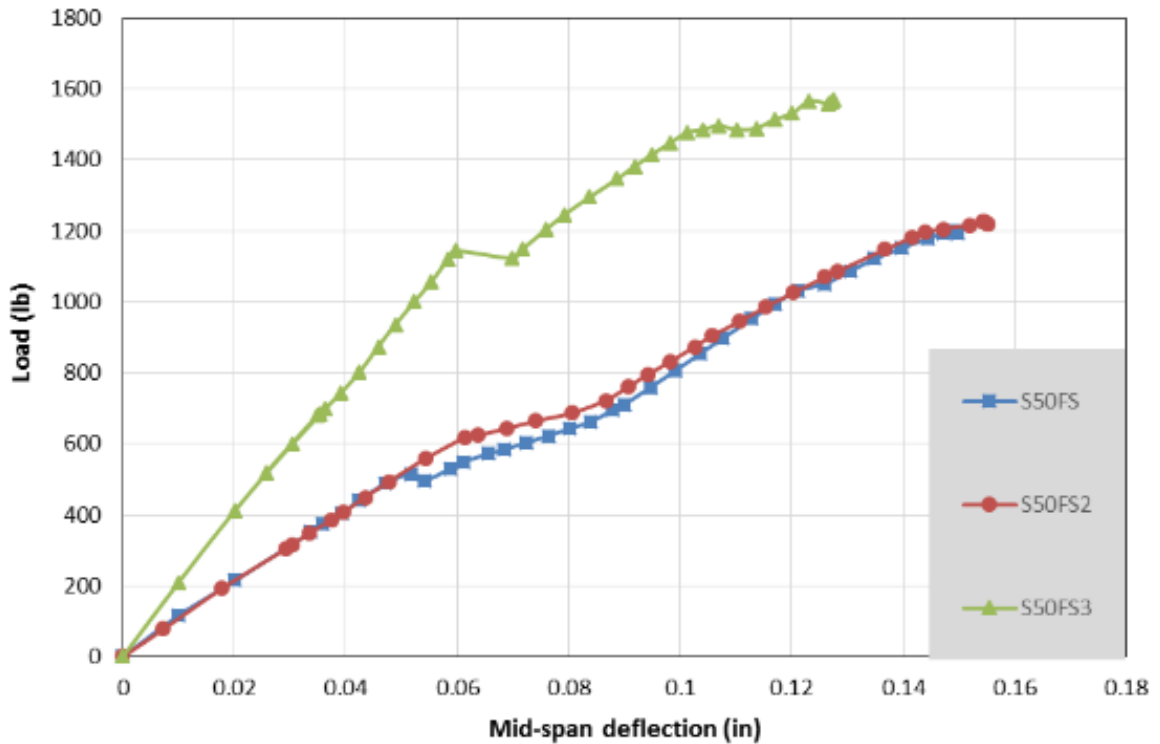


Figure 5. 16 Load versus deflection of AAC beams reinforced with 2 inches wide basalt fabric.

For the S50FS3 series, the capacity of the specimens in this series could be further increased by increasing the thickness of the specimens from 4 inches to 6 inches. Due to the low density of the AAC, increasing the thickness will not increase the dead load considerably in the structure. A considerable increase in load has been observed in this series as shown in Figure 5.16. The load increased approximately 23 %. An increase in stiffness was also observed. The load-deflection behavior was linear increasing up to 70 %

of the failure load, then a slight strain hardening at approximately 70 % from the failure load.

The main objective of the tests in the series S90FS3 was to evaluate whether the beams will perform better when increasing the width of the basalt fabric to 3.5 inches. As shown in Figure 5.17, it was observed that the specimens in this series were performed a better term of load and ductility. The ductility ratio increased approximately by 30 % than series S50FS3. The ultimate load recorded during the test was 2630.2 lb, and the ultimate mid-deflection was 0.165 inch. Post cracking can be observed at approximately 65 % from the maximum load. The failure was governed by flexure.

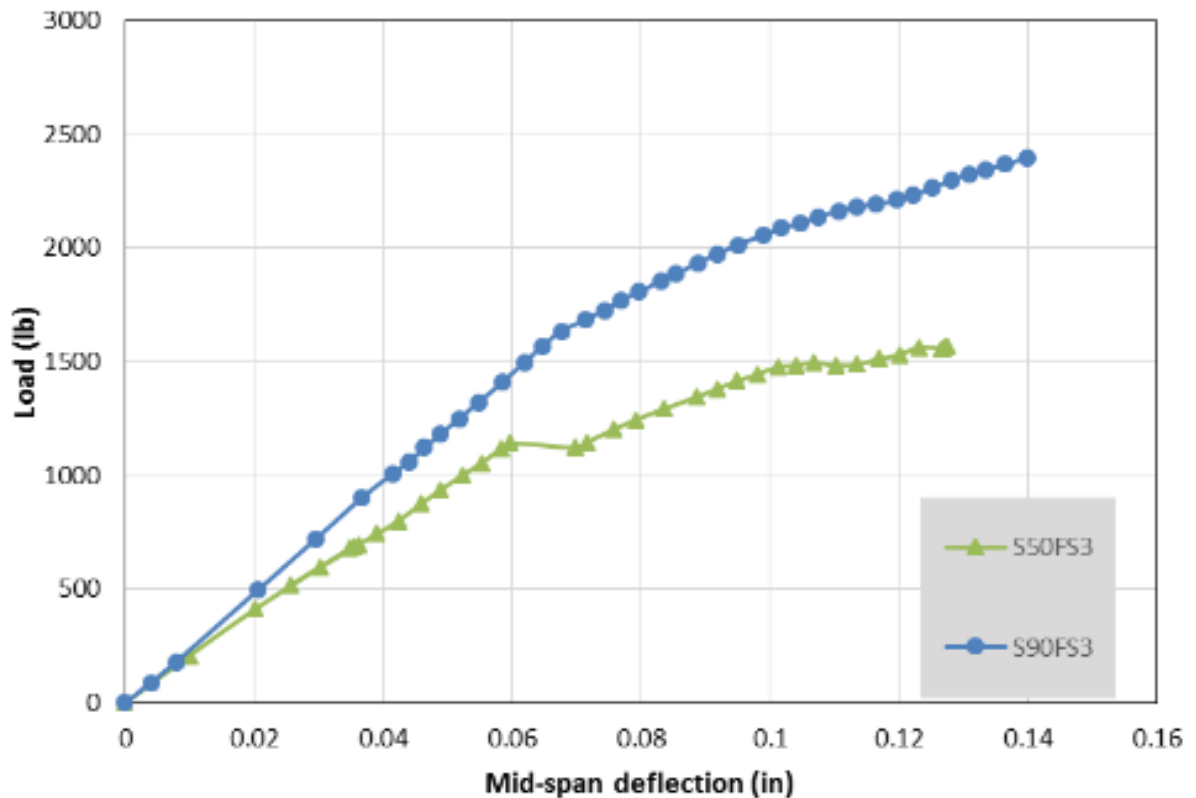


Figure 5. 17 Load deflection of 4 inches X 6 inches AAC beams reinforced with 2 inches and 3.5 inches basalt fabric.

The specimens in series S180FS were reinforced with the largest area of basalt fabrics compared to other series. To achieve this larger area of fabric reinforcement, two layers of 3.5 inches wide fabric were used. The failure mode was a bond failure of the flexural reinforcement near the support followed by the shear crack as shown in Figure 5.18. The specimens in this series had the highest load carrying capacity compared to the other series. The ultimate load recorded was 2360.4 lb, and the mid-span deflection was 0.1118 inch as shown in Figure 5.19. The specimens in this series showed higher stiffness with low ductility.

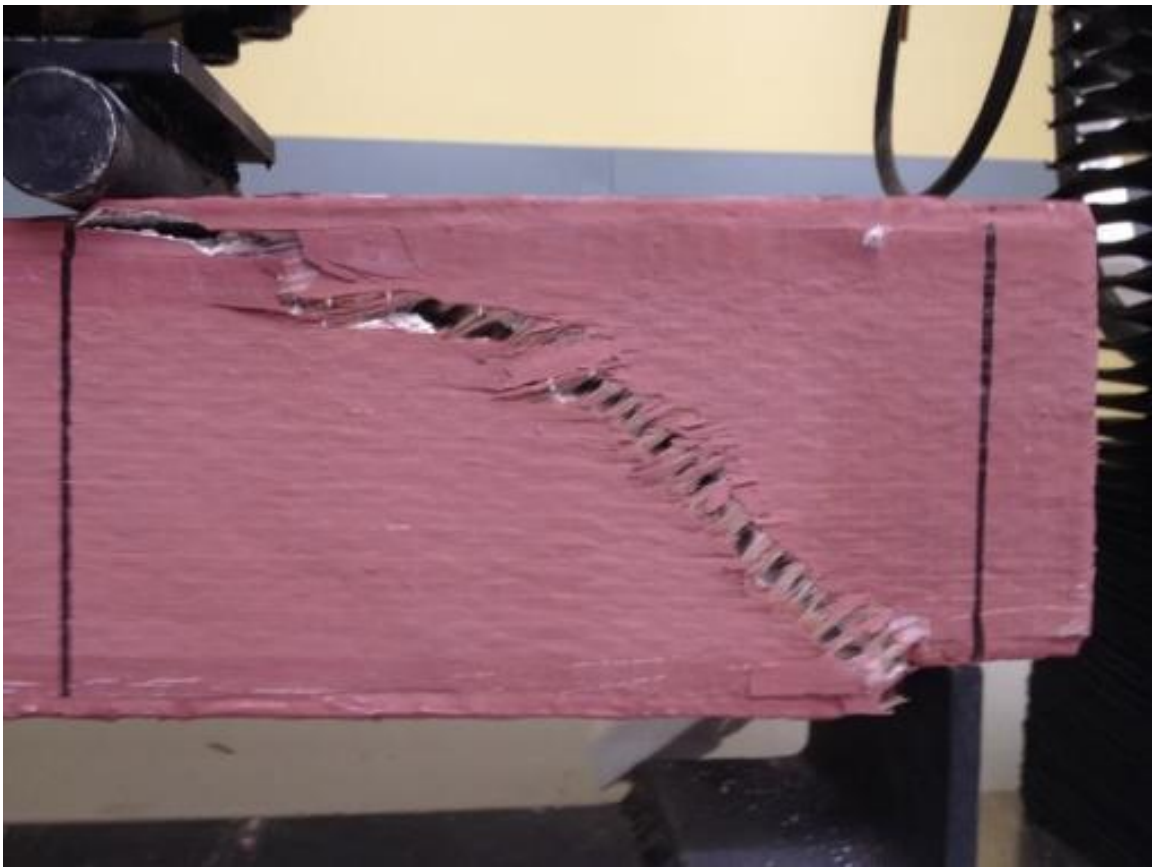


Figure 5. 18 Shear failure of AAC beams reinforced with two layers of basalt fabric 3.5 inches wide.

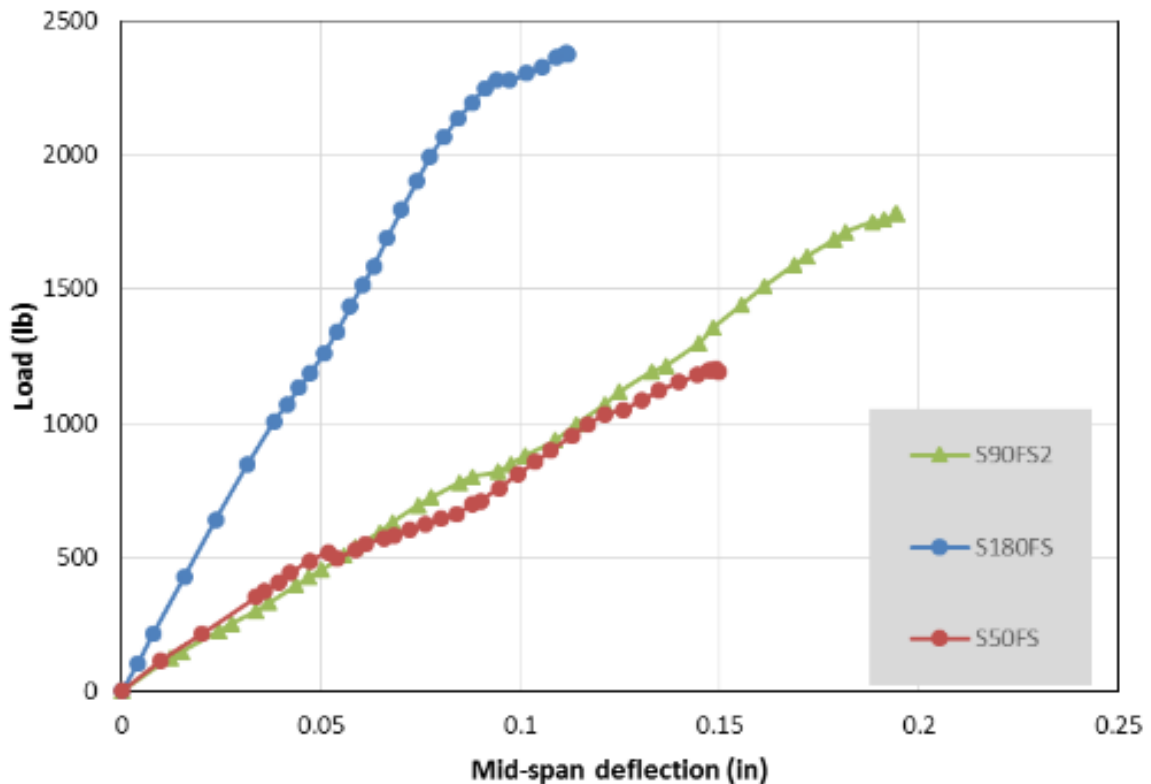


Figure 5.19 Load deflection curve for specimens with 4 inches fabric width.

### 5.6 Ductility of AAC beams

Researchers generally define the ductility of a beam as its ability to sustain inelastic deformation without significant loss in the load carrying capacity of the beam. In some cases, ductility can be defined in terms of deformation or energy. In the case of AAC reinforced with basalt fabrics and tows, the load versus deformation curves did not exhibit clear plastic hardening regions; therefore, the classical definition of ductility could not be applied. An alternative definition of ductility is the ratio of mid-span deflection to the clear span length (Uddin 2007). This definition of ductility was used to compare ductility of the

AAC beams tested in this study. The ductility values of the tested specimens are shown in the last column in Table 5.3.

**Table 5.3 Summary of the test results of AAC beam specimens**

Series description	Series ID	Failure mode	Ultimate load (lb)	Ultimate mid-deflection (in)	Ductility ration= deflection/ span
Plain AAC	S1PN	Flexural crack	285.5	0.00472	0.000262
AAC beams strengthened with tows	S4TN	Flexural crack	422.6	0.03937	0.002187
	S5TN	Flexural crack	494.6	0.05118	0.002843
	S10TN	Shear crack	539.5	0.07874	0.004374
	S10TS	Flexural crack	1011.6	0.17717	0.009843
AAC beams strengthened with fabric	S13FN	Flexural crack	418.1	0.04961	0.002756
	S90FN	Shear crack	580.0	0.06299	0.003500
	S90FS	Crushing at supports	899.2	0.08268	0.004593
	S90FS2	Flexural crack	1775.9	0.19685	0.010936
	S50FS	Flexural crack	1191.4	0.14370	0.007983
	S50FS2	Flexural crack	1213.9	0.15394	0.008552
	S50FS3	Flexural crack	1573.6	0.12756	0.007087
	S90FS3	Flexural crack	2630.2	0.16535	0.009186
	S180FS	Bond-shear failure	2360.4	0.11181	0.006212

## CHAPTER VI

### **PHASE II: THERMAL TEST RESULTS AND DISCUSSION**

Exposure of structural components to high-temperatures may lead to excessive deflections and potentially results in structural failure. AAC panels may be subjected to high temperatures during their service life and therefore the deterioration of Autoclaved Aerated Concrete (AAC) following a high-temperature event is important. It is also important to estimate the residual strength of AAC structural members after exposure to high temperatures to guide engineers and owners when making the decision on whether to retrofit or replace a structural component. For reinforced AAC beams, the degradation in strength and stiffness is required for both: AAC and basalt fibers.

As discussed in Chapter IV, Phase II was comprised of five series temperature (23 °C), and after exposure to different sets of elevated temperatures. Four series of AAC beams were tested for flexural, and the fifth series was cube AAC material tested for compression at an elevated temperature up to 1000 °C. Wall panels, lintels, and roof panels are the most common structural AAC components used in building construction after reinforced them with steel wire mesh. However, the tensile and flexural strength of AAC panels are very low, and bonding of structural steel to AAC is weak due to the high porosity of AAC. To maintain this improved bending strength at high temperatures, basalt tows as main reinforcement, and an inorganic matrix was used for strengthening and bonding the basalt tows to the AAC beams. The test results showed that the degradation of bending strength

of AAC beams strengthened with basalt composites at high temperatures was relatively small compared to plain AAC beams.

In this phase of the experimental investigation, the thermal performance of coated and uncoated plain AAC material was investigated in compression and flexure. The coating material used in this study is an inorganic matrix which was described in Chapter IV. Also evaluated in this phase, the thermal performance of AAC beams strengthened with inorganic basalt composites was evaluated at elevated temperatures.

The results presented in this chapter (VI) deal with the effect of elevated temperature on the mechanical properties of AAC beams reinforced with basalt tows and attached to the AAC using inorganic matrix. Background information on the basic behavior of the inorganic matrix at high temperature was presented in Chapter II. This chapter focuses on the flexural behavior of AAC beams at higher temperatures.

## **6.1 RESEARCH SIGNIFICANCE FOR THERMAL PERFORMANCE**

For practical applications, AAC is used as a main structural element after reinforcing it with steel wire mesh to provide the required flexural strength. In the long run of the structure, and due to the porosity of the AAC, the steel tends to corrode. However, this will reduce the expected time life of the structure. Moreover, the reinforcing steel will not take part for enhancing the shear strength of the element. That will produce a thicker element to provide the requisite shear requirements. The aim is to replace the reinforcing steel with efficient and low cost FRP, and produce a system has a feasible fire resistant properties. Basalt tows have been chosen to reinforce the AAC beams for their favorable mechanical and thermal properties.

Even though organic resin systems have appropriate advantages and they used successfully for decades, some of their most detrimental features include the increasing brittleness and deterioration that occur naturally as a result of the breakdown of the organic system over relatively small periods. Moreover, the organic resin has a low ability to maintain the required bond in high-temperature occasions. However, the nano-inorganic composite has been adopted in the experiment to provide the bond between the FRP and AAC and to provide the fire protection to maintain the required strength.

The natural behavior of basalt fiber and AAC is brittle; however, the combination of them showed reasonable results in terms of mechanical properties. In addition, this lightweight combination has a perspective to speed up the construction and reduce the required intensive labor.

## **6.2 PREPARATION AND TESTING OF SPECIMENS**

This experimental investigation was conducted at the material engineering laboratory of Rutgers, the state university of New Jersey. The AAC blocks used in the experimental program were commercial type products provided directly from the manufacturer. In this experiment, a total of five series was prepared and tested. Four series of beams were tested under different levels of elevated temperatures to determine the failure loads, flexural stiffness, and displacement. A fifth series was cube AAC material, and it was tested in compression with different levels of elevated temperature. The specimens in the fifth series were 4 inches x 4 inches x 4 inches plain AAC cubes. The experimental program was also designed to evaluate the effectiveness of the basalt strengthening system for AAC. The first series (S1-P) included plain AAC beams and had four sets of specimens: S1-P1, S1-

P2, S1-P3, and S1-P4. It was exposed to different sets of elevated temperatures up to 300 °C. The second series (S2-CP) included plain AAC beams with similar dimensions of the (S1-P); however; the beams in this series were coated with an inorganic resin in reason of study the effect of inorganic resin on modulus of rupture of AAC material. This series had six sets of specimens: S2-CP1, S2-CP2, S2-CP3, S2-CP4, S2-CP5, and S2-CP6. It was exposed to different sets of elevated temperatures up to 600 °C. The specimen dimensions for these two series (S1-P, and S2-CP) were 2 inches x 4 inches x 8 inches (the clear span was 6 inches). Two layers of inorganic matrix were applied to the whole surface of the beams in series S2-CP with 24 hours waiting time to apply the second layer. A hand brush was used to apply the inorganic matrix. The third and the fourth series for flexural tests were (S3-P) for plain AAC beams and (S4-BT) for AAC beams reinforced with basalt tows. The dimensions of the beams for series three and four were 4 inches x 4 inches x 14 inches. The clear span of the beams in series (S3-P) and (S4-BT) was 12 inches. The beam length in series (S3-P, and S4-BT) was limited to 14 inches due to the space limitations of the furnace. Series S3-P included four sets: S3-P1, S3-P2, S3-P3, and S3-P4 that were tested at 23 °C, 100 °C, 200 °C, and 300 °C. Similarly series (S4-BT) had four sets that were tested at 23 °C, 100 °C, 200 °C, and 300 °C. The compression series was the fifth series and it was included eight sets: S5-C1, S5-C2, S5-C3, S5-C4, S5-C6, S5-C7, and S5-C8 that were tested at 23 °C, 100 °C, 200 °C, 300 °C , 400 °C, 600 °C, 800 °C, and 1000 °C respectively. The various sets of exposed temperature for each series was selected depending on results of the retain strength. The tests were stopped when the strength of the material dropped by 60 % or more. Each set in each series had three specimens. The reported results were the average of the three tested specimens in the particular set. In Table

6.1, summarization for the various series tested in this study. The AAC beams were selected from one pallet and the specimens of each set of beams were made from the same block to ensure all the beams had the identical properties and reduce the effect of the material composites variations. The beams carefully cut using table saw and cleaned prior to the application of the inorganic resin material. The dimension of the cross section measured using digital calibrator had an accuracy within  $\pm 0.025$  in. Hand impregnation was used to wet the basalt tows and attach them to the AAC beams with reason of simulate the field application. The tows were attached parallel to the longitudinal direction of the beams, and they placed carefully to avoid the effect of skew angle of the fibers. After applying the basalt tows, the beams left to cure in room temperature for three weeks prior to testing.

Table 6. 1 Summary of the properties of the various test series in the experimental program

Series	Specimen Dimension (width X depth X span) (in)	Specimen Type	Test Type	Temperatures (°C)
S1-P1 to S1-P4	4 x 2 x 6	Plain beams	Flexure	23, 100, 200, 300
S2-CP1 to S2-CP6	4 x 2 x 6	Plain beams coated with inorganic resin	Flexure	23, 100, 200, 300, 400, 600
S3-P1 to S3-P4	4 x 4 x 12	Plain beams	Flexure	23, 100, 200, 300
S4-BT1 to S4-BT4	4 x 4 x 12	Reinforced beams with basalt tows	Flexure	23, 100, 200, 300

S5-C1 to S5-C8	4 x 4 x 4	Plain cubes	Compression	23, 100, 200, 300, 400, 600, 800, 1000
----------------	-----------	-------------	-------------	--

---

### 6.3 FURNACE SPECIFICATION AND HEATING PROCESSES

After the specimens cured in the room temperature, each set had put in the furnace, and the specimens have heated to the required temperature. The furnace used in this investigation was high performance Vulcan 3-1750 with internal muffle dimensions 14 inches width, 10 inches high, and 13 inches depth. The maximum heating capacity of the furnace was 1100 °C with 5 °C precision. The muffle temperature uniformity was 8 °C. The furnace has a programmable controller with nine three-stage programs (six segments each) and one program with a single temperature hold. The furnace is illustrated in Figure 6.6. It also has wide programmable linear temperature rates both positive and negative (0.1 to 40 °C/minute). The maximum relative humidity of the furnace was 80%. The performance curve for heating and cooling of the furnace is shown in Figure 6.7. The temperature for each series was applied gradually starting from the room temperature by dividing the final temperature into three ramps (R1, R2, and R3). In each ramp, the temperature rate was 10 °C/min, and there was a corresponding temperature for each ramp (T1, T2, and T3). For each ramp, also there was a holding time (H1, H2, and H3). The purpose of this holding time was to allow the temperature reach the core of the specimens and ensure a well distribution for the temperature across the section of the specimen. The final holding time for all series was 60 minutes, and the total time for each series shown in Table 6.3. The heating in all series has started from the room temperature to the targeted exposure temperature. A Veho Microscope was used to capture the effect of heating on the

appearance of the AAC and measure the width of the developed cracks. When the temperature inside the furnace reaches 100 °C, 200 °C, 300 °C, 400 °C, 600 °C, 800 °C, and 1000 °C, respectively, the specimens held in this temperature for 1 hour then the furnace stopped, and the door of the furnace opened to cool the specimens with air.

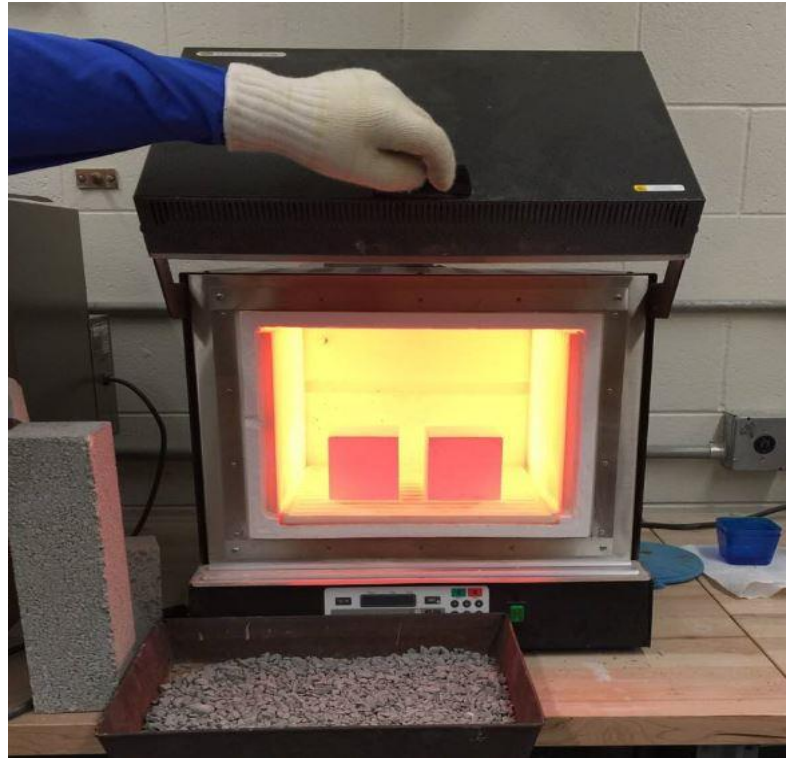


Figure 6. 1 Furnace used in this experiment

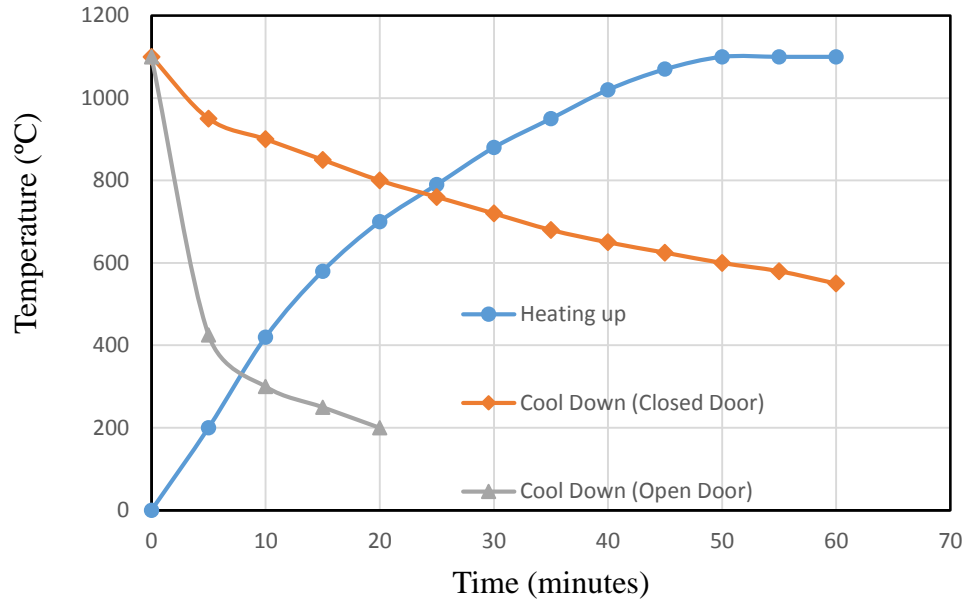


Figure 6. 2 Heating performance rate for the furnace used to heated the specimens

Table 6. 2 Heating process and total holding time in furnace

Temperature (°C)	Ramp temperature (°C/min.)	Temperature for each ramp (°C)	Holding time for each ramp(min)	Total time inside the furnace(min)	
23	R1	0	T1	23	--
	R2	0	T2	23	--
	R3	0	T3	23	--
100	R1	10	T1	50	10
	R2	10	T2	70	10
	R3	10	T3	100	60
200	R1	10	T1	70	10
	R2	10	T2	140	10
	R3	10	T3	200	60
300	R1	10	T1	100	10
	R2	10	T2	200	10
	R3	10	T3	300	60

	R1	10	T1	130	10	
400	R2	10	T2	260	10	112
	R3	10	T3	400	60	
	R1	10	T1	200	10	
600	R2	10	T2	400	10	137
	R3	10	T3	600	60	
	R1	10	T1	260	10	
800	R2	10	T2	530	10	157
	R3	10	T3	800	60	
	R1	10	T1	350	10	
1000	R2	10	T2	700	10	177
	R3	10	T3	1000	60	

---

#### **6.4 TEST SET UP AND PROCEDURE FOR HEATED BEAMS IN FLEXURE**

The flexural strength of the AAC beams was measured using the third-point loading method following ASTM C78M. Figure 6.9 shows a schematic of the third-point-loading test method and beam dimensions for series S3P and S4BT, while Figure 6.10 shows a schematic of the third-point-loading test method and beam dimensions for series S1P and S2CP. For the beams that were tested at high temperatures, the beams were heated in the furnace as described earlier; then they were left to cool by air. Both the shear span and flexural span were 4 inches for beams in series S3P, and S4BT, while they were 2 inches for series S1P, and S2CP. An MTS flexural machine was used to conduct all the flexural tests using a 10 kips load cell for series S3P and S4BT, and 1 kips load cell for series S1P and S2CP. The load was applied to the beams at a continuous slow, and uniform rate load of 0.05 in/min. One vertical linear variable differential transformer (LVDT) with an

accuracy  $\pm 0.1\%$  for the full range was attached at the mid-span of each beam to measure deflections. The applied load was recorded by the MTS data collection system and was plotted versus the measured mid-span deflection. The mode of failure was observed and recorded. The dead load effect of the beam was negligible and was neglected.

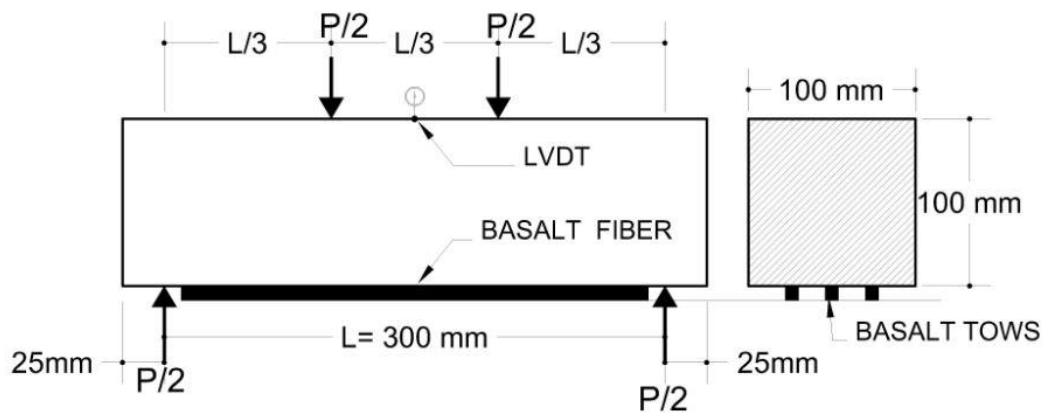


Figure 6. 3 Specimen dimension and load application for AAC Series S3P and S4BT

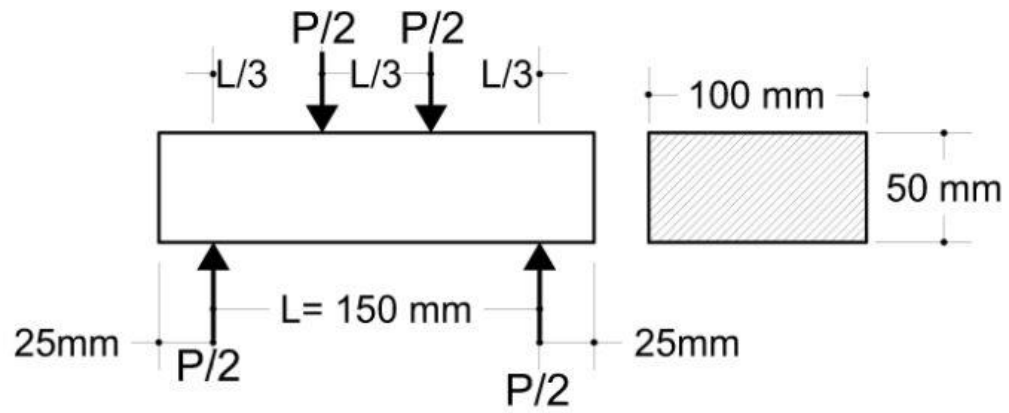


Figure 6. 4 Specimen dimension and load application for AAC Series S1P and S2CP

## 6.5 RESULTS AND DISCUSSION

This section summarizes the test results from compression and flexural tests of plain, coated, and reinforced AAC elements subjected to elevated temperatures.

### 6.5.1 Effect of high temperatures on the compressive strength

Compressive strength tests were conducted to determine the effect of different temperatures on the compressive strength of the AAC. Eight series of 4 inches cubes were prepared and tested at eight different temperatures as shown in Table 6.1. The selected temperatures were 23 °C (room temperature), 100 °C, 200 °C, 300 °C, 400 °C, 600 °C, 800 °C, and 1000 °C. For each series, three cubes were tested, and the compressive strength was averaged. The compressive strength was performed in accordance with ASTM C 39. The variation of the compressive strength for all three specimens in the same series was less than 4%. This variation in results was similar in all series. The compressive strength and the relative compressive strength as a function of the applied temperature increase were shown in Table 6.4. The table also shows comparisons with results from other researchers. For the control series (unheated cubes), the results showed that the compressive strength was 580 psi. At 100 °C, there was a slight increase in compressive strength (about 1%), and there were no noticeable cracks as shown in Figure 6.12(b). At 300 °C, the compressive strength increased by about 8 % compared to the control series as shown in Table 6.4. The maximum compressive strength of all the tested series was 647 psi observed at 400 °C. The compressive strength was slightly developed starting from the room temperature up to the 600 °C. At 600 °C, the compressive strength was higher than the control strength by about 9 %. A loss in strength was observed beyond 600 °C. At 800 °C, a reduction of 7% in compressive strength compared to the control specimens was observed. It seems that the

chemical structure of the AAC starts to break down at 200 °C where the first cracks became visually observable at this temperature as shown in Figure 6.12(C). The average width of these cracks was approximately 0.004 in. The width of the cracks remains slightly increased as the temperature was increased to 600 °C as shown in Figures. 6.12(c), 6.12(d), 6.12(d) and 6.12(f). At 800 °C, the crack widths have increased to about 0.008 in, and more spalling developed at this temperature as shown in Figure. 6.12(g). These cracks have not had a significant effect on the compression strength of the AAC specimens. However, the amount of cracks increased as the temperature increased above 600 °C and the drop in compressive strength was significant as shown in in Figure 6.11. At 300 °C, the color of the specimens started to change and became darker, changing from white to light grey. The color of the specimens at 800°C became bright due to the decomposition of the chemical phases of silica and lime (Keyvani 2014). At 1000 °C, the compressive strength has dropped significantly by approximately 52.4% less than the control samples and spalling and cracking was observed across the whole area of the cubes as shown in Figure 6.14.

Figure 6.11 showed the relative compressive strength tested in this study as a function of the elevated temperature as well as test results from other researchers (Tanaçan et al. 2009). In general, the tested samples showed a good convergence with the samples has tested by Tanaçan. The first four series behaved similarly by increasing in strength with slight differences in relative compressive strength attribute to the test conditions. The values of the relative strength for 200 °C, and 300 °C series were fallen lower that Tanaçan values by about 5 %. At 400 °C, the strength kept developed, however, in the other study it started lower by 7 % than the tested specimens in this experiment. In both studies, the maximum relative compressive strength was 1.12, however, in the current experiment, it has occurred

at 400 °C, while in the other study at 200 °C. At 600 °C, the reported relative strength was 2 % lower than the other study, and at 800 °C it was 4 % lower. The reported compressive strength at 1000 °C was less than the one reported by Tanaçan by 16 %.

In another study (Israngkura 2011), the results were carried out in current experiment showed a comparable results with the study of relative compressive strength up to 400 °C, then the results diverged, and the referred study reported a sharp lower results for the compressive strength after 400 °C, then the results stabilized at 800 °C to 1000 °C, and the retained compressive strength was 16 % from the original strength. Unlike in the current experiment, the strength increased gradually up to 600 °C; then the retained strength was 93 % of the original strength at 800 °C. The behavior of the AAC material was not clear in this study for temperatures between 400 °C to 800 °C because there were not any reported data at that range of temperatures.

The variation in the reported data from current experiment and other studies may attribute to many reasons such the variation in composite of the AAC material or the autoclaving process, the lab conditions, the differences in test approach, the sequence or procedure of the test, using different loading or heating rates, and techniques used for the measurements. Comparing the results with the reported results for normal strength concrete (Kodur 2008) showed that the retained relative strength of the AAC material was higher than the normal strength concrete Figure 6.11, and the drop in strength for NSC started after exposed to 100 °C, however, in AAC was started after exposed to 600 °C. Knowing, the actual strength of concrete higher than the Actual strength of AAC by about 8 times.

Table 6. 3 Summary of the test results for the compressive strength for this study and from previous studies

Temperature (°C)	Compressive strength (MPa)	Increase or decrease in compressive strength (%)	Relative compressive strength	Relative compressive strength for Tanacan (2009)	Relative compressive strength for Israngkura (2011)	Relative compressive strength for Kodur-NSC (2008)
23	580	0	1	1	1	1
100	589	1.4	1.01	1.06	10.6	1
200	618	6.6	1.07	1.12	10.6	0.95
300	625	7.6	1.08	1.06	10.3	0.85
400	647	11.6	1.12	1.04	1.01	0.75
600	632	9	1.09	1.11	-	0.45
800	503	-6.5	0.93	0.97	0.16	0.15
1000	275	-52.4	0.48	0.64	0.15	0.04

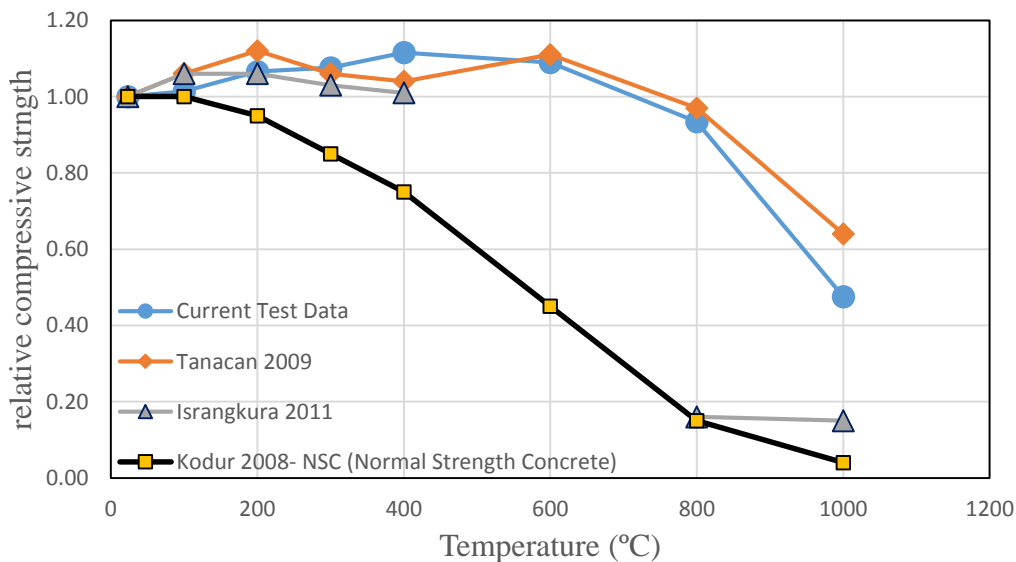


Figure 6. 5 Variation of the relative compressive strength of AAC as a function of temperature from this study and other studies

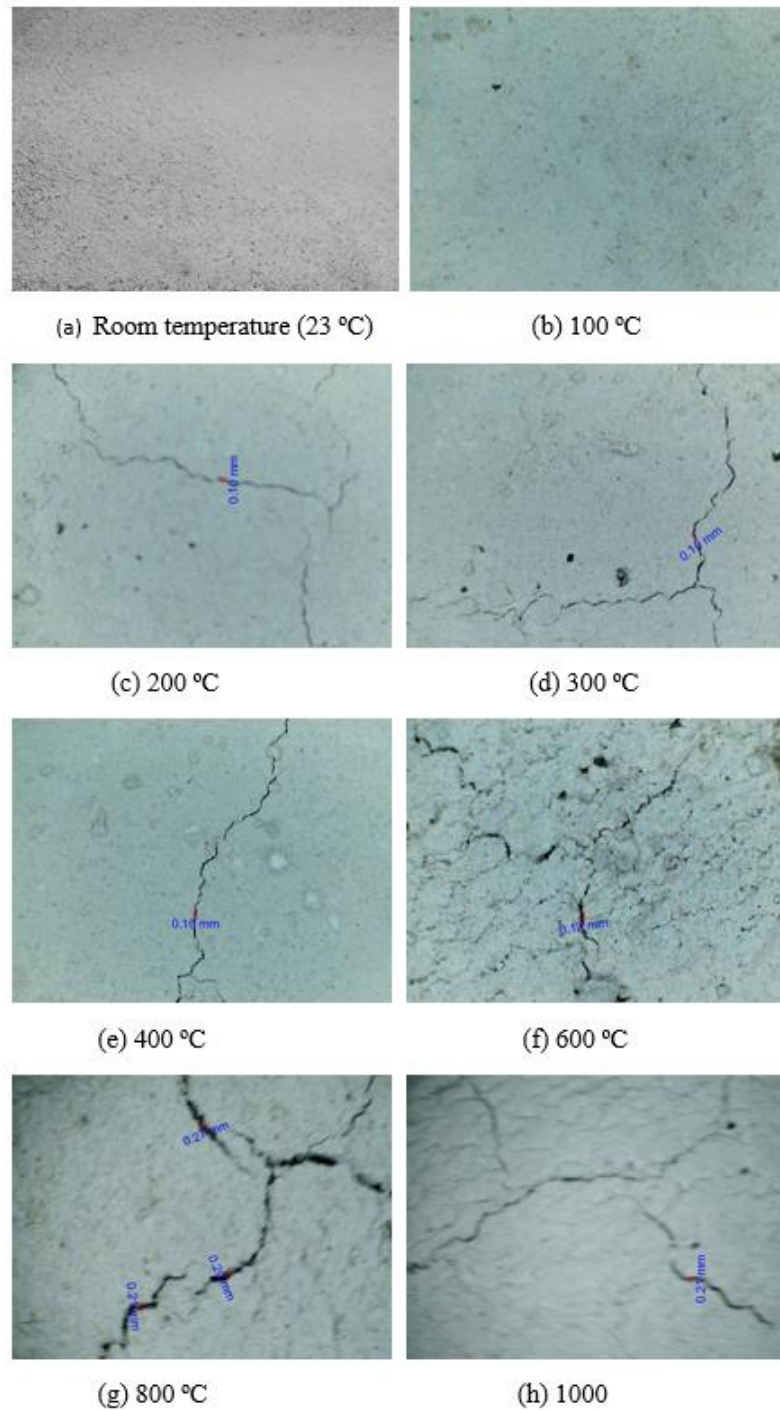


Figure 6. 6 20x magnifying picture for AAC cubes at different temperatures



Figure 6. 7 (a). AAC cubes in the furnace at 1000 °C before being tested in compression

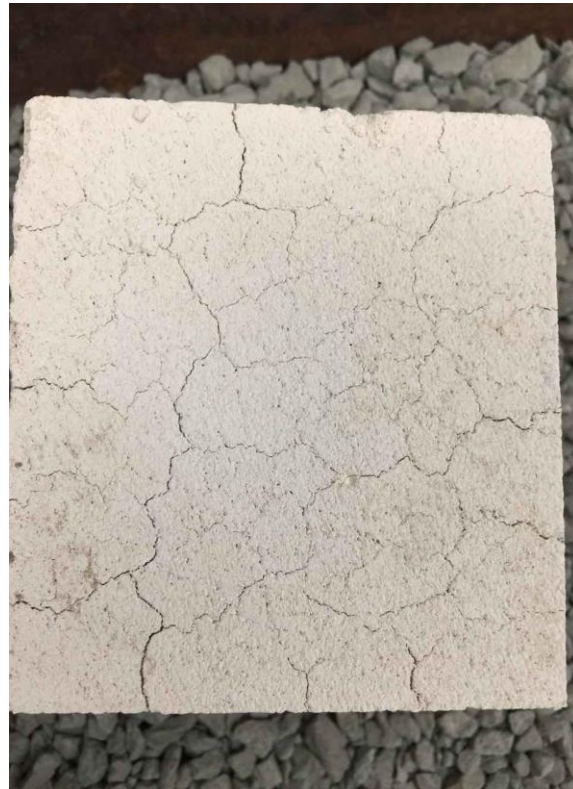


Figure 6. 8 Spalling and cracking in cubes after heated for 1000 °C and cool by air.

### 6.5.2 AAC Compressive Strength – Prediction Model

Based on the experimental test data obtained in this study, a constitutive relationship for the degradation in the compression strength of the AAC with increasing temperature between 23 °C to 1000 °C is shown in Figure 6.15. The variation of the results in the relative strength of AAC was not large as noticed in Figure 6.11; however, the developed empirical compressive strength-Temperature model consider the lower bound of the reported results to ensure more conservative in reduction strength. The test data did not show any reduction in the compressive strength up to 600 °C. This is demonstrated in the proposed model in Eq. 1. Between 600 °C to 800 °C, the test data showed a reduction in compression strength approximately about 7% or the control strength (93% of the control strength). The proposed model suggests 90 % of the compressive strength of the original strength is retained between 600 °C to 800 °C. For temperatures 800 °C up to 1000 °C, the degradation is a compressive strength with temperature was modeled based on experimental data and was expressed in (Eq. 1).

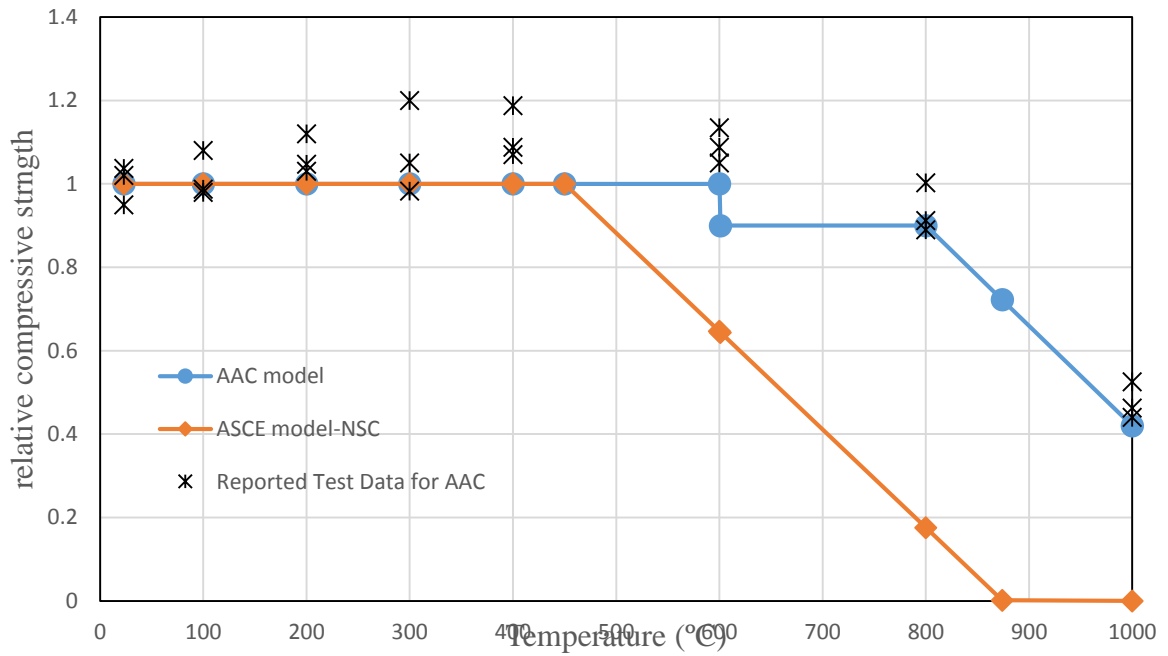


Figure 6. 9 Variation of compressive strength with Temperature for AAC

$$f'_{AAC,T} = \begin{cases} f'_{AAC} & 23^{\circ}\text{C} \leq T \leq 600^{\circ}\text{C} \\ 0.9f'_{AAC} & 600^{\circ}\text{C} < T \leq 800^{\circ}\text{C} \\ f'_{AAC} \left[ 2.4 \left( \frac{1000 - T}{1000} \right) + 0.42 \right] & 800^{\circ}\text{C} < T \leq 1000^{\circ}\text{C} \end{cases} \quad (1)$$

Where:

$f'_{AAC,T}$  = compressive strength of AAC at temperature T (MPa),

$f'_{AAC}$  = compressive strength of AAC material at room temperature (MPa),

T = exposure temperature (°C).

### 6.5.3 Effect of high temperatures on the flexural strength of AAC

The deterioration in flexural strength with increasing temperature of AAC beams was much higher than the compression strength. This can be attributed to flexural cracks forming and then propagating quickly as the temperature rises. The observed average modulus of rupture of the control plain AAC beams tested in flexure from Series S1P1, S2CP, and S3P1 at room temperature (23 °C) were 116, 114, and 113 psi respectively as shown in Table 6.5. These values were consistent with the ACI526 prediction formula for the modulus of rupture which gives a value of 115 psi for AAC with a compression strength of 580 psi. The flexural strength of AAC at room temperature observed in this study was approximately about 20 % of the compressive strength (compared to 10 % for normal strength concrete). As expected, the load-deflection curves for all three series were linear up to failure with single crack forming in the flexural span zone. Figure 6.16 shows the load deflection curve for series S3P for various temperatures (plain AAC 4 in x 4 in x 12 in beams). The test results showed that the flexural strength 100 °C was about 54 % less than that of the control set. A reduction in stiffness was also observed as well. Even though the plain series S1P and S3P had different cross-sectional areas, the technique used for the thermal load application has not shown differences in the flexural strength variation for both series due to temperature increase. However, the differential thermal expansion between the exterior surfaces of the AAC beams and the core may have resulted in larger thermal cracks in the specimens with the larger exposed area. Comparing the decrease in flexural strength of specimens S1P2 heated at 100 °C and specimens S1P3 heated at 200 °C relative the control specimens, it was observed that the further reduction in strength from S1P2 to S1P3 was much less than the reduction in strength from the control set S1P1

to the second set S1P2. As mentioned earlier, the maximum load for set S1P1 was about 54 % less than the control set, while the maximum load for set S1P3 was about 19 % less than S1P2 (or 64 % less than the control set). The specimens in set S1P4 (heated at 300 °C) had a maximum load about 13 % less than to the specimens in set S1P3 (or approximately 67 % less than the control set). At 300 °C, the cracks were visually noticeable starting at 100 °C. The test was stopped at 300 °C because the beams exhibited significant loss of strength (69 % less strength compared to the control beams). Similar flexural strength reductions were observed in series S3P suggesting that the difference in the cross-sectional area did not have a significant effect on the degradation of flexural strength with temperature increase.

For sets S1P1, S1P2, and S1P3 the coefficient of variation for the peak load from the three specimens tested in each set was less than 3 %, however, for set S1P4, the coefficient of variation was about 11 % which may have been higher was due to the higher applied temperature. For sets S3P1, S3P2, and S3P3 the coefficient of variation for the peak load was less than 4.5 %, however, for set S4P4, the coefficient of variation was about 10 % which also may be attributed to higher fluctuations due to higher applied temperature. The existence of cracks at elevated temperature reduces the effective cross-sectional area of the AAC beams and existence of tensile stress causes expansion of cracks. The impact of cracks on flexural strength degradation is more significant than compressive degradation. This may be explained by the presence of axial loads in compression which reduces the tensile stresses at crack locations compared to flexural loading.

The beam specimens in series S2CP were coated with the inorganic matrix to mitigate the drop in the flexural strength of the AAC beams with temperature increase. The beams were

coated with two layers of an inorganic matrix using hand layout to apply the matrix. The observed results showed that coating the beams with the inorganic matrix prevented the degradation of flexural strength at higher temperatures up to 300 °C as shown in Figure 6.17. The possible explanation is that the matrix filled some of the voids on the AAC beams delaying the heat radiation and transfer into the AAC beam section. Beyond 300 °C, the strength had dropped about 18 % at 400 °C, and 58 % at 600 °C as shown in Table 6.5. The variation in results were less than 4 % for all temperatures sets in this series.

Table 6. 4 Variation of flexural strength with temperature

Temperature (°C)	Flexural Strength (MPa)			Reduction in Strength %		
	S3P	S1P	S2CP	S3P	S1P	S2CP
23	113	116	114	0.0	0.0	0.0
100	51	53	114	54.8	54.3	0.2
200	41	42.3	113.3	63.3	63.6	0.7
300	36	39	113	68.4	66.6	1.3
400	-	-	93.3	-	-	18.3
600	-	-	48	-	-	58.2

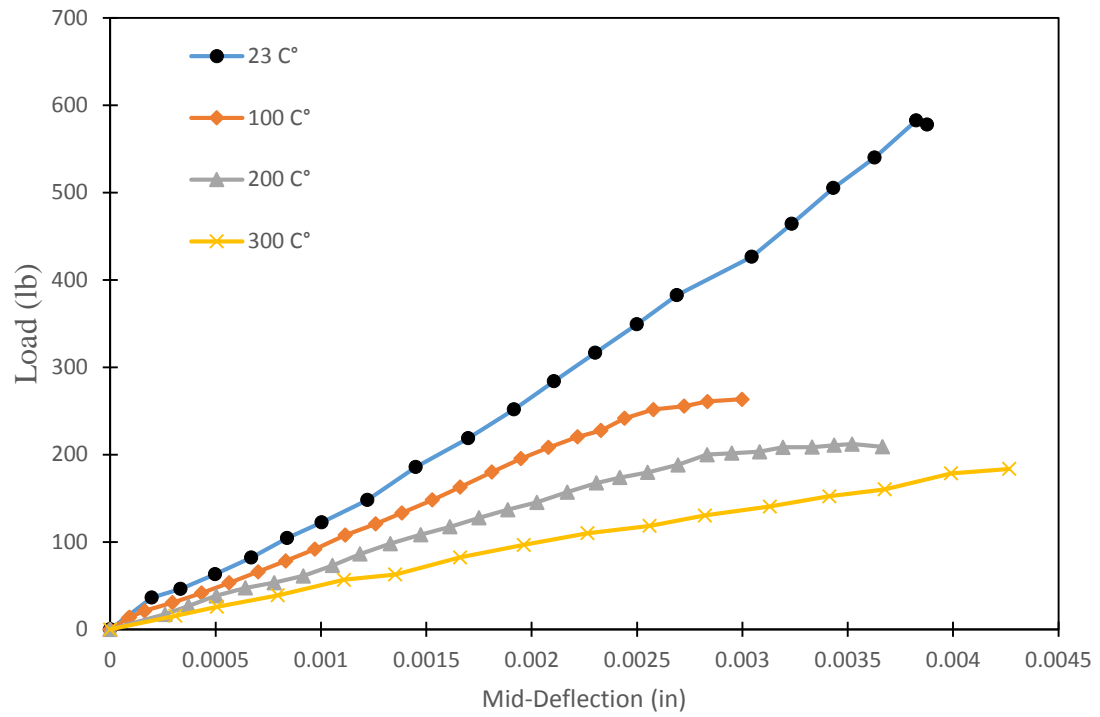


Figure 6. 10 Load-deflection curves for plain AAC beams series S3P

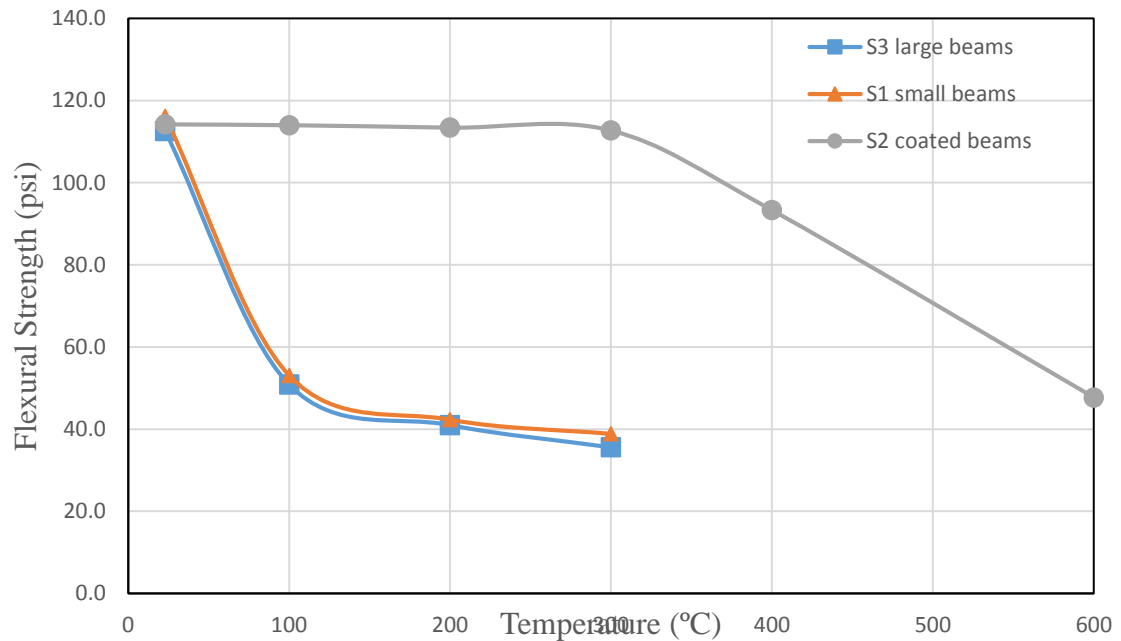


Figure 6. 11 Variation of flexural strength with temperature for series (S1P, S2CP, and S3P)

#### 6.5.4 AAC beams strengthened with basalt tows (Series S4BT)

The AAC beams in series S4BT were identical to those beams in series S3P except they were strengthened with basalt tows to enhance their flexural strength. The area of the tows provided was  $0.0006 \text{ in}^2$ . The provided area is equivalent to a volume fraction of 0.004 % (fiber area/beam cross-section). This provided area of basalt tows increased the flexural strength of the beams by about 33 % compared to the control beams at room temperature as shown in Table 6.6. The three beam specimens in set S4BT-2 were heated to 100 °C compared those in set S4BT-1 which were not heated. The flexural strength of beams S4BT-2 was reduced by about 17 % compared to the unheated beams S4BT-1 as shown in Figure 6.18. The reduction in flexural strength was about 31 % and 40 % when the temperatures were raised to 200 °C and 300 °C respectively as compared with unheated beams. The test results showed that the higher the applied temperature, the higher the

decrease in strength. However, the decrease in flexural strength of the strengthened beams series S4BT-1 was considerably less than the decrease in strength in the plain beams series S3P. For example, the plain beams at 300 °C lost about 68.4 % of their flexural strength whereas the strengthened beams had only lost about 40 % of their flexural strength at 300 °C. Table 6.6 shows that the flexural strength of the strengthened unheated beams S4BT-1 increased by 33 % compared to the unreinforced beam at the same temperature. Above 300 °C, the reinforced beams had about 65 % flexural strength compared to the plain beams at the same temperatures. The heated reinforced beams have sustained higher loads compared to the plain beams in the same the temperature range. The coefficient of variation between the three specimens in sets S4BT-1, S4BT-2, and S4BT-3 was less than 3.5 %, while for set S4BT-4, the variation was about 10 % which could be higher because of specimen fluctuations at higher temperatures. In summary, basalt fibers composites provided substantial enhancement even at low fiber content, and the inorganic matrix maintained the excellent bond between the basalt tows and AAC at elevated temperatures.

In Figure 6.19, the observed behavior of the load-deflection curve of series S4BT was linear up to failure for all temperature with a noticeable constant reduction in stiffness equal to approximately to one third of the total stiffness in all sets of heated series S4BT-2, S4BT-3, and S4BT-4. The reduction in strength with temperature increase is shown in Table 6.6.

Table 6. 5 Comparison between plain and reinforced AAC beams in flexure.

Temperature (°C)	Maximum Load (kips)		Increase in Strength %	Stiffness reductions for S3P (%)	Stiffness reduction for S4BT (%)
	S3P	S4BT			
23	0.582	0.875	33	0	0
100	0.263	0.726	64	33	29
200	0.212	0.604	65	46	33
300	0.184	0.527	65	56	35

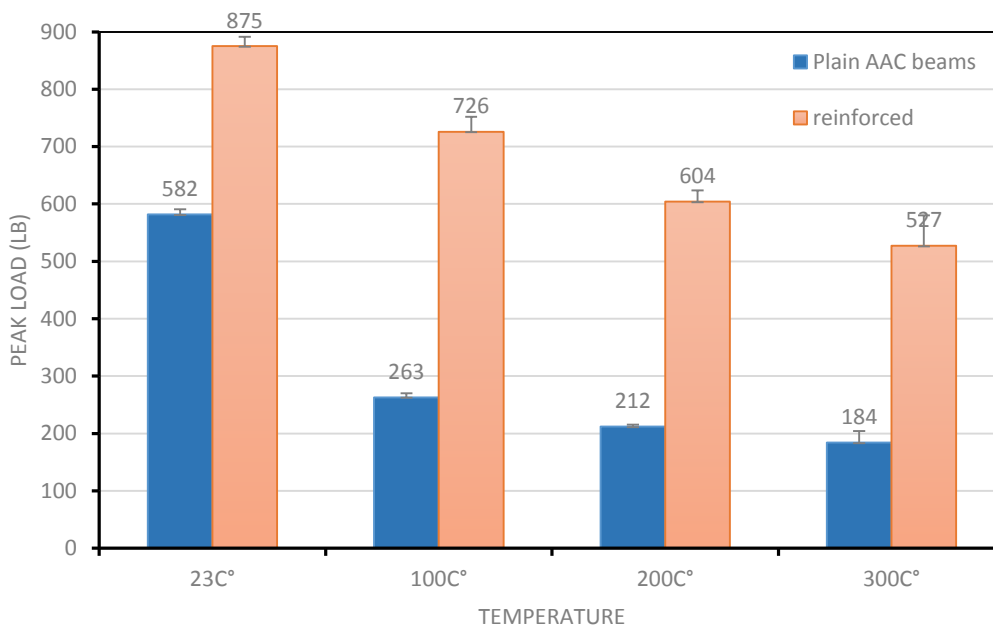


Figure 6. 12 Variation in failure load of plain and basalt reinforced AAC beams in flexure as a function of temperature

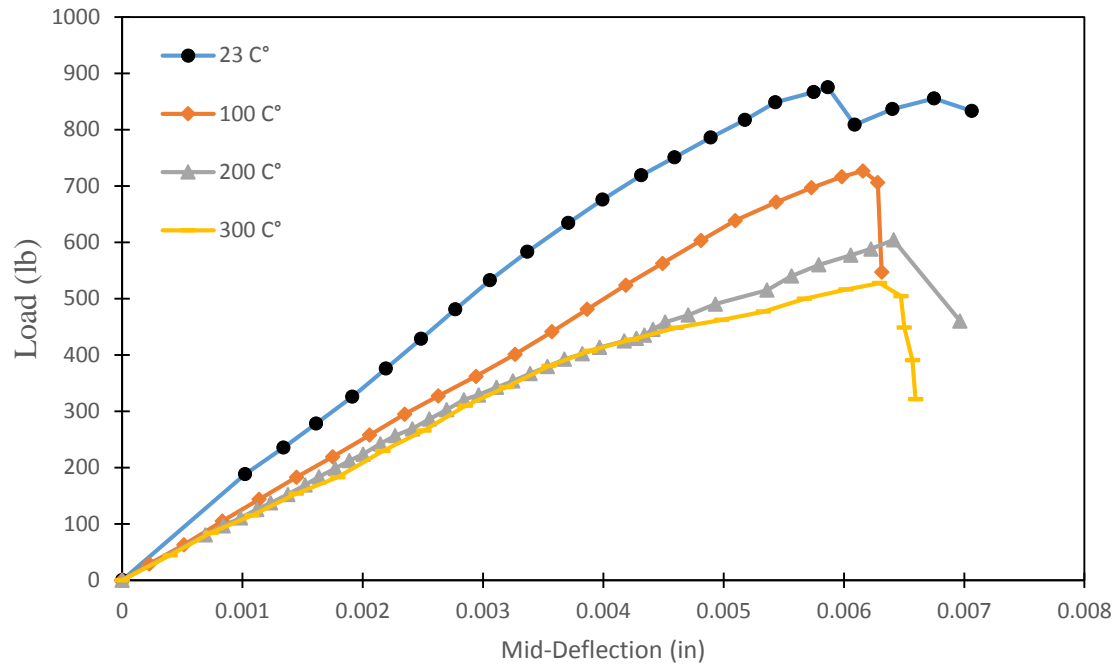


Figure 6. 13 Load versus deflection for reinforced AAC beams as a function of temperature

## 6.6 OBSERVATIONS FROM THERMAL TEST

The following observations from the thermal tests are summarized:

- The compressive strength of AAC slightly increased when the temperature is increased to 100 °C. However, the flexural strength is decreased by 50% for the same temperature increase. Between 100 °C and 400 °C, the compressive strength was approximately increased 10% compared to 13 % drop in flexural strength.
- The decrease in flexure strength of plain AAC with temperature increase was more significant between room temperature and 100 °C compared to the decrease between 100 °C 300 °C.
- The drop in flexural strength of AAC beams reinforced with basalt tows was less than the drop for plain beams. For reinforced beams, the drop between 23 °C and 100 °C was about 17 % compared to 50 % for plain beams.
- The improved performance of basalt-reinforced AAC beams at higher temperatures can be attributed to the good resistance of the inorganic matrix and the basalt tows to high temperatures.
- The effect of coating on the thermal performance on AAC beams was evident. Beams coated with the inorganic matrix had about 20 % drop in flexural strength between 23 °C and 100 °C compared to 50 % in plain uncoated beams, and at 600 °C, the drop in strength was 58 %.
- At 100 °C, the AAC specimens showed random surface cracks with a crack width about 0.004 in. At 400 °C there were more cracks, and the crack width was about 0.1 in.

- The significant drop in flexural strength in beams at high temperatures is due to thermal cracking that reduces the flexural stiffness of the beam. The depth and trajectory of the thermal cracks resulted in the loss of section and reduction of flexural stiffness.
- The enhancement of the AAC beams with basalt composite as exterior skin reinforcement is expected to improve, strength, durability, and resistance to high temperatures thus improving the performance of AAC in various structural applications.

## CHAPTER VII

### 7.1 ANALYTICAL MODELING

The second phase of the research will focus on analytical modeling to predict the capacity of AAC beams reinforced with basalt fabrics and tows in flexure. It will also include the development of design guides for AAC panels strengthened with basalt fabrics subjected to lateral loads. The results from the experimental data of flexural tests will be used to validate the theoretical representations and modeling assumptions and methodologies for determining the capacities of AAC beams in flexure and shear. Several basic concepts of the mechanics of fiber composites and concrete such as elastic analysis, ultimate strength method, and nonlinear analysis using Desayi model will be used to in the analytical investigation for flexural capacity prediction.

### 7.2 FLEXURAL BEHAVIOR OF FRP-REINFORCED AAC BEAMS

The nominal flexural capacity of Autoclaved aerated concrete (AAC) beams strengthened with basalt fabric/tows may be calculated using strain compatibility and forces equilibrium of a cross-section. The following sections present the use of the concept of an equivalent compressive stress block and the test results for the observed nominal flexural capacity in the flexure for AAC beams. Three approaches were suggested to simulate the stress block.

- Linear stress distribution (elastic analysis).
- Rectangular distribution (Whitney's stress block approach).
- Non-linear distribution (Desayi, 1964).

The calculated results from these three methods will be verified and compared with the results reported from the experimental results.

## **7.3 METHOD I - LINEAR STRESS DISTRIBUTION (ELASTIC ANALYSIS)**

### **7.3.1 Assumptions for this approach:**

- The plane section of AAC before bending remains plane after bending. This assumption implies strains across AAC section are linearly varying. This assumption is accurate for the most section of a flexural member except deep beam where shear deformation is considerable.
- AAC beam section behaves elastically when subjected to service load. This assumption implies stress in the AAC beams varies linearly from zero at neutral axis to a maximum at the extreme fiber.
- The tensile strength of AAC is weak, so it was ignored. The basalt FRP assumed to takes all the tension due to flexure.
- The inorganic matrix provides a perfect bond between basalt fabric and AAC beams such that no slip occurs at the interface. This assumption is possible if adequate development length of basalt FRP is provided.

### **7.3.2 Analysis equations for a rectangular section of AAC strengthened with basalt FRP**

Figure 7.1 shows the stress distribution for the AAC beams strengthened with basalt fiber. First, the neutral axis is located in the section. Then, the cracked moment of inertia is

calculated. Finally, the elastic beams formula is applied to determine the stresses in the fiber as shown in the following equations.

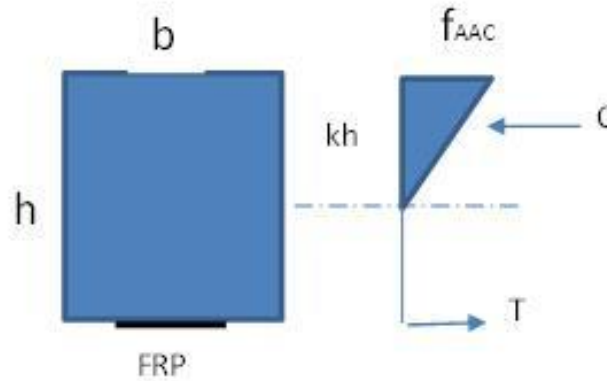


Figure 7. 1 Linear stress distribution approach

The neutral axis location is determined from equilibrium equations as follow:

$$\frac{b(kh)^2}{2} = n \cdot A_{FRP} \cdot (h - kh)$$

$$\frac{b(kh)^2}{2} = n \cdot A_{FRP} \cdot h(1 - k)$$

$$n = \frac{E_{FRP}}{E_{AAC}}$$

$$I_{cr} = \frac{b(kh)^3}{3} + n \cdot A_{FRP} \cdot (h - kh)^2$$

The stress in AAC and FRP are determined using these equations

$$f_{AAC} = \frac{M}{I_{cr}} \cdot kh$$

$$f_{FRP} = \frac{M}{I_{cr}} \cdot (h - kh) \cdot n$$

The test results from Chapter V for strengthened AAC beams were used to verify the results from elastic analysis shown in Table 7.1. Experimental test series S4TN was selected as an example to show the calculation procedure.

Example:

$$f'_{AAC} = 580 \text{ psi} \quad b = 4 \text{ in.} \quad h = 4 \text{ in.}$$

$$A_{FRP} = 0.0008 \text{ in.}^2 \quad (\text{area of 4 tows, each one with } 0.0002 \text{ in.}^2)$$

$$E_{AAC} = 260 \text{ ksi} \quad E_{FRP} = 2600 \text{ ksi} \quad n = 10$$

$$F_{FRP} = 266 \text{ Ksi (from the coupon test)}$$

$$\frac{b(kh)^2}{2} = n \cdot A_{FRP} \cdot (h - kh)$$

$$\frac{4 * (kh)^2}{2} = 10 * 0.0008(4 - kh)$$

$$Kh = 0.12 \text{ in.}$$

Second, the cracked moment of inertia calculated

$$I_{cr} = \frac{b(kh)^3}{3} + n \cdot A_{FRP}(h - kh)^2$$

$$I_{cr} = \frac{4(0.12)^3}{3} + 10 * 0.0008(4 - 0.12)^2$$

$$I_{cr} = 0.13 \text{ in.}^4$$

Finally, the moment capacity in the section is calculated

$$f_{FRP} = \frac{M}{I_{cr}} \cdot (h - kh) \cdot n$$

$$266 = \frac{M}{0.13} \cdot (4 - 0.12) \cdot 10$$

$$M = 842 \text{ in.lb}$$

$$M = 2P$$

The predicted maximum load from elastic analysis for series S4TN is 421 lbs

Table 7.1 shows the maximum loads from test data (presented in Chapter V) and those predicted from elastic analysis for different series of the AAC beams in flexure. The series shown in Table 7.1 include AAC beams strengthened with basalt tows and AAC beams strengthened with basalt fabrics. The series shown in Table 7.1 are those series that failed in flexure. The series with other types of failure were excluded because the maximum stress in the fiber can not be predicted. In general, Table 7.1 shows good compatibility between the analytical results and the experimental results in most tested series except the series with an extra amount of basalt fibers (Series S50FS3, S90FS3, and S90FS2). For the AAC beams strengthened with basalt tows, the average difference in the maximum load between the experimental and the analytical was about 3.3%. For the AAC beams strengthened with basalt fabrics, the average difference in the maximum load between the experimental and the analytical was about 8.9%. The contrast in averages between the two strengthening schemes may be attributed to the amount of the basalt fibers used in each strengthening scheme. Because less basalt fibers need to be impregnated when the tows are used, it is believed that better bond will exist between the tows and the soffit of the AAC beam. As a result, the possibility of having unequal loads in the filaments of the fiber is

less, leading to better performance and higher strength. The predicted maximum load from the elastic analysis for Series S4TN – in which the AAC beams were strengthened with tows- was very close to the maximum load from test results (about 0.3% difference). For Series S10TS the difference between maximum loads was about 3.5 % which is still considered to be a small difference. For Series S5TN the difference between maximum loads was about 6.3% which is still a relatively small difference. It is worth noting that the flexural capacity in this series was increased by approximately 3.7 times the plain series discussed in Chapter V.

For the fabric strengthening scheme, the difference between maximum loads predicted from elastic analysis and those from experimental data for Series S13FN, S50FS, S50FS2 was 3.1 %, 0.3 %, and 2.1% respectively. For Series S90FS2, S50FS3, and S90FS3, the difference was 16.2 %, 13.7 %, and 18.4 % respectively. The biggest difference between the predicted load and the test load was 18.4% which was observed for Series S90FS3. As discussed earlier the reason for this relatively big difference compared to other series, may be attributed to the increase in the fiber amount per section.

Table 7. 1 Comparison of maximum loads from test data and from elastic analysis for different series of the AAC beams in flexure.

Categories	Group ID	Ultimate load (lb) from test	Elastic analysis				
			AFRP(in <sup>2</sup> )	Kh(in)	I <sub>cr</sub> (in <sup>4</sup> )	analytical load from FFRP(lb)	% difference in P
Tows strengthening	S4TN	423	0.0008	0.12	0.130774	421	-0.3
	S5TN	495	0.0010	0.14	0.162661	526	6.3
	S10TS	1012	0.0020	0.20	0.319076	1047	3.5
Fabric strengthening	S13FN	418	0.0010	0.17	0.369149	431	3.1
	S90FS <sub>2</sub>	1776	0.0070	0.36	1.054542	2064	16.2
	S50FS	1191	0.0040	0.27	0.62095	1188	-0.3
	S50FS <sub>2</sub>	1214	0.0040	0.27	0.62095	1188	-2.1
	S50FS <sub>3</sub>	1574	0.0040	0.34	1.421248	1790	13.7
	S90FS <sub>3</sub>	2630	0.0070	0.44	2.426826	3114	18.4

## **7.4 METHOD II - RECTANGULAR STRESS DISTRIBUTION (WHITNEY'S STRESS BLOCK APPROACH)**

The analysis recommendations in this method are based on a synthesis of analytical recommendations from the previous research and from the publication of the ACI526 committee. The proposed analysis procedure for strengthening AAC beams with the basalt fiber is based on the same principles used for strength analysis of conventional reinforced concrete elements except for the stress-strain parameters of AAC need to be defined in order to apply strength analysis. In this method, strain compatibility between AAC and basalt fiber (with some modifications as noted) is assumed, and equilibrium of forces on the composite section is used to obtain the plastic neutral axis and the resulting moment capacity.

Nominal flexural capacity ( $M_n$ ) can be calculated using conventional assumptions of plane sections, strain compatibility, stress-strain relationships, and equilibrium. The compressive zone was determined based on a linear stress-strain relationship, using a maximum useful compressive strain in the AAC of 0.003, and an equivalent rectangular stress block with a height of  $0.85f'_{AAC}$ , and depth of  $1\chi$ , where  $\beta_1 = 0.67$  (ACI 526).

Using these relationships, Argudo (2003) reported very good agreement between experimentally derived and analytically determined nominal moment capacities ( $M_n$ ) for reinforced AAC panels failing predominantly in flexure (Panels 1-2 YF 6-24-12.5 A and 1-2 YF 8-24-16.5 A).

### 7.4.1 Assumptions for this Method II

The proposed assumptions for strengthened AAC beams are based on the same principles used for strength design of conventional reinforced concrete elements:

- Strain distribution across the section is assumed to be linear.
- Plan section before bending remains plain after bending.
- The tensile strength of AAC may be neglected.
- At ultimate strength, the maximum strain at the extreme compression fiber of AAC is assumed to equal to 0.003, as ACI 318, ACI 526

Figure 7.2 shows the strain and stress distribution of the cross section.

### 7.4.2 Analysis equations for a rectangular section of AAC strengthened with basalt

#### FRP

The compression force in the AAC and the tension force in the basalt fibers are denoted by C and T respectively and are calculated as follows:

$$C = 0.85f'_{AAC} \cdot a \cdot b$$

$$T = A_{FRP} \cdot f_{FRP}$$

The depth of the AAC compression block  $a$  is obtained from force equilibrium by equating T and C and is given by:

$$a = \frac{A_{FRP} \cdot f_{FRP}}{0.85f'_{AAC} \cdot b}$$

The moment capacity of the cross section is obtained by summing the moments of the section forces at any point and is given by:

$$M_n = A_{FRP} \cdot f_{FRP} \cdot \left(h - \frac{a}{2}\right)$$

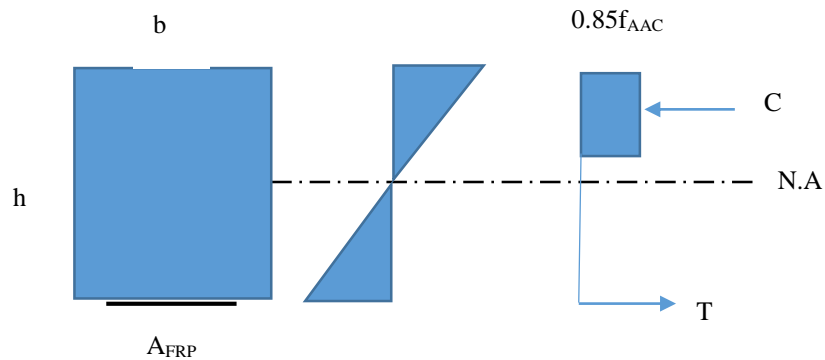


Figure 7. 2. Whitney's block for rectangular distribution

Using Method II to predict the moment capacity of AAC Series S4TN predicts a failure load of 421 lbs. The cross section of Series S4TN was 4 in x 4 in, and the compressive strength and elastic modulus of AAC was 580 psi and 260 ksi respectively. The modulus and tensile strength of the basalt fibers were 2600 ksi and 266 ksi respectively.

Table 7.2 shows a comparison of maximum loads from test data and strength analysis for different series of the AAC beams in flexure.

As observed in Table 7.2, the strength method (Method II) showed better agreement with the analytical results than the linear elastic method (Method I). The average differences between the maximum load from Method II and those obtained from the experimental results for the AAC beams strengthened with the tows were about 2.6%. Table 7.2 shows series S4TN has an excellent match between the maximum load predicted by the strength analysis and the maximum load predicted by laboratory testing. On the other hand, S5TN showed the highest difference in maximum loads between prediction and tests (about 5.7

%). For the AAC beams strengthened with basalt fabrics, the average differences in the maximum load from strength analysis and laboratory tests was about 7 %. This difference was smaller than the 8.9 % difference observed when using the linear elastic method to predict maximum loads. The best match for the maximum loads from strength analysis and lab tests was observed for S13FN (about 2.6%). The differences for series S90FS2, S50FS3, and S90FS3 were 5.7 %, 10.7 %, and 11.8 % respectively. The differences in maximum load prediction from the linear elastic method for the same series were 16.2 %, 13.7 %, and 18.4 % respectively.

The only two series that did not follow the trend of maximum load predictions between the strength method and the linear elastic method were series S50FS and S50FS2. For those two series, the difference in maximum load from analytical prediction and lab tests was higher using the strength method (Method II) compared to the elastic method (Method I). In the linear method, the differences in these two series were 0.3 % and 2.1 % respectively, while in the ultimate method, they were 4.8 % and 6.6 % respectively.

Table 7. 2. Comparison of maximum loads from test data and the strength analysis (Method II ) for different series of the AAC beams in flexure

Categories	Group ID	Ultimate load (kN) from the test	Ultimate analysis				
			a(in )	Tension force T(lb)	nominal capacity Mn(k.in)	Analytical load P(lb)	% different in P
Tows strengthenin g	S4TN	423	0.11	213	0.839718	420	-0.7
	S5TN	495	0.13	266	1.04606	523	5.7
	S10TS	1012	0.27	532	2.056239	1028	1.6
Fabric strengthenin g	S13FN	418	0.13	266	0.857769	429	2.6
	S90FS <sub>2</sub>	1776	0.94	1862	6.568932	1877	5.7
	S50FS	1191	0.54	1064	3.968957	1134	-4.8
	S50FS <sub>2</sub>	1214	0.54	1064	3.968957	1134	-6.6
	S50FS <sub>3</sub>	1574	0.54	1064	6.096957	1742	10.7
	S90FS <sub>3</sub>	2630	0.94	1862	10.29293	2941	11.8

### 7.5 NON-LINEAR DISTRIBUTION ANALYSIS – METHOD III

The nonlinear behavior of AAC beams will be discussed in this approach. The nonlinear behavior of AAC beams will be modeled after the empirical formula proposed by Desayi which assumes the stress-strain relation of AAC can be represented by the following equation (Eq. 1):

$$f = \frac{E_{\varepsilon}}{1 + \left(\frac{\varepsilon}{\varepsilon_0}\right)^2} \quad (1)$$

Where:

f: stress at any strain  $\varepsilon$

$\varepsilon_0$ : strain at the maximum stress of  $f_0$

$E_{\varepsilon}$ : a constant (same as initial tangent modulus) such that  $E_{\varepsilon} = \frac{2f_0}{\varepsilon_0}$

The area between the curve and the strain axis in Figure 7.3 is calculated as follows:

$$\begin{aligned} \int_0^{\varepsilon_c} f \, d\varepsilon &= \int_0^{\varepsilon_c} \frac{E_{\varepsilon}}{1 + \left(\frac{\varepsilon}{\varepsilon_0}\right)^2} d\varepsilon \\ &= \frac{1}{2} E_{\varepsilon} \cdot \varepsilon_0^2 \cdot \log_e \left(1 + \frac{\varepsilon_c^2}{\varepsilon_0^2}\right) \end{aligned} \quad (2)$$

$$= f_0 \cdot \varepsilon_0 \cdot \log_e \left(1 + \frac{\varepsilon_c^2}{\varepsilon_0^2}\right) \quad (3)$$

The moment of this area about the stress axis is given by:

$$\int_0^{\varepsilon_c} f \varepsilon d\varepsilon = \int_0^{\varepsilon_c} \frac{E \varepsilon^2}{1 + \left(\frac{\varepsilon}{\varepsilon_0}\right)^2} d\varepsilon$$

$$= E \cdot \varepsilon_0^2 \left( \varepsilon_c - \varepsilon_0 \tan^{-1} \frac{\varepsilon_c}{\varepsilon_0} \right) \quad (4)$$

For known values of  $\varepsilon_c$ ,  $f_0$ , and  $\varepsilon_0$  the total area and the moment of the area can be easily computed from Eq. (2), (3) and (4). Generally  $\varepsilon_c$  is unknown, but  $kf_0$  is assumed and thus  $\varepsilon_c$  is determinable from Eq. (1).

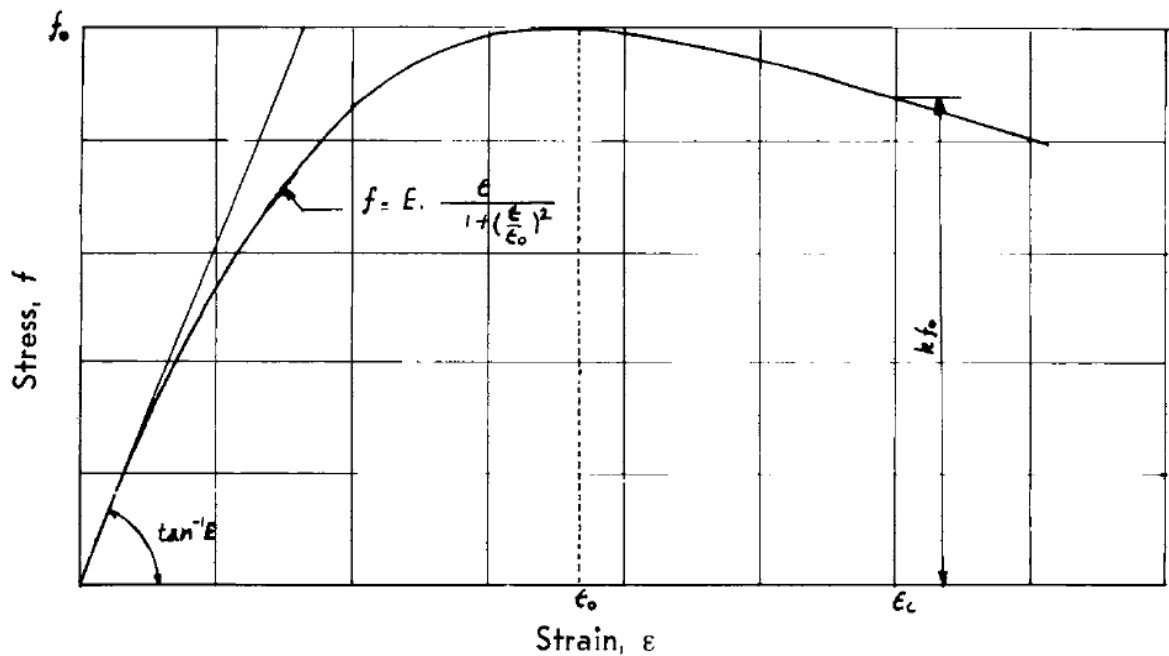


Figure 7.3. Stress-strain curve of AAC used in the nonlinear analysis (Desayi 1964)

The non-linear analysis method which uses the nonlinear stress-strain model of AAC proposed by Desayi requires several iterations to be performed in order to obtain equilibrium and moment capacity. To perform the non-linear analysis, a spreadsheet was developed to carry out the necessary computations. The results of the non-linear analysis are shown in Table 7.3.

The procedure followed to develop the spreadsheet is summarized in the following steps:

Step 1: Assume the neutral axis of the section ( $kh$ )

Step 2: Find  $\varepsilon_0 = \frac{1.71f'_{AAC}}{E_{AAC}}$ , knowing that  $E_{AAC} = 6500(f'_{AAC})^{0.6}$

1. Find the compressive strain of the AAC material using the strain compatibility

$$\text{equation } \varepsilon_{AAC} = \varepsilon_{FRP} \cdot \frac{kd}{h-kd}$$

2. Calculate  $\beta_2 = \frac{\ln(1 + (\frac{\varepsilon_{AAC}}{\varepsilon_0})^2)}{\varepsilon_{AAC}/\varepsilon_0}$

3. Calculate the compressive force using the following equation

$$C = 0.9f'_{AAC} \cdot \beta_2 \cdot kh \cdot b$$

4. Calculate the tension force from  $T = \varepsilon_{FRP} \cdot A_{FRP}$

5. Compare C to T, both C and T should be equal or have a closer value to each other.

If the difference between them is acceptable, then proceed to find the moment capacity of the section, otherwise adjust the value of the  $kh$  and repeat the steps from 1 to 7.

6. If C and T are close enough, then find  $K_2 = 1 - \frac{2(\frac{\varepsilon_{AAC}}{\varepsilon_0} - \tan^{-1}(\frac{\varepsilon_{AAC}}{\varepsilon_0}))}{\beta_2 \cdot (\frac{\varepsilon_{AAC}}{\varepsilon_0})^2}$

7. Calculate the moment capacity of the section  $M = T \cdot (d - K_2 kh)$
8. Find the predicted analytical load  $M=2P$

The results of the nonlinear analysis shown in Table 7.3 show the maximum predicted load and the difference in maximum load from the non-linear analysis (Method III) and experimental results for each test series. For AAC beams strengthened with the basalt tows, the average difference in maximum load from nonlinear analysis and lab tests was 2.6 %. This difference was similar to the difference observed when using the strength analysis (Method II). Even though the average difference in maximum load from the nonlinear analysis of those beams was same as the average difference from the strength analysis, the average difference of individual series was not similar. For example, in series S4TN, the difference in maximum load from non-linear analysis and lab tests was about 3.5 % while the difference using the strength analysis was only 0.7 % and was 0.3% using the linear elastic analysis. That showed the analytical results of this series (S4TN) had a noticeable shift from the experimental result with the nonlinear analysis. The nonlinear analytical result for series S5TN showed a better match with the experimental results than the other two methods of analysis. In the nonlinear analysis, the difference in maximum load for series S5TN was 2.9 % compared to 5.7% from the strength analysis. The difference in maximum load was 3.5% from the linear elastic method. For series S10Ts which was strengthened using basalt tows, the difference in maximum load between the nonlinear method and lab tests was about 1.5%. Using the strength analysis and the linear elastic analysis, the difference in maximum loads between analytical prediction and lab tests was 1.6 % and 3.5% respectively.

For the AAC strengthened with basalt fabrics, the average differences using nonlinear analysis of these beams was 6.3 %. When the same beams were analyzed using the strength method, the difference in maximum load between analytical prediction and lab tests was about 7% and was about 8.9% when analyzed using the elastic method. Series S13FN, had a compatible very good match using the nonlinear analysis to predict maximum load and it was the series that had the best match among all the series in this group of beams. The difference in maximum load between the non-linear analysis and experimental results for the series (S13FN) was about 0.3 % only, while in the strength analysis was about 2.6 %, and in the linear analysis was about 3.1 %. Series S50FS2 had less match with the experimental results when using the nonlinear analysis. The difference in this series (S50FS2) was about 9.9 %, while from the strength analysis, it was about 6.6 % and the best match was from the linear analysis with 2.1 % difference only.

In general, the results obtained from the nonlinear analysis were closer to the results obtained from the strength analysis and had and slightly different from the results obtained from the linear elastic analysis as shown in Table 7.4.

In general, the maximum load predicted using the nonlinear analysis did not have good agreement with the maximum loads from the laboratory tests. The reason may attribute to the behavior of the stress-strain curve of the AAC material compared to the behavior of the stress-strain curve of the conventional concrete. The Desayi model was built based on the behavior of the conventional concrete as shown in Figure 7.4; however; the behavior of the AAC material had slight differences. In two previous studies (Tanner 2003, and Cancino 2003), a comprehensive study of the behavior of the stress-strain curve of the AAC material have been conducted as shown in Figures 7.5, 7.6, and 7.7. Comparing the behavior of the

stress-strain curves for both materials, the ascending portion of the two curves was pretty close except that the AAC material tends to have a more linear ascending curve. The maximum strain of the concrete was about 0.002 as shown in Figure 7.4, while in the AAC material was ranging between 0.002 to 0.003 as shown in the Figures 7.5, 7.6, and 7.7. The descending portion of the two stress-strain curves showed a noticeable difference in behavior. The concrete stress-strain curve had a smooth descending; however; in some of the AAC stress-strain curves the descending portion of the curve was not existent. These differences in the behavior of the two material may explain the reason for the difference in the results between analytical and experimental results using the nonlinear analysis (Method III).

Table 7.3. Comparison of maximum loads from test data and from non-linear analysis (Method III) for different series of the AAC beams in flexure

Categories	Group ID	Ultimate load (lb) from test	Non-linear analysis		
			Kh(in)	analytical load P(lb)	% different in P
Tows strengthening	S4TN	423	0.228	408	-3.5
	S5TN	495	0.258	509	2.9
	S10TS	1012	0.391	1027	1.5
Fabric strengthening	S13FN	418	0.258	417	-0.3
	S90FS2	1776	1.22	1938	9.1
	S50FS	1191	0.88	1094	-8.2
	S50FS2	1214	0.88	1094	-9.9
	S50FS3	1574	1.05	1617	2.7
	S90FS3	2630	1.42	2842	8.0

Table 7. 4. Difference in maximum load from analytical prediction and lab tests for the the three analytical methods

Strengthening Schemes	Differences in the three Method of Analysis		
	Linear Elastic (Method I) (%)	Strength Analysis (Method II) (%)	Nonlinear (Method III) (%)
Basalt Tows	3.3	2.6	2.6
Basalt Fabric	8.9	7.0	6.3

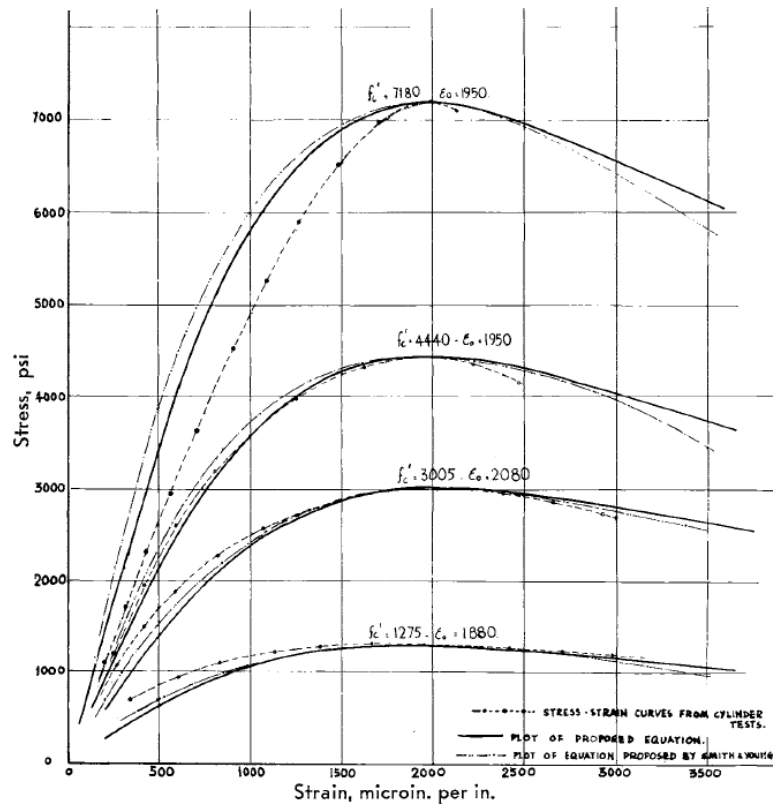


Figure 7.4. stress strain curves for normal concrete

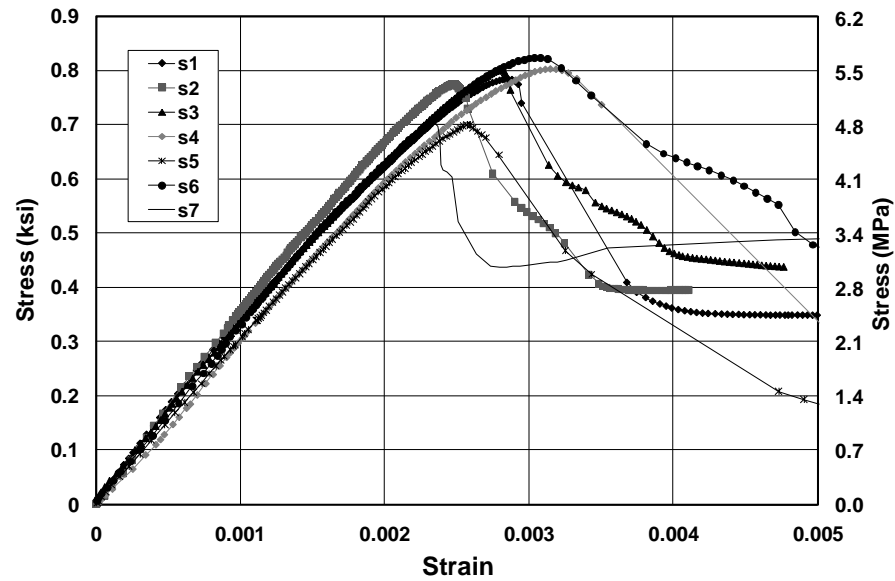


Figure 7.5. Compressive stress versus strain for Shipment 1 (Tanner 2003).

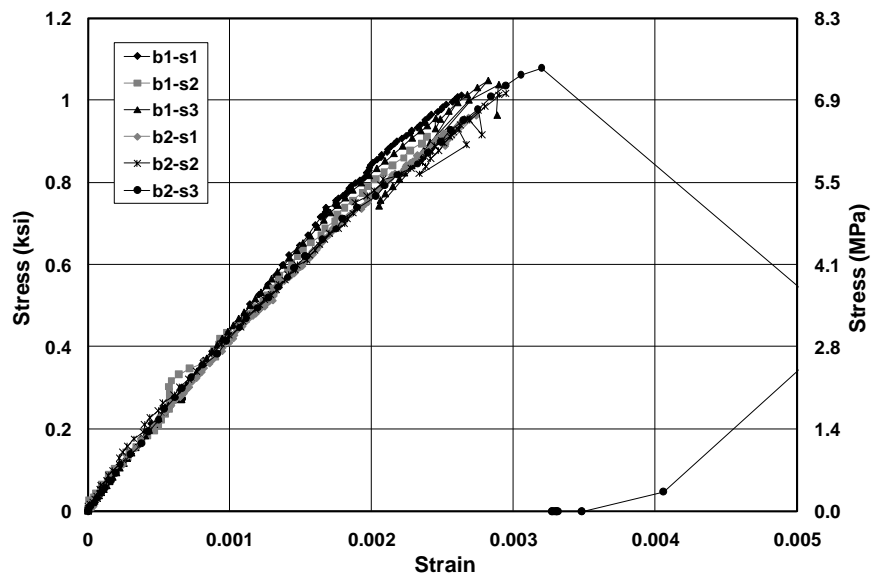


Figure 7. 6. Compressive stress versus strain for Contec Shipment 2 (Tanner 2003).

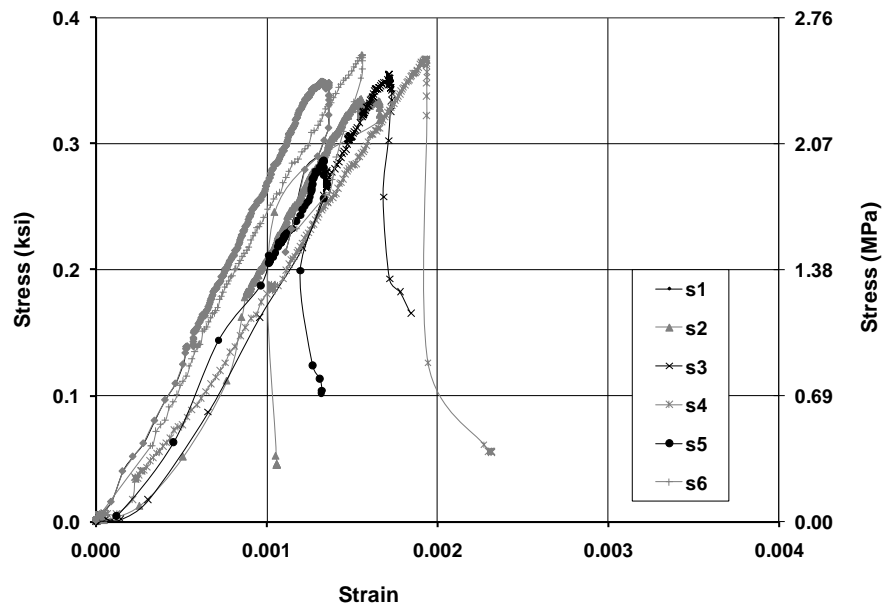


Figure 7.7. Compressive stress versus strain for Babb Shipment 3 (Cancino 2003).

## CHAPTER VIII

### CONCLUSIONS AND RECOMMENDATIONS

#### 8.1 CONCLUSIONS

This dissertation evaluates the performance of strengthened Autoclaved Aerated Concrete (AAC) members as structural elements. The AAC beams were strengthened with basalt fibers and an inorganic matrix. The inorganic matrix was chosen to provide the required adhesion between the AAC and the basalt fibers in order to provide fire protection for the strengthened system. Based on the experimental and the analytical results the following conclusions can be drawn:

- The inorganic matrix provided the necessary bond strength between AAC and basalt fibers needed to achieve rupture failure of the fibers.
- There is a substantial increase in the maximum load and the ductility of AAC beams strengthened with basalt fabrics and basalt tows in the tension zone.
- The flexural capacities of the AAC beams can be doubled using a limited amount of fibers.
- The matrix was easy to work with, and its composition was conducive for uniform wetting of the fabrics and the tows.
- The hand layout impregnation was a successful technique to apply the inorganic matrix, and it simulated the field application.

- Basalt fabrics and tows can be a viable alternative to reinforce AAC lintels and beams in flexure compared to steel wire mesh which tends to corrode and also adds weight to the structure.
- The results of this study showed that the flexural strength of plain AAC beams decreases significantly with the increase in temperature. When these beams are strengthened with basalt tows, the loss of flexural strength is less pronounced compared to plain AAC beams. After exposed to 300 °C, the strength decreased for plain AAC beams was 68 % as compared to 40 % for strengthening AAC beams.
- The compressive strength of AAC slightly increased when the temperature is raised to 100 °C. However, the flexural strength is decreased by 50% for the same temperature increase.
- Between 100 °C and 400 °C, the compressive strength was approximately increased by 10% compared to 13 % drop in flexural strength.
- The decrease in flexure strength of plain AAC with increasing temperature was more significant between the room temperature and 100 °C compared to the decrease in flexure strength between 100 °C and 300 °C.
- The drop in flexural strength of AAC beams reinforced with basalt tows was less than the drop for plain beams. For reinforced beams, the drop between 23 °C and 100 °C was about 17 % compared to 50 % for plain beams.

- The improved performance of basalt-reinforced AAC beams at higher temperatures can be attributed to the good resistance of the inorganic matrix and the basalt tows to high temperatures.
- The effect of coating on the thermal performance on AAC beams was evident. Beams coated with the inorganic matrix had about 20 % drop in flexural strength between 23 °C and 100 °C compared to 50 % in plain uncoated beams. At 600 °C, the drop in strength was 58 %.
- The significant drop in flexural strength in beams at high temperatures is due to thermal cracking that reduces the flexural stiffness of the beam. The depth and trajectory of the thermal cracks resulted in the loss of section and reduction of flexural stiffness.
- The inorganic matrix used to impregnate the basalt fiber did not emit any odors or smoke even at an elevated temperature up to 1000 °C
- The enhancement of the AAC beams with basalt composite as exterior skin reinforcement is expected to improve, strength, durability, and resistance to high temperatures thus improving the performance of AAC in various structural applications.
- Results from the analytical investigation show that the difference in the failure load predicted by the rectangular stress distribution method and the non-linear stress distribution method was not significant.

## **8.2 RECOMMENDATIONS:**

This dissertation focused on evaluating the mechanical properties of the AAC beams strengthened using FRP. Further research is still needed in the following areas:

- Further tests need to be performed for the other types of Autoclaved Aerated Concrete types ( AAC5 and AAC6) with different densities in order to verify the results obtained in this experiment.
- Perform more experiments with different beam dimension and different span to the depth ration to evaluate size effects.
- The use of basalt fabrics and tows for shear strengthening of AAC beams.
- The suggested strengthening system should be tested for impact load and evaluate the damage due to this load.

## **REFERENCES**

ACI Committee, American Concrete Institute, & International Organization for Standardization. (2014). Building code requirements for structural concrete (ACI 318-14) and commentary. American Concrete Institute.

ACI Committee, American Concrete Institute, & International Organization for Standardization. (2009). Guide for Design and Construction with Autoclaved Aerated Concrete (AAC) panels (ACI 523.4R-09) and commentary. American Concrete Institute.

American Society for Testing and Materials. C78/C78M-15b (2015). Standard Test Method for Flexural Strength of Concrete (Using Simple Beam with Third-Point Loading). West Conshohocken, PA, USA: American Society for Testing and Materials.

American Society for Testing Materials. C39/C39M-15a. (2015). Standard Test Method for Compressive Strength of Cylindrical Concrete Specimens. Philadelphia, PA, USA: American Society for Testing and Materials.

Arafa, M. D. I. (2007). High strength-high temperature laminated sandwich beams. ProQuest.

Argudo, J. F., Fern, J., & Argudo, O. (2003). Evaluation and Synthesis of Experimental Data for Autoclaved Aerated Concrete.

Aroni, I. S. (1993). Autoclaved aerated concrete-properties, testing, and design. CRC Press.

ASTM C192/C192M. (2015). Standard Practice for Making and Curing Concrete Test Specimens in the Laboratory.

Babu, K., & Palani, S. (2013). Mechanical and abrasive wear behavior of glass and basalt fabric-reinforced epoxy composites. *Journal of Applied Polymer Science*, 130(1), 120-130.

Bakis, C. E., Ganjehlou, A., Kachlakev, D. I., Schupack, M., Balaguru, P. N., Gee, D. J., ... & Kliger, H. S. (2002). Guide for the design and construction of externally bonded FRP systems for strengthening concrete structures. Reported by ACI Committee, 440(2002).

Balkema, A. A. (1992). Advances in autoclaved aerated concrete. F. H. Wittmann (Ed.). AA Balkema.

Boutros, M., & Saverimutto, L. (1997). Anchorage capacity of reinforcing bars in autoclaved aerated concrete lintels. *Materials and Structures*, 30(9), 552-555.

Chen, J. F., & Teng, J. G. (2003). Shear capacity of fiber-reinforced polymer-strengthened reinforced concrete beams: Fiber reinforced polymer rupture. *Journal of Structural Engineering*, 129(5), 615-625.

Chusid, M. (1999). Building with autoclaved aerated concrete. *Masonry Construction*, January, 24-27.

Concrete-Properties, A. A., & Design, S. (2005). SP-226, S. Caijun, FH Fouad, eds., American Concrete Institute, Farmington Hills, MI.

Czigány, T., Vad, J., & Pölöskei, K. (2005). Basalt fiber as a reinforcement of polymer composites. *Periodica Polytechnica Mechanical Engineering*, 49(1), 3-14.

Davidovits, J. (2002, October). 30 years of successes and failures in geopolymer applications. Market trends and potential breakthroughs. In *Keynote Conference on Geopolymer Conference*.

Davidovits, J., & Cordi, S. A. (1979). Synthesis of new high temperature geo-polymers for reinforced plastics/composites. *SPE PACTEC*, 79, 151-154.

Dembowski, J. (2001). A study of the material properties and structural behavior of plain and reinforced AAC components.

Desayi, P., & Krishnan, S. (1964). Equation for the stress-strain curve of concrete. *Journal of the American Concrete Institute*, 61(3), 345-350.

Domingo, E. R. (2008). An Introduction to Autoclaved Aerated Concrete including design requirements using strength design (Doctoral dissertation, Kansas State University).

Drysdale, R. G., Hamid, A. A., & Baker, L. R. (1994). *Masonry structures: behavior and design*. Prentice Hall.

Foden, A. J. (1999). Mechanical properties and material characterization of polysialate structural composites.

Fouad, F. H., & Dembowski, J. (2005). Mechanical Properties of Plain AAC Material. *Special Publication*, 226, 1-16.

Garon R.J. (2001). The effectiveness of High Strength Composites as Structural & Protective Coatings for Structural Elements.

Giancaspro, J. W. (2004). Influence of reinforcement type on the mechanical behavior and fire response of hybrid composites and sandwich structures.

Giancaspro, J. W., Papakonstantinou, C. G., & Balaguru, P. N. (2010). The flexural response of inorganic hybrid composites with E-glass and carbon fibers. *Journal of Engineering Materials and Technology*, 132(2), 021005.

Gottfredsen, F. R., Knutsson, H. H., & Nielsen, A. (1997). Determination of length changes due to moisture variations in autoclaved aerated concrete. *Materials and Structures*, 30(3), 148-153.

Grace, N. F., Sayed, G. A., Soliman, A. K., & Saleh, K. R. (1999). Strengthening reinforced concrete beams using fiber reinforced polymer (FRP) laminates. *ACI Structural Journal*, 96(5).

Hammell, J. A. (2000). The influence of matrix composition and reinforcement type on the properties of polysialate composites.

High, C., Seliem, H. M., El-Safty, A., & Rizkalla, S. H. (2015). Use of basalt fibers for concrete structures. *Construction and Building Materials*, 96, 37-46.

Hollaway, L. C., & Leeming, M. (Eds.). (1999). *Strengthening of reinforced concrete structures: Using externally-bonded FRP composites in structural and civil engineering*. Elsevier.

Keyvani, A. THERMAL PERFORMANCE & FIRE RESISTANCE OF AUTOCLAVED AERATED CONCRETE EXPOSED HUMIDITY CONDITIONS.

Kizilkanat, A. B., Kabay, N., Akyüncü, V., Chowdhury, S., & Akça, A. H. (2015). Mechanical properties and fracture behavior of basalt and glass fiber reinforced concrete: An experimental study. *Construction and Building Materials*, 100, 218-224.

Klein, M. J. (2013). *Nondestructive repair and rehabilitation of structural elements using high strength inorganic polymer composites* (Doctoral dissertation, Rutgers University-Graduate School-New Brunswick).

Klingner, R. E., Tanner, J. E., & Varela, J. L. (2005). *Technical Justification for Proposed Design Provisions for AAC Structures: Assemblage Test and Development of R and CD Factors*. ACI Special Publication, 226.

Kurtz, S., & Balaguru, P. (2001). Comparison of inorganic and organic matrices for the strengthening of RC beams with carbon sheets. *Journal of Structural Engineering*, 127(1), 35-42.

Li, W., & Xu, J. (2009). Mechanical properties of basalt fiber reinforced geopolymeric concrete under impact loading. *Materials Science and Engineering: A*, 505(1), 178-186.

- Lu, Z., Xian, G., & Li, H. (2015). Experimental Study on the Mechanical Properties of Basalt Fibres and Pultruded BFRP Plates at Elevated Temperatures. *Polymers & Polymer Composites*, 23(5), 277.
- Lyon, R. E., Balaguru, P. N., Foden, A., Sorathia, U., Davidovits, J., & Davidovics, M. (1997). Fire-resistant aluminosilicate composites. *Fire and materials*, 21(2), 67-73.
- Mallick P.K., (1993). *Fiber-Reinforced Composites: Materials, Manufacturing, and Design*. Marcel Dekker, Inc., New York, pp. 566.
- Mazumdar, S. (2001). *Composites manufacturing: materials, product, and process engineering*. CrC press.
- Mei, P., Yanjun, L., Ye, Z., & Yu, C. (2013). Mechanical Properties of Autoclaved Aerated Concrete with Different Densities. *Advances in Civil Engineering Materials*, 2(1), 441-456.
- Memari, A. M., Lepage, A., & Setthachayanon, J. (2010). An experimental study of autoclaved aerated concrete lintels strengthened with externally bonded glass FRP. *Journal of Reinforced Plastics and Composites*, 29(22), 3322-3337.
- Mousa, M. A., & Uddin, N. (2009). Experimental and analytical study of carbon fiber-reinforced polymer (FRP)/autoclaved aerated concrete (AAC) sandwich panels. *Engineering Structures*, 31(10), 2337-2344.
- Narayanan, N., & Ramamurthy, K. (2000). Structure and properties of aerated concrete: a review. *Cement and Concrete Composites*, 22(5), 321-329.
- Nazier, M. (2004). Evaluation of high strength composites and new construction techniques for their effective use.
- Oskouei, A. V., & Rasouli, S. The Study of FRP Sheet Effectiveness on Structural Behavioral of AAC Blocks.
- Parker, C. K., Tanner, J. E., & Varela, J. L. (2007). Evaluation of ASTM methods to determine splitting tensile strength in concrete, masonry, and autoclaved aerated concrete. *Journal of ASTM International*, 4(2).
- Parnas, R., Shaw, M. T., & Liu, Q. (2007). Basalt fiber reinforced polymer composites (No. NETCR63).
- Pavlovski, D., Mislavsky, B., & Antonov, A. (2007). CNG cylinder manufacturers test basalt fiber. *Reinforced Plastics*, 51(4), 36-39.

Pytlik, E. C., & Saxena, J. (1992). Autoclaved cellular concrete: the building material for the 21st Century. In Proceedings of the 3rd Rilem International Symposium on Autoclaved Aerated Concrete (Zürich).

Ramakrishnan, V., Tolmare, N. S., & Brik, V. B. (1998). Performance evaluation of 3-D basalt fiber reinforced concrete & basalt rod reinforced concrete (No. NCHRP-IDEA Project 45).

Rivera, J. L. V. (2003). Development of R and CD Factors for the Seismic Design of AAC Structures (Doctoral dissertation, Ph.D. Thesis. The University of Texas at Austin, USA).

Shi, C., & Fouad, H. F. 2005. Autoclaved Aerated Concrete-Properties and Structural Design, SP-226, American Concrete Institute, Farmington Hills, MI.

Sim, J., & Park, C. (2005). Characteristics of basalt fiber as a strengthening material for concrete structures. *Composites Part B: Engineering*, 36(6), 504-512.

Snow, C. A. (1999). A comprehensive study of the material properties and structural behavior of AAC products.

Standard, A. S. T. M. C1660-10 (2010) Standard Specification for Thin-bed Mortar for Autoclaved Aerated Concrete (AAC) Masonry. ASTM International.

Standard, A. S. T. M. C1693-11 (2011) Standard Specification for Autoclaved Aerated Concrete (AAC). ASTM International.

Standard, A. S. T. M. C1694-09 (2009) Standard Specification for Reinforced Autoclaved Aerated Concrete (AAC) Elements. ASTM International.

Standard, A. S. T. M. C78-15 (2015) Standard test method for flexural strength of concrete (using a simple beam with third-point loading). ASTM International.

Standard, A. S. T. M. D3039-D3039M-14, Standard test method for tensile properties of polymer matrix composite materials, DOI: 10.1520-D3039-D3039M-14.

Standard, A. S. T. M. E111-04 Standard Test Method for Young's Modulus, Tangent Modulus, and Chord Modulus.

Standard, A. S. T. M. E119-14 Standard Test Methods for Fire Tests of Building Construction and Materials.

Straube, B., Langer, P., & Stumm, A. (2008). The durability of Autoclaved Aerated Concrete. In 11DBMC International Conference on Durability of Building Materials and Components, Istanbul Turkey, May (Vol. 11).

Tanaçan, L., Ersoy, H. Y., & Arpacioğlu, Ü. (2009). Effect of high temperature and cooling conditions on aerated concrete properties. *Construction and building materials*, 23(3), 1240-1248.

Tanner, J. E., Varela, J. L., Klingner, R. E., Brightman, M. J., & Cancino, U. (2005). Seismic testing of autoclaved aerated concrete shearwalls: a comprehensive review. *ACI structural journal*, 102(3).

Thompson, J. D., Higgins, D. G., & Gibson, T. J. (1994). CLUSTAL W: improving the sensitivity of progressive multiple sequence alignment through sequence weighting, position-specific gap penalties, and weight matrix choice. *Nucleic acids research*, 22(22), 4673-4680.

Uddin, N., Fouad, F. H., Vaidya, U. K., Khotpal, A. K., & Serrano-Perez, J. C. (2007). Structural behavior of fiber-reinforced polymer-autoclaved aerated concrete panels. *ACI Structural Journal*, 104(6).

Wittmann, F. H. (1983). *Autoclaved aerated concrete, moisture, and properties*. Elsevier Scientific Pub. Co. Distributors for the US and Canada, Elsevier Science Pub. Co.

Wongpa, J., Kiattikomol, K., Jaturapitakkul, C., & Chindaprasirt, P. (2010). Compressive strength, modulus of elasticity, and water permeability of inorganic polymer concrete. *Materials & Design*, 31(10), 4748-4754.

Yousef, A. E. A. (2009). *Evaluation of the shear design provisions of ACI 523.4 R for autoclaved aerated concrete members* (Doctoral dissertation, The University of Texas at Austin).

Ayudhya, B. I. N. (2011). Compressive and splitting tensile strength of autoclaved aerated concrete (AAC) containing perlite aggregate and polypropylene fiber subjected to high temperatures. *Sonklanakarın Journal of Science and Technology*, 33(5), 555.

Li, M., Qian, C., & Sun, W. (2004). Mechanical properties of high-strength concrete after the fire. *Cement and concrete research*, 34(6), 1001-1005.

## **APPENDIX A—DESIGN EXAMPLES**

### Design Examples of AAC Components

The results of the analytical investigation presented in Chapter VII showed that using the strength design method (Method II) is adequate to calculate the design flexural strength for the suggested composite AAC system proposed in this dissertation. The use of the strength method for to design AAC structural elements strengthened with basalt composite should be sufficient, and the computational effort would not require design iterations as with the non-linear method. The suggested examples discussed and solved in this chapter have already developed and proposed by the ACI 526 committee. Appendix A explains the full details of the design examples proposed by committee ACI 526. In this chapter, the same examples were solved; however; the conventional steel wire mesh reinforcement was replaced with basalt fiber to provide the required tensile strength for the AAC section.

The design of the AAC Floor Panel will follow the following steps:

Step 1: Obtain the material properties of AAC and FRP. Values of  $f'_c$  of AAC and tensile strength of FRP and modulus of elasticity of FRP are required

Step 2: Determine the applied dead loads and live loads that will applied to the AAC panel

Step 3: Obtain the thickness of the panel by assuming the depth and calculate the total deflection of the panel.

Step 4: Compare the calculated deflection with the allowable deflection.

Step 5: Evaluate the ultimate shear strength of the panel assuming that the total shear force will be carried by the AAC material only.

Step 6: Calculate the flexural capacity of the panel cross section using the ultimate strength design (Method II).

Step 7: Compare the applied strength with the actual strength of the panel.

Three detailed examples are presented in Appendix A following the design steps are given in above. Example 1 is a design of an AAC floor panel subjected dead loads and live loads. The example includes design for flexure, shear design and deflection calculations. Example 2 is a design for an AAC shear wall subjected to lateral loads. The example includes design for flexure and shear design. Example 3 is a design for of load-bearing vertical wall panel subjected to eccentric gravity and out-of-plane wind loads. The example includes developing a  $\Phi P_n$ - $\Phi M_n$  interaction diagram for the wall.

### Example 1: Design of an AAC floor panel

Design the following simply supported AAC floor panel shown in Figure A.1 and the section in Figure A.2. Assume the following material properties, uniform loads, and geometry.

Floor panel AAC-4

$$f_{ACC} = 580 \text{ psi}$$

$$f_{FRP} = 266,000 \text{ psi (from the coupon test)}$$

$$E_{FRP} = 13,000 \text{ ksi}$$

$$\text{Dead load, } q_d = 75 \text{ psf}$$

$$\text{Live load, } q_l = 40 \text{ psf}$$

Area of the provided unidirectional basalt fiber  $A_{FRP/in} = 0.02 \text{ in}^2/\text{in}$ .

The width of the total provided basalt fiber is 23 in with total area equal to  $A_{FRP} = 0.46 \text{ in}^2$

Density of AAC-4 =  $44 \text{ lb/ft}^3$

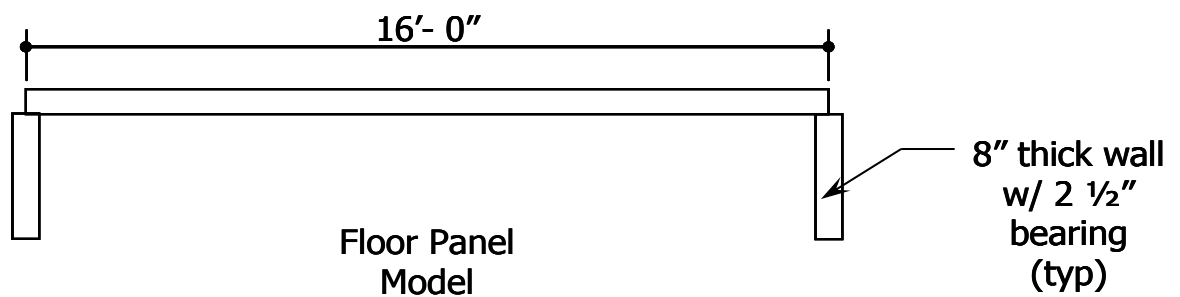
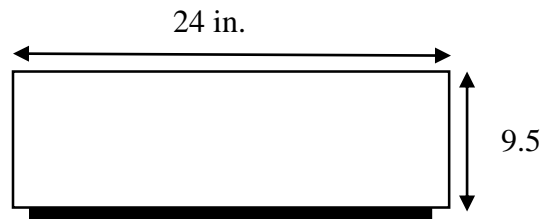


Figure A. 1 Elevation of floor panel



Basalt fiber with a width of 23

Figure A. 2 Cross section for AAC panel.

### Deflections

- a) Start the design with a 10 in. nominal panel. Determine if the actual panel thickness ( $h$ ) of 9.5 in. is adequate for deflection control.

For a simply supported AAC slab, the minimum thickness ( $h$ ) to avoid calculation of deflections is shown below (ACI 318-11, Table 9.5a). The factor  $F1$  adjusts for lightweight concrete.

$$F1 = 1.65 - 0.005w_c = 1.65 - 0.005 \cdot 44 = 1.43$$

$$h = \frac{l \cdot F1 \cdot F2}{20} = \frac{192 \cdot 1.43 \cdot 1}{20} = 13.7 \text{ in}$$

At this point, the designer may wish to start with a 10 in. nominal panel and check deflections. The actual thickness of 9.5 in. will be used to calculate strength properties.

b) Determine properties of AAC.

Calculate modulus of elasticity of AAC (ACI 530/530.1).

$$E_{AAC} = 6500(f'_{AAC})^{0.6} = 6500(580)^{0.6} = 295,800 \text{ psi}$$

Calculate reduced modulus of elasticity of AAC for long-term deflections based on 7.4 (ACI 318-11, Section 9.5.2.5).

$$E'_{AAC} = \frac{E_{AAC}}{1.5} = \frac{295.8 \text{ ksi}}{1.5} = 197 \text{ ksi}$$

Calculate splitting tensile strength of AAC (ACI 530/530.1).

$$f_{iAAC} = 2.4\sqrt{f'_{AAC}} = 2.4\sqrt{580} = 57.8 \text{ psi}$$

Calculate modulus of rupture of AAC (ACI 530/530.1).

$$f_{rAAC} = 2f_{iAAC} = 2(57.8) = 115.6 \text{ psi}$$

Calculate modular ratio (modulus of elasticity of basalt fabric to reduced modulus of elasticity of AAC).

$$n = \frac{E_{FRP}}{E'_{AAC}} = \frac{13000}{197} = 66$$

Determine the transformed moment of inertia and cracking moment.

$$\text{Total area of the fiber} = 0.46 \text{ in.}^2$$

Transformed area of basalt fiber to AAC.

$$A_{FRPt} = n \cdot A_{FRP} = 66 * 0.46 = 30.36 \text{ in.}^2$$

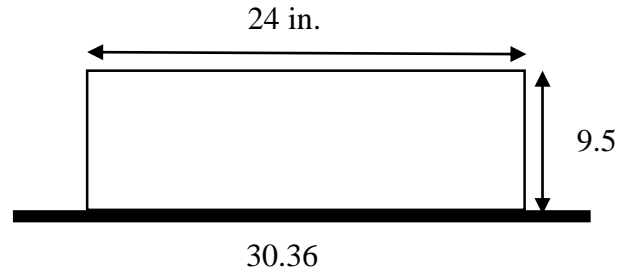


Figure A. 3 Cross section of panel to calculate uncracked transformed moment of inertia using one layer of basalt fiber

Use the parallel axis theorem to determine the uncracked transformed moment of inertia. First, calculate the location of the neutral axis.

$$y' = \frac{30.36 * 9.5 + 228 * 4.75}{24 * 9.5 + 30.36} = 5.3 \text{ in}$$

$$I_{ut} = \frac{bh^3}{12} + bh \cdot \left(5.3 - \frac{h}{2}\right)^2 + A_{FRPt} \cdot (h - 5.3)^2$$

$$\begin{aligned} I_{ut} &= \frac{24 * 9.5^3}{12} + 24 * 9.5 * \left(5.3 - \frac{9.5}{2}\right)^2 + 30.36 * (9.5 - 5.3)^2 \\ &= 2604.6 \text{ in.}^4 \end{aligned}$$

$$M_{cr} = \frac{f_{tAAC} \cdot I_{ut}}{h - 5.3} = \frac{115.6 * 2604.6}{9.5 - 5.3} = 71,688 \text{ lb} - \text{in.}$$

Note: There are no axial loads in this beam example.

- c) Calculate unfactored uniform distributed load and bending moment at midspan of the floor panel.

$$w_a = (75 \text{ psf} + 40 \text{ psf}) \left( \frac{24 \text{ in.}}{12 \text{ in./ft}} \right) \left( \frac{1 \text{ ft}}{12 \text{ in.}} \right) = 19.2 \frac{\text{lb}}{\text{in.}}$$

When calculating the maximum moment, use the clear span or distance between support edges.

$$l_n = 192 \text{ in.} - 2(2.5) = 187 \text{ in.}$$

$$M_a = \frac{w_a l_n^2}{8} = \frac{19.2 \text{ lb/in.} \cdot (187 \text{ in.})^2}{8} = 83,780 \text{ lb-in.}$$

$M_a = 83,780 \text{ lb-in.} > M_{cr} = 42,061 \text{ lb-in.}$ , therefore, calculate the cracked moment of inertia and yielding moment.

- d) Determine the position of neutral axis and cracked transformed a moment of inertia.

Consider only tension steel as illustrated in Figure A.4.



Figure A. 4 Cracked transformed section of the floor panel.

From equilibrium

$$12 * y^2 = 30.36 (9.5 - y)$$

$$y^2 + 2.53y - 24 = 0$$

$$y = 3.8 \text{ in.}$$

$$I_{cr} = 24 * 3.8^3 / 3 + 30.36 (9.5 - 3.8)^2 = 1425.3 \text{ in.}^4$$

e) Determine moment at the maximum strength on the basalt fiber.

$$M_{FRP} = E'_{AAC} \cdot I_{cr} \cdot \left[ \frac{\frac{f_{FRP}}{E_{FRP}}}{h - y} \right]$$

$$M_{FRP} = 197000 * 1425.3 * \left[ \frac{0.01}{9.5 - 3.8} \right] = 492603 \text{ lb} - \text{in.}$$

- f) Determine curvature at cracking and at a maximum of the basalt fiber using mechanics of materials:

$$\phi_{cr} = \left( \frac{M_{cr}}{E'_{AAC} \cdot I_{ut}} \right) = \left( \frac{71688}{197000 \cdot 2604.6} \right) = 0.00014 \quad 1/in$$

$$\phi_{FRP} = \left( \frac{M_{FRP}}{E'_{AAC} \cdot I_{cr}} \right) = \left( \frac{492603}{197000 \cdot 1425.3} \right) = 0.00175 \quad 1/in$$

Use linear interpolation to calculate  $\phi_a$ . This is the curvature at a service moment  $M_a$ .

$$\phi_a = \phi_{cr} + \left[ \frac{M_a - M_{cr}}{M_{FRP} - M_{cr}} \right] (\phi_{FRP} - \phi_{cr})$$

$$\phi_a = 0.00014 + \left[ \frac{83780 - 71688}{492603 - 71688} \right] (0.00175 - 0.00014) = 0.000186 \quad 1/in$$

- g) Calculate equivalent stiffness and deflections. Determine the effective moment of inertia at this service moment,  $M_s$ .

$$E'_{AAC} \cdot I_e = \frac{M_a}{\phi_a}$$

$$E'_{AAC} \cdot I_e = \frac{83780}{0.000186} = 450.43 \times 10^6 \text{ lb} - \text{in}^2$$

$$\delta_{Long-term} = \frac{5w_a l_n^4}{384 E'_{AAC} I_e} = \frac{5 * 19.2 * 187^4}{384 * 450.43 * 10^6} = 0.68 \text{ in}$$

Calculate the allowable deflection for the beam

$$\delta_{allowable} = \frac{l_n}{240} = \frac{187}{240} = 0.78 \text{ in} > 0.68 \text{ in} \quad \text{oK}$$

Consider live load deflections only.

$$w_l = (40 \text{ psf})(2 \text{ ft}) \left( \frac{1 \text{ ft}}{12 \text{ in.}} \right) = 6.67 \frac{\text{lb}}{\text{in.}}$$

$$\delta_{LL} = \frac{5w_l l_n^4}{384 E'_{AAC} I_e} = \frac{5 * 6.67 * 187^4}{384 * 450.43 * 10^6} = 0.23 \text{ in}$$

$$\delta_{allowable,LL} = \frac{l_n}{360} = \frac{187}{360} = 0.52 \text{ in} > 0.23 \text{ in} \quad \text{oK}$$

### Evaluate ultimate shear capacity

The source of the shear capacity for the AAC panel is considered from the AAC material only without any contributions from the basalt fiber.

- a) Determine factored loads and maximum shear force in the panel.

$$q_u = 1.2 (75 \text{ psf}) + 1.6 (40 \text{ psf}) = 154 \text{ psf}$$

$$w_u = 154 \text{ psf} \cdot 2\text{ft} \cdot \frac{1\text{ft}}{12 \text{ in.}} = 25.7 \frac{\text{lb}}{\text{in.}}$$

$$V_u = w_u \frac{l_n}{2} = 25.7 \cdot \frac{\text{lb}}{\text{ft}} \cdot \frac{187\text{ft}}{2} = 2400 \text{ lb}$$

b) Determine shear capacity of floor panel.

$$\begin{aligned} \phi V_{AAC} &= \phi 0.8 \sqrt{f'_{ACC}} b d = \\ 0.75 (0.8) \sqrt{580} (24) (8.61) &= 2986 \text{ lb} \end{aligned}$$

$$\phi V_{AAC} = 2986 \text{ lb} > V_u = 2400 \text{ lb} \quad \text{OK}$$

### Flexural capacity

The maximum factored moment in the panel is calculated in the following.

$$M_u = \frac{w_u l_n^2}{8} = (25.7) \frac{\text{lb}}{\text{in.}} \frac{(187 \text{ in.})^2}{8} = 112,200 \text{ lb-in./panel}$$

Calculate the depth of the compressive stress block based on Figure A.5 by applying equilibrium in the horizontal direction,  $T = C$  and solve for  $a$ , the depth of the compression zone.

$$T = C$$

$$A_{FRP} \cdot f_{FRP} = 0.85 f'_{AAC} \cdot b \cdot a$$

$$23 \cdot 0.002 \cdot 2 \cdot 266000 = 0.85 \cdot 580 \cdot 24 \cdot a$$

Solving for  $a$ ,  $a = 2.06$  in.

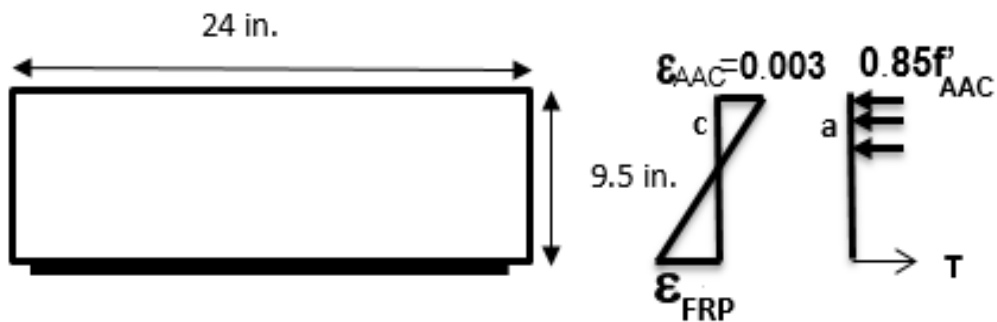


Figure A. 5 Free body diagram of the floor panel.

Now evaluate the nominal flexural capacity.

$$M_n = A_{FRP} \cdot f_{FRP} \left( h - \frac{a}{2} \right) = 23 * 2 * 0.002 * 266000 * \left( 9.5 - \frac{2.06}{2} \right)$$
$$= 207,277 \text{ lb} - \text{in.}$$

$$\phi M_n = 0.65 * 207,277 = 134,730 \text{ lb} - \text{in.}$$

$$\phi M_n = 134,730 \text{ lb} - \text{in.} > M_u = 112,200 \text{ lb} - \text{in.} \text{ OK}$$

### Example 2: Design of an AAC shear wall

Design the two-story AAC shear wall shown in the following. Assume the following material properties, factored loads, and geometry.

AAC-4

$$f_{AAC} = 580 \text{ psi}$$

$$f_{FRP} = 266,000 \text{ psi (from the coupon test)}$$

$$E_{FRP} = 13,000 \text{ ksi}$$

Area of the provided unidirectional basalt fiber  $A_{FRP/in} = 0.015 \text{ in}^2/\text{in}$ .

Factored axial load at each story,  $P_u = 35,000 \text{ lb}$

Factored lateral load at each story,  $F_u = 18,000 \text{ lb}$

Start with 10 in. nominal panels (actual  $t = 9.5 \text{ in}$ .)

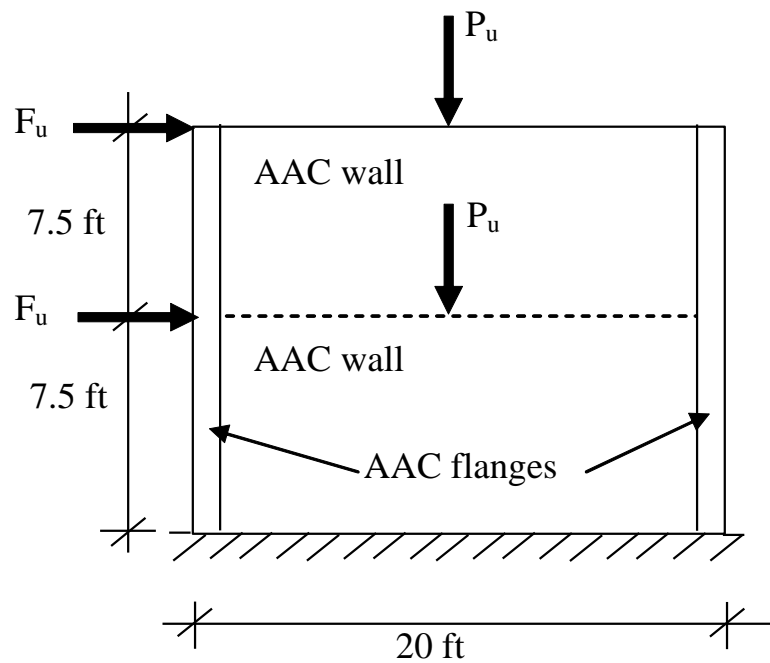


Figure A. 6 AAC shear wall elevation

### Flexural capacity

- a) Determine factored bending moment at the base of the wall.

$$M_u = 18,000 \text{ lb}(15 \text{ ft})(12 \text{ in./ft}) + 18,000 \text{ lb}(7.5 \text{ ft})(12 \text{ in./ft}) \\ = 4,860,000 \text{ lb-in.}$$

- b) Determine flexural capacity at the base of the wall.

Assume flexural enhancement at wall ends only, equal to 30 inches long, located at the flanges of the shear wall as shown in Figure A.7.

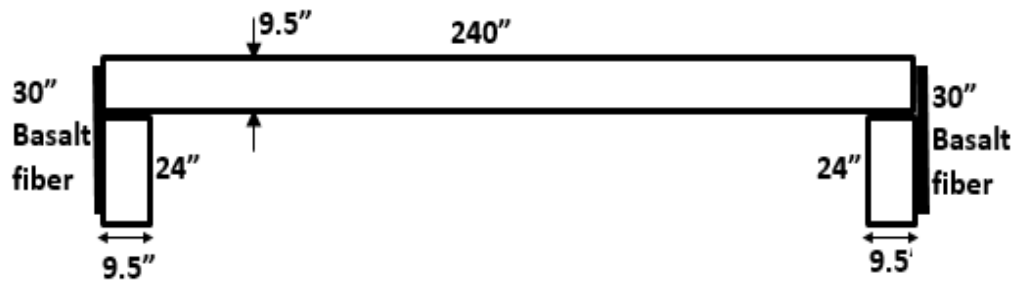


Figure A. 7 Plan view of the AAC shear wall with basalt fiber enhancement

Calculate the tension forces in the basalt fiber (T), assuming that the basalt fiber in the compression side is not going to contribute to the forces equilibrium.

$$T = f_{FRP} \cdot A_{FRP}$$

$$T = 266 * 30 * 0.0015 * 1000 = 11970 \text{ lb.}$$

For equilibrium:

$$C = N_u + T$$

$$N_u = 2(P_u) = 35,000 + 35,000 = 70,000 \text{ lb}$$

$$C = 70\,000 + 11\,970 = 81\,970 \text{ lb.}$$

$$C = 0.85 f'_{AAC} \cdot ab$$

$$a = \frac{81\,970}{0.85 * 580 * 33.5} = 5 \text{ inches}$$

*< the flange width 9.5 inches ok*

Calculate the moment capacity by taking moment about the geometric centroid of the shear wall:

$$M_n = T * \left(\frac{l}{2}\right) + C (l - a)/2$$

$$M_n = 11970 * \left(\frac{240}{2}\right) + 81970 (240 - 5)/2 = 11,067,875 \text{ in-lb}$$

$$\phi M_n = 0.9 * 11,067,875 = 9,961,087 \text{ in - lb}$$

$$\phi M_n = 9,961,087 \text{ in} - \text{lb} > 4,860,000 \text{ in} - \text{lb} \quad \text{ok}$$

### Shear capacity

- a) Determine factored shear force and axial force at the base of the wall.

$$V_u = 2F_u = 2(18,000) = 36,000 \text{ lb}$$

$$N_u = 70,000 \text{ lb}$$

- b) Determine shear capacity at the base of the wall (web shear cracking).

$$\phi V_{AAC} = \phi t l_w \sqrt{f'_{AAC}} \sqrt{1 + \frac{N_u}{2.4 \sqrt{f'_{AAC}} t l_w}} \quad (\text{ACI526})$$

$$\phi V_{AAC} = 0.75(9.5)(240) \sqrt{580} \sqrt{1 + \frac{70,000}{2.4 \sqrt{580} (9.5)(240)}} = 50,960 \text{ lb}$$

$$\phi V_{AAC} = 50,960 \text{ lb} > V_u = 36,000 \text{ lb} \quad \text{OK}$$

- c) Determine factored shear force and axial force at a height of 7.5 ft.

$$V_u = F_u = 18,000 \text{ lb}$$

$$P_u = N_u = 35,000 \text{ lb}$$

d) Determine shear capacity at 7.5 ft from the base of the wall (web shear cracking).

$$\phi V_{AAC} = 0.75(9.5)(240)\sqrt{580} \sqrt{1 + \frac{35,000}{2.4\sqrt{580}(9.5)(240)}} = 46,330 \text{ lb} \quad (7.6.1f)$$

$$\phi V_{AAC} = 46,330 \text{ lb} > V_u = 18,000 \text{ lb} \quad \text{OK}$$

**Example 3: Design of load-bearing vertical wall panel subjected to eccentric gravity and out-of-plane wind loads**

Use AAC4 block

The compressive strength of the block is  $f_{ACC} = 580$  psi

The information data for the basalt fiber are:

$$\epsilon_{FRPmax} = 0.005 \text{ (FHWA)}$$

$$E_{FRP} = 13,000 \text{ ksi}$$

$$A_{FRP} = 0.008 \text{ in.}^2/\text{in.}$$

The applied loads are:

$$q = 60 \text{ psf (Wind pressure)}$$

$$\text{density} = 44 \text{ lb/ft}^3 \text{ (with the FRP weight)}$$

$$\text{Weight} = (44 \text{ lb/ft}^3) \left( \frac{7.87 \text{ in.}}{12 \text{ in./ft}} \right)$$

$$\text{Weight} = 28.9 \text{ lb/ft}^2$$

The other applied load shown in Figure 8.8.

Use one layer of basalt fiber for both faces of the bearing wall.

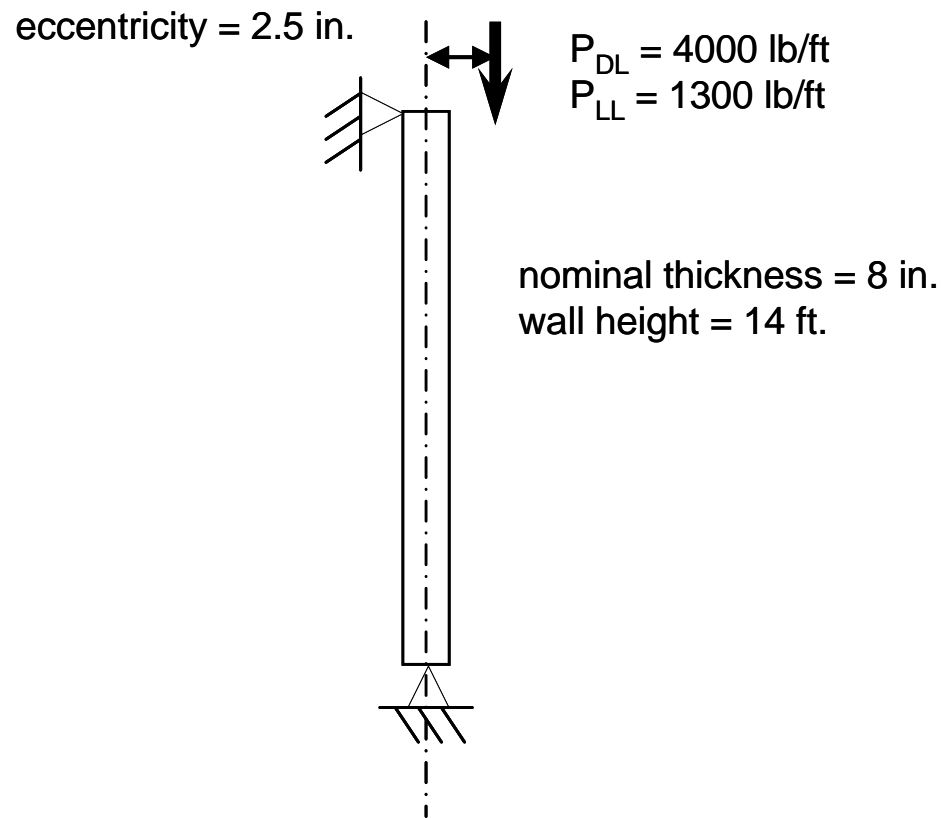


Figure A. 8 Section of AAC bearing wall

Because flexural capacity increases with axial load, and wind loads are much higher than gravity loads, the most critical loading combination is likely  $0.9D + 1.0W$ . Designers should check all critical loading combinations.

$$M_{wind} = \frac{wh^2}{8} = \frac{(60 \text{ lb/ft}^2)(14 \text{ ft})^2}{8} (12 \text{ in./ft}) = 17,640 \text{ lb-in./ft}$$

$$M_{DL}(\text{mid-height}) = \frac{Pe}{2} = \frac{(4000 \text{ lb/ft})(2.5 \text{ in.})}{2} = 5000 \text{ lb-in./ft}$$

$$M_u = 0.9D + 1.0W = 0.9(5000 \text{ lb-in./ft}) + 1.0(17,640 \text{ lb-in./ft}) = 22,140 \text{ lb-in./ft}$$

$$P_u(\text{mid-height}) = 0.9(4000 \text{ lb/ft}) + 0.9\left(\frac{14 \text{ ft}}{2}\right)(28.9 \text{ lb/ft}^2) = 3782 \text{ lb/ft}$$

Check slenderness:

$$\frac{kh}{r} = \frac{h}{r} = \frac{(14\text{ft})(12 \text{ in./ft})}{\frac{7.87 \text{ in.}}{\sqrt{12}}} = \frac{168 \text{ in.}}{2.27 \text{ in.}} = 73.9 < 99$$

$$\therefore \text{Factor} = \left[ 1 - \left( \frac{h}{140r} \right) \right]^2 = \left[ 1 - \left( \frac{168 \text{ in.}}{140(2.27 \text{ in.})} \right) \right]^2 = 0.721$$

This slenderness factor affects the pure axial capacity of the panel as defined in ACI 530/530.1. The interaction diagram will be capped at a value of  $0.721P_n$ .

Continue with factored design actions:

$$P_u = 3782 \text{ lb/ft} \text{ and } M_u = 22,140 \text{ lb-in./ft}$$

Construct moment interaction diagram:

Consider one layer of unidirectional basalt fiber in each face of the bearing wall with an equivalent area of  $0.008 \text{ in}^2/\text{in}$  length. Since the system is brittle and there isn't any explanation in the previous literature regarding the reduction factor, in this case, a conservative value of 0.65 was adopted for this example.

Compare factored loads with strength interaction diagram:

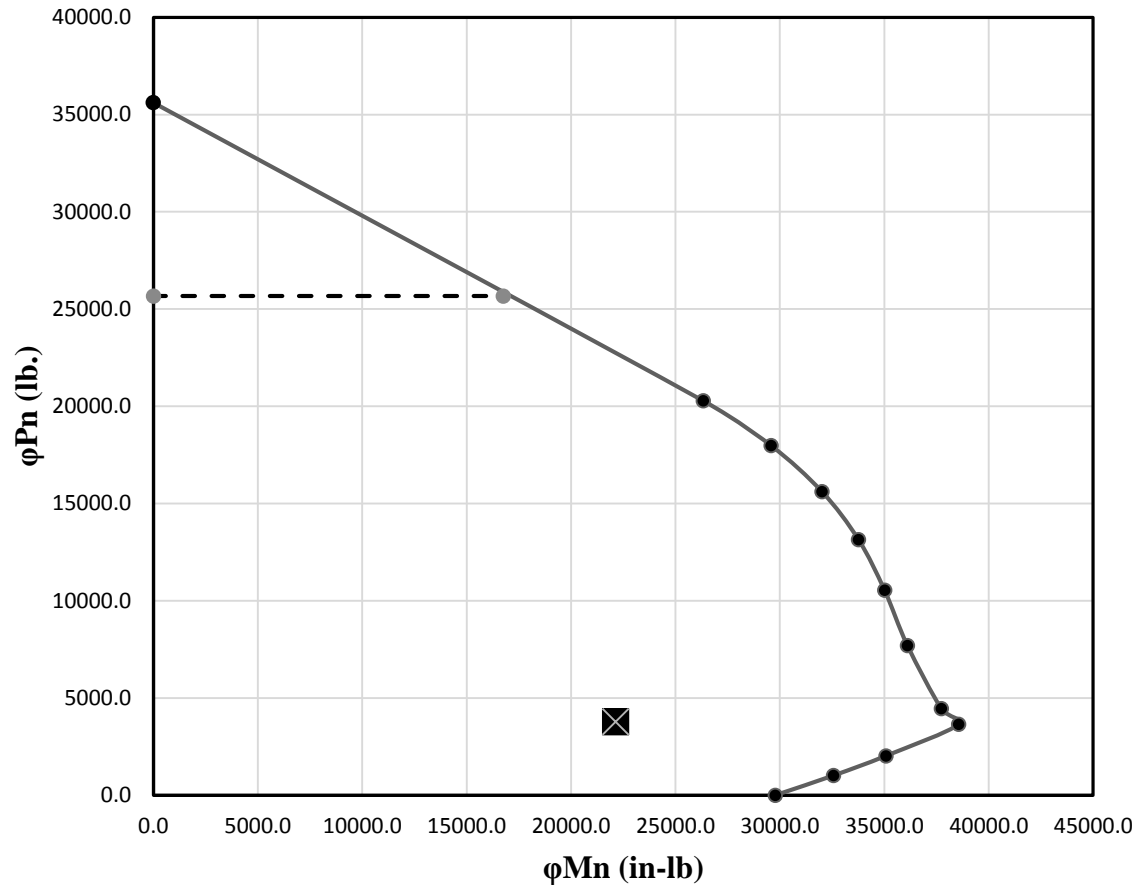


Figure A. 9 Force interaction for 8 inches AAC bearing wall with one layer of basalt fiber as reinforcement

Table A. 1 Values for interaction diagram

Control points	c/d	c (in.)	a (in.)	CAA C (lb.)	εFRP	FFRP(Ksi)	T (lb.)	φ	φPn (lb)	φMn (in-lb)	φPn (lb) with 0.721 cap
Points Controlled by the basalt fiber	0.01	0.08	0.0527	312	0.0050	65	6240	0.65	-3853.2	16752.9	-3853.2
	0.1	0.79	0.5273	3119	0.0050	65	6240	0.65	-2028.4	23404.5	-2028.4
	0.15	1.18	0.7909	4679	0.0050	65	6240	0.65	-1014.5	26725.7	-1014.5
	0.2	1.57	1.0546	6239	0.0050	65	6240	0.65	0.0	29779.6	0.0
	0.25	1.97	1.3182	7799	0.0050	65	6240	0.65	1013.1	32566.2	1013.1
	0.3	2.36	1.5819	9358	0.0050	65	6240	0.65	2026.9	35085.5	2026.9
	0.38	2.99	2.0037	11854	0.0050	65	6240	0.65	3649.0	38560.4	3649.0
Points Controlled by AAC	0.4	3.15	2.10916	12478	0.0045	58.50	5616.0	0.65	4460.2	37726.2	4460.2
	0.5	3.94	2.63645	15597	0.0030	39.00	3744.0	0.65	7704.6	36105.6	7704.6
	0.6	4.72	3.16374	18717	0.0020	26.00	2496.0	0.65	10543.4	35012.0	10543.4
	0.7	5.51	3.69103	21836	0.0013	16.71	1604.6	0.65	13150.5	33761.2	13150.5
	0.8	6.30	4.21832	24956	0.0008	9.75	936.0	0.65	15612.7	32011.2	15612.7
	0.9	7.08	4.74561	28075	0.0003	4.33	416.0	0.65	17978.4	29572.2	17978.4
	1	7.87	5.2729	31194	0.0000	0.00	0.0	0.65	20276.4	26329.9	20276.4
Pure axial load							0.65	35603.8	0	25670.4	

Critical actions at midheight of the wall:

$$P_u = 3782 \text{ lb/ft} \text{ and } M_u = 22,140 \text{ lb-in./ft}$$

The action is inside moment-axial force interaction, and the design is satisfactory if P-delta effects are not considered.

Check secondary moments (P-delta effect):

Determine if  $M_u < M_{cr}$

Evaluate section properties for this panel section assuming that it is uncracked.

$$f_t = 2 \cdot 2.4 \sqrt{f'_{AAC}} = 2 \cdot 2.4 \sqrt{580 \text{ lb/in.}^2} = 115.6 \text{ lb/in.}^2$$

$$f_r + \frac{P_u}{A} = 115.6 + \frac{3782 \text{ lb}}{12 \cdot 7.87 \text{ in.}^2} = 155.6 \text{ psi}$$

Determine uncracked transformed  $I_{ut}$  and  $M_{cr}$ :

$$E_{AAC} = 6500(f'_{AAC})^{0.6} = 6500(580)^{0.6} = 295,800 \text{ lb/in.}^2$$

$$n = \frac{E_{FRP}}{E_{AAC}} = \frac{13,000,000}{296,000} = 44$$

$$A_{FRP} = 0.008 * 12 = 0.096 \text{ in.}^2$$

$$nA_{FRP} = 44 * 0.096 = 4.224 \text{ in.}^2/\text{ft}$$

Because the basalt fiber in the compression side is not participating in taking compression load, neglect this in calculations. Continue to calculate the uncracked transformed moment of inertia about the neutral axis as shown in Figure A.10.

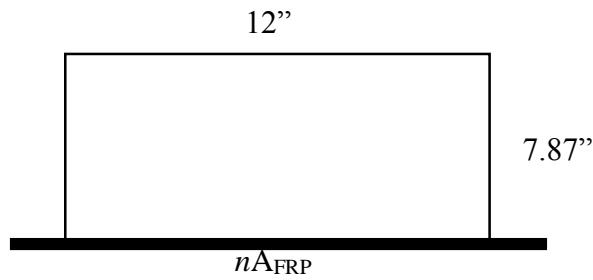


Figure A. 10 2 Horizontal section through 1 ft wide strip of uncracked AAC bearing wall.

$$I_{ut} = \frac{bh^3}{12} + [nA_{FRP} \cdot (h/2)^2]$$

$$I_{ut} = \frac{12 * 7.87^3}{12} + [(44) * 0.096 * (7.87/2)^2]$$

$$I_{ut} = 552.8 \text{ in.}^4$$

$$M_{cr} = \frac{I_{ut}}{h/2} \cdot (f_{tAAC} + \frac{P_u}{A})$$

$$M_{cr} = \frac{552.8}{7.87/2} \cdot \left( 115.6 + \frac{3782}{12 * 7.87} \right) = 21,865 \text{ lb-in./ft}$$

Because  $M_u = 22,140 \text{ lb-in.} > M_{cr} = 21,865 \text{ lb-in.}$ , calculate and use the cracked transformed moment of inertia.

Locate neutral axis and calculate transformed moment of inertia as shown in Figure A.11:

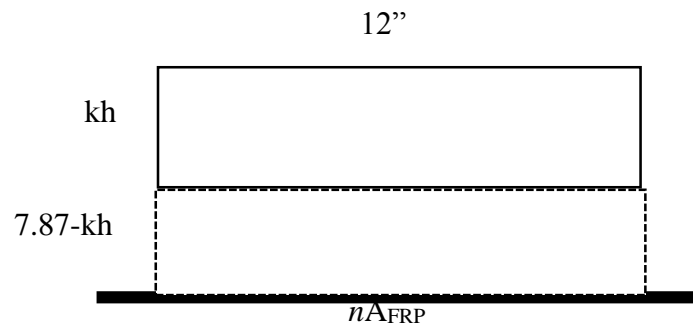


Figure A. 11 Horizontal section through 1 ft wide strip of cracked AAC bearing wall.

Now that the section is cracked, use  $nA_s$  to solve for the neutral axis.

$$b \cdot kh \cdot \frac{kh}{2} = nA_{FRP} \cdot (h - kh)$$

$$12 \cdot kh \cdot \frac{kh}{2} = 4.224 \cdot (7.87 - kh)$$

$$kh^2 + 0.704kh - 5.54 = 0$$

$$kh = \frac{-0.704 + \sqrt{0.704^2 - 4 \cdot 5.54}}{2} = 2 \text{ in.}$$

$$I_{cr} = b \frac{(kh)^3}{3} + nA_{FRP} \cdot (h - kh)^2$$

$$I_{cr} = 12 \frac{(2)^3}{3} + 4.224 \cdot (7.87 - 2)^2$$

$$I_{cr} = 177.5 \text{ in.}^4$$

Use the moment magnifier approach to determine the moment due to P-delta effects:

Based on ACI 530/530.1

$$P_e = \frac{\pi^2 E_{AAC} I_{cr}}{h^2}$$

$$P_e = \frac{\pi^2 * 296000 * 177.5}{(14 * 12)^2}$$

$$P_e = 18,372 \text{ lb}$$

$$\Psi = \frac{1}{1 - \frac{P_u}{P_e}}$$

$$\Psi = \frac{1}{1 - \frac{3782}{18372}} = 1.26$$

$$M_u = \Psi M_{u0}$$

$$M_u = 1.26 * 22,140 = 27896 \text{ lb} - \text{in.}$$

Even with P-delta effects, the factored loads are still within the interaction diagram.

Shear capacity:

Because most of the shear comes from wind, use  $0.9D + 1.0W$  load combination.

$$V_{wind} = \frac{1}{2} \times 60 \text{ lb/ft}^2 \times 14 \text{ ft} = 420 \text{ lb/ft}$$

$$V_{eccentric} = \frac{Pe}{\ell} = \frac{(4000 \text{ lb/ft})(2.5 \text{ in.})}{14 \text{ ft} \times 12 \text{ in./ft}} = 59.5 \text{ lb/ft}$$

$$V_u = 0.9D + 1.0W = 0.9(59.5 \text{ lb/ft}) + 1.0(420 \text{ lb/ft}) = 474 \text{ lb/ft}$$

$$V_n = 0.8\sqrt{f'_{AAC}}bd = 0.8\sqrt{580 \text{ psi}} \cdot 12 \text{ in.} \cdot 6.75 \text{ in.} = 1619 \text{ lb}$$

$$\phi V_n = 0.75 \cdot 1619 \text{ lb} = 1214 \text{ lb}$$

$$V_u = 474 \text{ lb} < \phi V_n = 0.75 \cdot 1619 \text{ lb} = 1214 \text{ lb}$$

Shear capacity is satisfactory.

## **APPENDIX B—DESIGN EXAMPLES**

The following design examples in this Appendix B were developed and reported by the ACI526 committee. The author of this dissertation is part of the committee. A general overview of the approach to the design of autoclaved aerated concrete (AAC) structural walls and floor/roof panels reinforced with steel wire mesh is presented. Variations in design approach from concrete and masonry, and design equations specific to AAC are discussed and provided.

### **Example 1: Design of an AAC floor panel**

Design the following simply supported AAC floor panel. Assume the following material properties, uniform loads, and geometry.

Floor panel AAC-4

$$f_{ACC} = 580 \text{ psi}$$

$$f_y = 80,000 \text{ psi (wires)}$$

$$E_s = 29,000 \text{ ksi}$$

Dead load,  $q_d = 75 \text{ psf}$

Live load,  $q_l = 40 \text{ psf}$

Diameter of longitudinal wires, 7 mm

Diameter of cross wires, 5 mm

Density of AAC-4, 44 lb/ft<sup>3</sup>

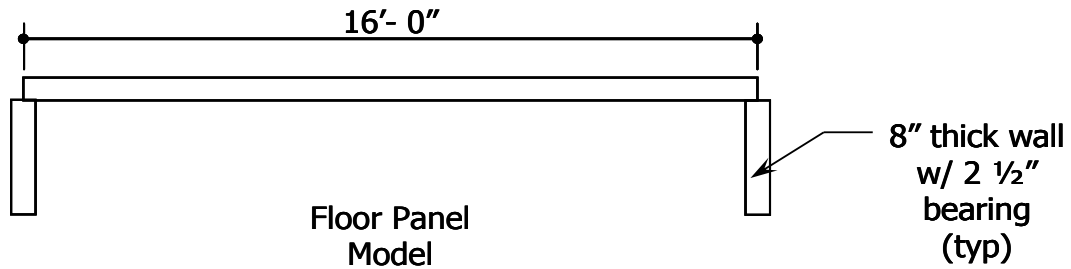


Figure B. 1 Elevation of the floor panel.

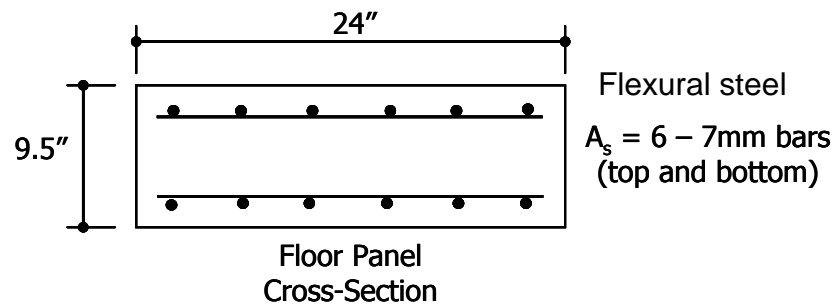


Figure B. 2 Cross section of the panel.

## Deflections

- h) Start the design with a 10 in. nominal panel. Determine if the actual panel thickness ( $h$ ) of 9.5 in. is adequate for deflection control.

For a simply supported AAC slab, the minimum thickness ( $h$ ) to avoid calculation of deflections is shown below (ACI 318-11, Table 9.5a). The first factor adjusts for lightweight concrete, F1; the second factor, F2, adjusts for a higher yield strength of welded wire fabric, 80,000 psi.

$$F1 = 1.65 - 0.005w_c = 1.65 - 0.005 \cdot 44 = 1.43$$

$$F2 = 0.4 + \frac{80,000}{100,000} = 0.4 + 0.8 = 1.2$$

$$h = \frac{l \cdot F1 \cdot F2}{20} = \frac{192 \cdot 1.43 \cdot 1.2}{20} = 9.6 \cdot 1.43 \cdot 1.2 \text{ in.} = 16.5 \text{ in.}$$

At this point, the designer may wish to start with a 10 in. nominal panel and check deflections. The actual thickness of 9.5 in. will be used to calculate strength properties.

- i) Determine properties of AAC.

Calculate modulus of elasticity of AAC (ACI 530/530.1).

$$E_{AAC} = 6500(f'_{AAC})^{0.6} = 6500(580)^{0.6} = 295,800 \text{ psi}$$

Calculate reduced modulus of elasticity of AAC for long-term deflections based on 7.4 (ACI 318-11, Section 9.5.2.5).

$$E'_{AAC} = \frac{E_{AAC}}{1.5} = \frac{295.8 \text{ ksi}}{1.5} = 197 \text{ ksi}$$

Calculate splitting tensile strength of AAC (ACI 530/530.1).

$$f_{tAAC} = 2.4\sqrt{f'_{AAC}} = 2.4\sqrt{580} = 57.8 \text{ psi}$$

Calculate modulus of rupture of AAC (ACI 530/530.1).

$$f_{rAAC} = 2f_{tAAC} = 2(57.8) = 115.6 \text{ psi}$$

Calculate modular ratio (modulus of elasticity of wire to reduced modulus of elasticity of AAC).

$$n = \frac{E_s}{E'_{AAC}} = \frac{29,000}{197} = 147$$

- j) Determine the transformed moment of inertia and cracking moment.

Area of longitudinal wire = 0.06 in.<sup>2</sup>/wire.

Transformed area of longitudinal wires to AAC.

$$A_{st} = (n-1)A_s = 146(6 \text{ wires})(0.0597 \text{ in.}^2) = 52.3 \text{ in.}^2$$

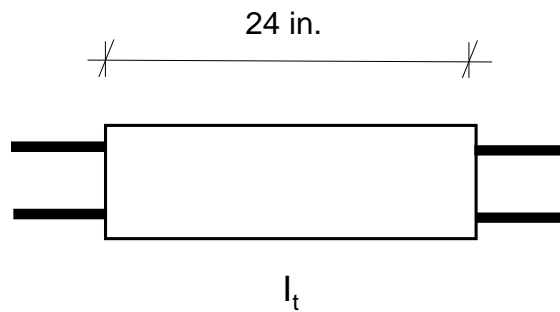


Figure B. 3 Cross section of the panel to calculate the uncracked transformed moment of inertia using two layers of steel. Actual thickness, h, is 9.5 in.

Use the parallel axis theorem to determine the uncracked transformed moment of inertia. Top and bottom cover is 3/4 in.

$$I_{ut} = \frac{bh^3}{12} + 2A_{st} \left( \frac{h}{2} - \text{cover} - \frac{d_b}{2} \right)^2 =$$

$$\frac{24(9.5)^3}{12} + 2(52.3) \left( \frac{9.5}{2} - 0.75 - \frac{0.28}{2} \right)^2 = 3273 \text{ in.}^4$$

$$M_{cr} = \frac{f_{rAAC} I_{ut}}{\frac{h}{2}} = \frac{115.6(3273)}{\frac{9.5}{2}} = 79,650 \text{ lb-in. (ACI 530/530.1)}$$

Note: There are no axial loads in this beam example.

- k) Calculate unfactored uniform distributed load and bending moment at midspan of the floor panel.

$$w_a = (75 \text{ psf} + 40 \text{ psf}) \left( \frac{24 \text{ in.}}{12 \text{ in./ft}} \right) \left( \frac{1 \text{ ft}}{12 \text{ in.}} \right) = 19.2 \frac{\text{lb}}{\text{in.}}$$

When calculating the maximum moment, use the clear span or distance between support edges.

$$l_n = 192 \text{ in.} - 2(2.5) = 187 \text{ in.}$$

$$M_a = \frac{w_a l_n^2}{8} = \frac{19.2 \text{ lb/in.} \cdot (187 \text{ in.})^2}{8} = 83,780 \text{ lb-in.}$$

$M_a = 83,780 \text{ lb-in.} > M_{cr} = 79,650 \text{ lb-in.}$ , therefore, calculate the cracked moment of inertia and yielding moment.

- l) Determine the position of neutral axis and cracked transformed a moment of inertia.

Consider only tension steel as illustrated in Figure B.4.

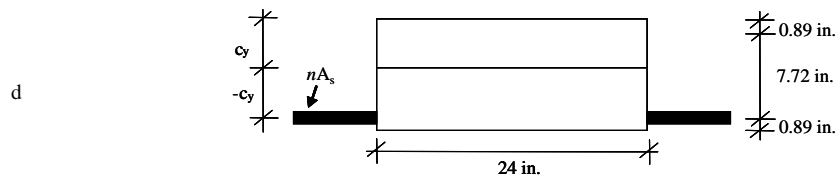


Figure B. 4 Cracked, transformed section of the floor panel.

$$d = h - \text{cover} - \frac{d_b}{2} = 9.5 \text{ in.} - 0.75 \text{ in.} - 0.14 \text{ in.} = 8.61 \text{ in.}$$

For equilibrium:

$$(52.3)(8.61 - c_y) - \left(\frac{24}{2}\right)c_y^2 = 0$$

The position of neutral axis,  $c_y = 4.32 \text{ in.}$

$$I_{cr} = \frac{24(4.32)^3}{3} + 52.3(8.61 - 4.32)^2 = 1608 \text{ in.}^4$$

m) Determine moment at yielding of longitudinal wires.

$$M_y = E'_{AAC} I_{cr} \left( \frac{f_y}{E_s} \right) =$$

$$197,000 \text{ psi} (1608 \text{ in.}^4) \left( \frac{80 \text{ ksi}}{29,000 \text{ ksi}} \right) = 203,800 \text{ lb-in.}$$

n) Determine curvature at cracking and at yielding of the cross wires using mechanics of materials:

$$\phi_{cr} = \left( \frac{M_{cr}}{E'_{AAC} I_{ut}} \right) = \left( \frac{79,650}{197(1000)(3273)} \right) = 0.000123 \frac{1}{\text{in.}}$$

$$\phi_y = \left( \frac{M_y}{E'_{AAC} I_{cr}} \right) = \left( \frac{203,800}{197(1000)(1608)} \right) = 0.000643 \frac{1}{\text{in.}}$$

Use linear interpolation to calculate  $\phi_a$ . This is the curvature at a service moment  $M_a$ .

$$\phi_a = \phi_{cr} + \left( \frac{M_a - M_{cr}}{M_y - M_{cr}} \right) (\phi_y - \phi_{cr})$$

$$\phi_a = 0.000123 + \left( \frac{83,780 - 79,650}{203,800 - 79,650} \right) (0.000643 - 0.000123) = 0.000141 \frac{1}{\text{in.}}$$

- o) Calculate equivalent stiffness and deflections. Determine the effective moment of inertia at this service moment,  $M_s$ .

$$E'_{AAC} I_e = \frac{M_a}{\phi_a} = \frac{83,780}{0.000141} = 594 \times 10^6 \text{ lb-in.}^2$$

$$\delta_{long-term} = \left( \frac{5w_a l_n^4}{384 E'_{AAC} I_e} \right) = \left( \frac{5(19.2 \text{ lb/in.})(187 \text{ in.})^4}{384(594 \times 10^6 \text{ lb-in.}^2)} \right) = 0.514 \text{ in.}$$

$$\delta_{allowable} = \frac{l_n}{240} = \frac{187}{240} = 0.779 \text{ in. This is the allowable deflection for this beam.}$$

$$\delta_{long-term} = 0.514 \text{ in.} < \delta_{allowable} = 0.779 \text{ in.} \quad \text{OK}$$

Consider live load deflections only.

$$w_l = (40 \text{ psf})(2 \text{ ft}) \left( \frac{1 \text{ ft}}{12 \text{ in.}} \right) = 6.67 \frac{\text{lb}}{\text{in.}}$$

$$\delta_{LL} = \left( \frac{5w_l l_n^4}{384 E'_{AAC} I_e} \right) = \left( \frac{5(6.67)(187)^4}{384(594 \times 10^6)} \right) = 0.179 \text{ in.}$$

$$\delta_{max-LL} = \frac{l_n}{360} = \frac{187}{360} = 0.519 \text{ in.}$$

$$\delta_{LL} = 0.179 \text{ in.} < \delta_{max} = 0.519 \text{ in.} \quad \text{OK}$$

**Evaluate ultimate shear capacity**

c) Determine factored loads and maximum shear force in the panel.

$$q_u = 1.2 (75 \text{ psf}) + 1.6 (40 \text{ psf}) = 154 \text{ psf}$$

$$w_u = 154 \text{ psf} \cdot 2\text{ft} \cdot \frac{1\text{ft}}{12 \text{ in.}} = 25.7 \frac{\text{lb}}{\text{in.}}$$

$$V_u = w_u \frac{l_n}{2} = 25.7 \cdot \frac{\text{lb}}{\text{ft}} \cdot \frac{187\text{ft}}{2} = 2400 \text{ lb}$$

d) Determine shear capacity of floor panel.

$$\begin{aligned} \phi V_{AAC} &= \phi 0.8 \sqrt{f'_{ACC}} bd = && \text{Eq. (7.5.1c)} \\ 0.75(0.8) \sqrt{580} (24)(8.61) &= 2986 \text{ lb} \end{aligned}$$

$$\phi V_{AAC} = 2986 \text{ lb} > V_u = 2400 \text{ lb} \quad \text{OK}$$

## Anchorage

Evaluate the maximum expected shear in the beam to follow the prescriptive design approach outlined in 7.2.3.

$$V_{max} = \frac{V_u}{\phi} = \frac{2400}{0.75} = 3200 \text{ lb}$$

Calculate the number of cross wires required in each half of the panel using Eq. (7.2.3d).

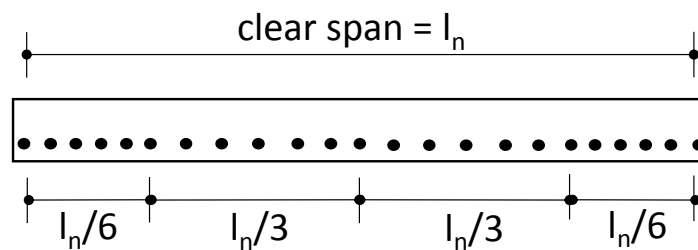
$$n_{cross, \min} = \frac{V_{max} l_n}{5.1d \cdot d_{cross} l_{cross} f'_{AAC}} = \frac{3200 \cdot 187}{5.1(8.61) \left( \frac{5}{25.4} \right) (22)(580)} = 5.42$$

Use six cross wires in the end zone or  $l_n/6$  from each support. Because it is important to have an anchorage in the bearing area, the designer should include the bearing length in the spacing calculation. Designers should ensure at least one cross wire is located within the bearing area.

$$\text{End Zone} = \frac{l_n}{6} + \text{bearing width} = \frac{187}{6} + 2.5 = 33.7 \text{ in.}$$

$$s_{req'd \text{ end zone}} = \frac{33.7 - 1}{5} = 6.53 \text{ in.}$$

Use a conservative stirrup spacing of 6 in. in the end zone. In the center portion of the panel, use a cross wire spacing of 12 in. A total of 24 cross wires will be used in this panel.



Six bars in end zone.  $l_n/3=5.2$  ft. With  $s=12''$ , a total of 6 bars is sufficient to develop the longitudinal steel.

Figure B. 5 Floor panel divided into end zones ( $l_n/6$  from support) and intermediate zones ( $l_n/3$  from centerline).

### Flexural capacity

The maximum factored moment in the panel is calculated in the following.

$$M_u = \frac{w_u l_n^2}{8} = (25.7) \frac{\text{lb} (187 \text{ in.})^2}{8} = 112,200 \text{ lb-in./panel}$$

Assuming that the steel yields, calculate the depth of the compressive stress block based on Figure B.6.

$$T = A_s f_y = 0.358 \text{ in.}^2 (80 \text{ ksi}) = 28.6 \text{ kips}$$

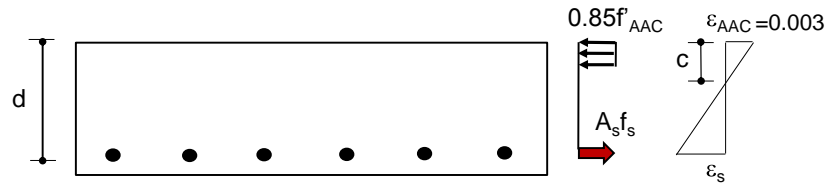


Figure B. 6 Free-body diagram of the floor panel. Only tensile steel showed for clarity

Apply equilibrium in the horizontal direction,  $T = C$  and solve for  $a$  the depth of the compression zone.

$$T = C = 0.85f'_{AAC} a b_w = 0.85(0.58 \text{ ksi})(a)(24 \text{ in.}) = 28.6 \text{ kips}$$

Solving for  $a$ ,  $a = 2.42 \text{ in.}$

Determine stress in longitudinal reinforcement based on bearing capacity of cross wires.

Based on Figure B.6, a total of 10 cross wires are available to resist the moment on either side of the center wire. The designer should check the stress that can be developed in the longitudinal wires.

$$A_s f_s = n_{cross} l_{cross} f'_{AAC} d_{cross}$$

$$f_s = \frac{n_{cross} l_{cross} f'_{AAC} d_{cross}}{A_s} = \frac{10(22)(0.58)(0.197)}{(0.358)} = 70.2 \text{ ksi}$$

The assumption that the steel yields is not valid because anchorage of the cross wires will reduce the maximum stress in the longitudinal steel. The designer should revise the analysis using limiting stress of 70.2 ksi in the steel.

$$T = A_s f_s = 0.358 \text{ in.}^2 (70.2 \text{ ksi}) = 25.1 \text{ kip}$$

$$T = C = 0.85 f'_{AAC} a b_w = 0.85 (0.58 \text{ ksi}) (a) (24 \text{ in.}) = 25.1 \text{ kip}$$

Solving for  $a$  gives a reduced depth of the compressive stress block.

$$a = 2.12 \text{ in.}$$

Now evaluate the nominal flexural capacity.

$$M_n = A_s f_s \left( d - \frac{a}{2} \right) = 0.358 \cdot 70.2 \left( 8.61 - \frac{2.12}{2} \right) = 189,700 \text{ lb-in.}$$

Check strains for tensile reinforcement. Because the steel remains within the elastic zone, Hooke's law is valid.

$$\epsilon_s = \left( \frac{f_s}{E_s} \right) = \frac{70.2}{29,000} = 0.00242$$

This section is between tension and compression-controlled. Interpolate to determine the strength reduction factor.

$$\phi = 0.65 + \left( \frac{0.00242 - 0.002}{0.005 - 0.002} \right) (0.9 - 0.65) = 0.685$$

$$\phi M_n = 0.685 (189.7) = 130 \text{ kip-in.}$$

$$\phi M_n = 130 \text{ kip-in.} > M_u = 112.2 \text{ kip-in.} \quad \text{OK}$$

Now check  $A_{smin}$ .

$$A_{smin} = \frac{4 \sqrt{f'_{AAC}} b_w d}{f_y} = \frac{4 \sqrt{580} \cdot 24 \text{ in.} \cdot 8.61 \text{ in.}}{80,000} = 0.249 \text{ in.}^2 \text{ Eq. (7.3.2f)}$$

$$A_s = 6(0.0597 \text{ in.}^2) = 0.358 \text{ in.}^2 \quad A_{smin} = 0.248 \text{ in.}^2 \text{ OK}$$

Check wall-panel connection for shear force on critical section

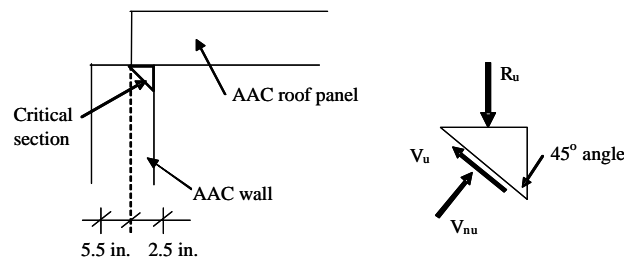


Figure B. 7 the Free body of the corner of AAC roof panel at support.

- a) Determine vertical reaction on the wall in a 1-in. wide strip using factored loads.

First, evaluate the reaction in a single panel. Next, convert this to a 1 in. wide strip for design purposes.

$$R_u = \frac{w_u l_n}{2} = \left( \frac{25.7 \cdot 187}{2} \right) = 2400 \text{ lb per panel width.}$$

Convert the vertical reaction to  $V_u$  as shown in Fig. A.1g.

$$\frac{V_u}{\text{in.}} = \frac{R_u \sqrt{2}}{\text{in.} \cdot 2} = \frac{100 \sqrt{2}}{2} = 70.7 \frac{\text{lb}}{\text{in.}}$$

- b) Determine shear capacity

$$f_v = 0.15 f'_{AAC} = 0.15(580) = 87 \text{ psi ACI 530/530.1}$$

$$\phi V_n = \phi f_v A_d = 0.75(87)\sqrt{(2.5)^2 + (2.5)^2} = 231 \frac{\text{lb}}{\text{in.}}$$

$$\phi V_n = 231 \frac{\text{lb}}{\text{in.}} > V_u = 70.7 \frac{\text{lb}}{\text{in.}} \quad \text{OK}$$

### Example 2: design of an AAC shear wall

Design the two-story AAC shear wall shown in the following. Assume the following material properties, factored loads, and geometry.

AAC-4

$$f_{AAC} = 580 \text{ psi}$$

$$f_y = 60,000 \text{ psi (flexural reinforcement)}$$

$$E_s = 29,000 \text{ ksi}$$

Factored axial load at each story,  $P_u = 35,000 \text{ lb}$

Factored lateral load at each story,  $F_u = 18,000 \text{ lb}$

Start with 10 in. nominal panels (actual  $t = 9.5 \text{ in.}$ )

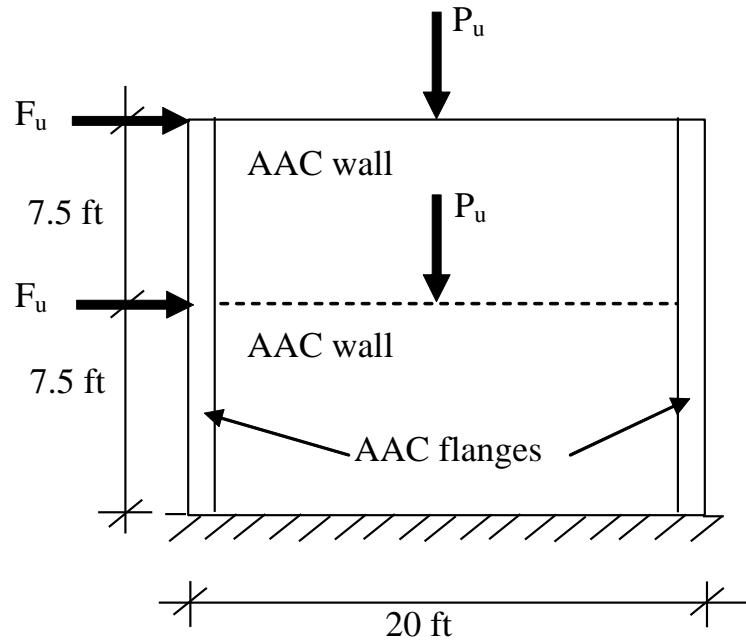


Figure B. 8 AAC shear wall elevation.

### Flexural capacity

- c) Determine factored bending moment at the base of the wall.

$$M_u = 18,000 \text{ lb}(15 \text{ ft})(12 \text{ in./ft}) + 18,000 \text{ lb}(7.5 \text{ ft})(12 \text{ in./ft}) \\ = 4,860,000 \text{ lb-in.}$$

- d) Determine flexural capacity at the base of the wall.

Assume flexural reinforcement at wall ends only, equal to one No. 4 bar, located 24 in. from the wall ends.

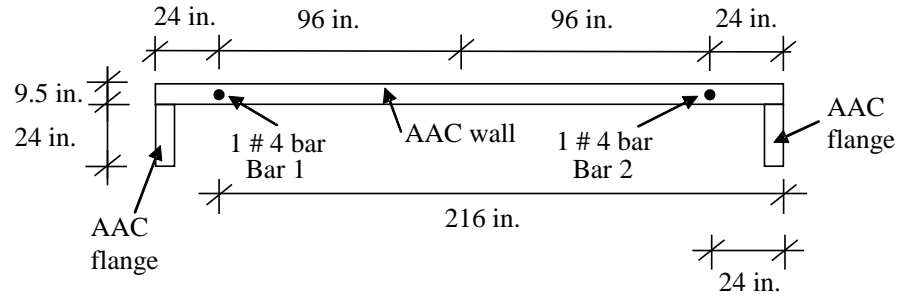


Figure B. 9 Plan view of AAC shear wall and flexural reinforcement.

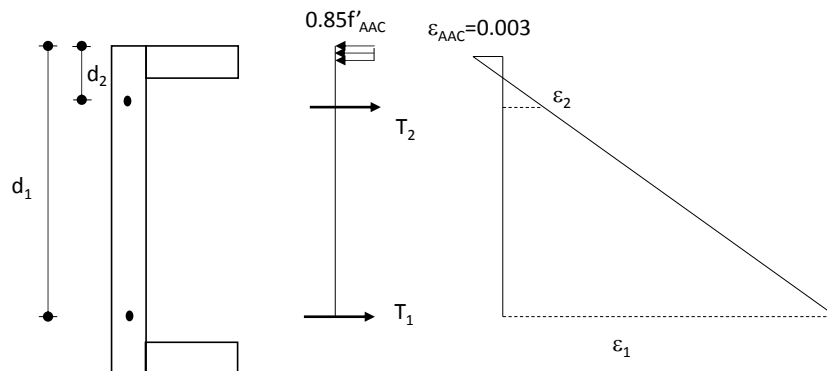


Figure B. 10 Plan view of a wall with ACI nomenclature, a free-body diagram of the wall, and strain distribution. Wall is rotated for ease of reading.

Calculate forces in bars (designated here as  $T_1$  and  $T_2$ ) assuming that both bars are yielding. Bar 1 is farther from the neutral axis; Bar 2 is closer. Assume both bars have yielded.

$$T_1 = T_2 = A_s f_y = 0.2 \text{ in.}^2 (60,000 \text{ psi}) = 12,000 \text{ lb}$$

For equilibrium:

$$C = N_u + T_1 + T_2$$

$$N_u = 2(P_u) = 35,000 + 35,000 = 70,000 \text{ lb}$$

$$C = 0.85 f'_{AAC} ab = N_u + T_1 + T_2 = 94,000 \text{ lb}$$

$$a = \frac{N_u + T_1 + T_2}{0.85 f'_{AAC} b} = \frac{94,000}{0.85 \cdot 580 \cdot 33.5} = 5.69 \text{ in.}$$

Check if Bar 2, closer to the neutral axis, has yielded.

$$c = \frac{a}{\beta_1} = \frac{5.69}{0.67} = 8.49 \text{ in.}$$

$$\varepsilon_2 = \frac{(d_2 - c)}{c} (\varepsilon_{AAC}) = \frac{(24 - 8.49)}{8.49} (0.003) = 0.00548$$

$$\varepsilon_y = \frac{f_y}{E_s} = \frac{60,000}{29,000,000} = 0.0021$$

$\varepsilon_2 = 0.00548 > \varepsilon_y = 0.0021$  The assumption that Bar 2 yields is OK

$\varepsilon_1$  will exceed this value; therefore, Bar 1 yields and the flexural capacity is tension controlled. Note: Sufficient shear connectors are required to engage the entire flange width.

Take moment about the geometric centroid of the wall.

$$M_n = T_1 \left( 216 - \frac{l_w}{2} \right) - T_2 \left( \frac{l_w}{2} - 24 \right) + C \left( \frac{l_w - a}{2} \right)$$

$$M_n = 12,000 \left( 216 - \frac{240}{2} \right) - 12,000 \left( \frac{240}{2} - 24 \right) + 94,000 \left( \frac{240 - 5.69}{2} \right) = 11,010,000 \text{ lb-in.}$$

$$\phi M_n = 0.9 (11,010,000) = 9,910,000 \text{ lb-in.}$$

$$\phi M_n = 9,910,000 \text{ lb-in.} > M_u = 4,860,000 \quad \text{OK}$$

### Shear capacity

e) Determine factored shear force and axial force at the base of the wall.

$$V_u = 2F_u = 2(18,000) = 36,000 \text{ lb}$$

$$N_u = 70,000 \text{ lb}$$

f) Determine shear capacity at the base of the wall (web shear cracking).

$$\phi V_{AAC} = \phi t_w \sqrt{f'_{AAC}} \sqrt{1 + \frac{N_u}{2.4 \sqrt{f'_{AAC}} t_w}} \quad \text{Eq. (7-40)}$$

$$\phi V_{AAC} = 0.75(9.5)(240)\sqrt{580} \sqrt{1 + \frac{70,000}{2.4\sqrt{580}(9.5)(240)}} = 50,960 \text{ lb}$$

$$\phi V_{AAC} = 50,960 \text{ lb} > V_u = 36,000 \text{ lb} \quad \text{OK}$$

g) Determine factored shear force and axial force at the height of 7.5 ft.

$$V_u = F_u = 18,000 \text{ lb}$$

$$P_u = N_u = 35,000 \text{ lb}$$

h) Determine shear capacity at 7.5 ft from the base of the wall (web shear cracking).

$$\phi V_{AAC} = 0.75(9.5)(240)\sqrt{580} \sqrt{1 + \frac{35,000}{2.4\sqrt{580}(9.5)(240)}} = (7.6.1f) \\ 46,330 \text{ lb}$$

$$\phi V_{AAC} = 46,330 \text{ lb} > V_u = 18,000 \text{ lb} \quad \text{OK}$$

- i) Determine shear capacity at base of wall (crushing of the diagonal strut).

$$\phi V_{AAC} = 0.75(0.17) f'_{AAC} t \frac{h(l_w)^2}{h^2 + \left(\frac{3l_w}{4}\right)^2} \quad \text{ACI 530/530.1}$$

$$\phi V_{AAC} = 0.75(0.17)(580)(9.5) \frac{90(240)^2}{90^2 + \left(\frac{3(240)}{4}\right)^2} = 89,920 \text{ lb}$$

$$\phi V_{AAC} = 89,920 \text{ lb} > V_u = 36,000 \text{ lb} \quad \text{OK}$$

- j) Determine sliding shear capacity at the bottom of the wall with a thin-bed mortar joint. Capacity could be governed by friction across a leveling-bed joint, or across an AAC-to-AAC joint created by the propagation of a flexural tensile crack across an interface. In the latter case, the coefficient of friction between two pieces of AAC governs, because the thin-bed mortar is stronger than the AAC material, and a crack will create an AAC-AAC interface rather than an AAC to thin-bed mortar interface.

$\mu = 1$  at a leveling bed joint (ACI 530/530.1)

$$\phi V_{ss} = \phi(\mu N_u)$$

Neglect additional force in tensile steel. Use a factor of 1.07 from ACI 530/530.1 as described in 7.6.4.

$$\phi V_{ss} = 0.75(1.07(1)(70,000)) = 56,170 \text{ lb}$$

$$\phi V_{ss} = 56,170 \text{ lb} > V_u = 36,000 \text{ lb} \quad \text{OK}$$

$\mu = 0.75$  for AAC against AAC (ACI 530/530.1)

$$\phi V_{ss} = 1.07\phi(\mu N_u)$$

Neglect additional force in tensile steel.

$$\phi V_{ss} = 0.75(1.07 \cdot 0.75(70,000)) = 42,130 \text{ lb}$$

$$\phi V_{ss} = 42,130 \text{ lb} > V_u = 36,000 \text{ lb} \quad \text{OK}$$

### Example 3: design of an AAC diaphragm

Design the AAC diaphragm. Assume the following material properties, factored loads, and geometry.

Use Class 4 AAC

$$f_{AAC} = 580 \text{ psi}$$

$$f_{grout} = 3000 \text{ psi}$$

$$f_y = 60,000 \text{ psi}$$

Factored lateral load at each story based on seismic design,  $F_u = 18,000 \text{ lb}$

Ring beam reinforcement, two No. 5, and a grouted width of 5 in. inside of a 1.5 in. AAC form block

Grouted key reinforcement, one No. 5

AAC panels are connected with thin-bed mortar at the bottom of the grouted key.

Confining cages are placed in the ring beam in accordance with 7.8.2.2.

Floor panel thickness is 8 in. nominal and 7.87 in. actual based on production data.

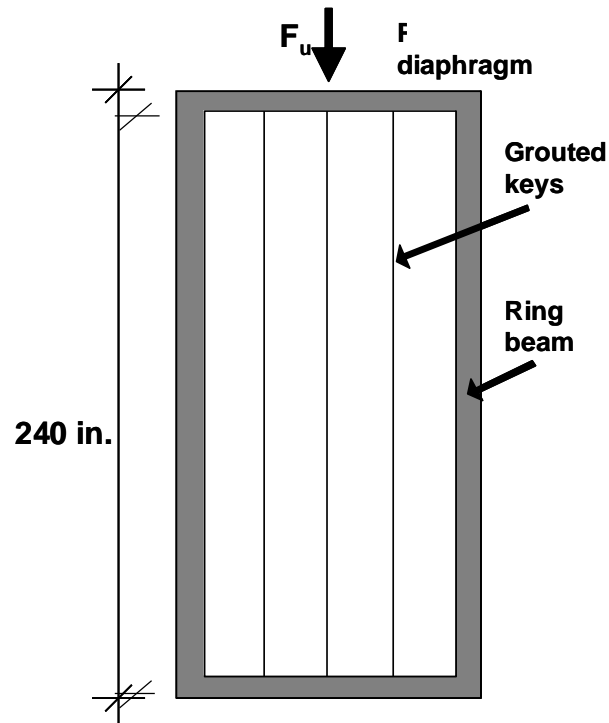


Figure B. 11 Plan view of the diaphragm.

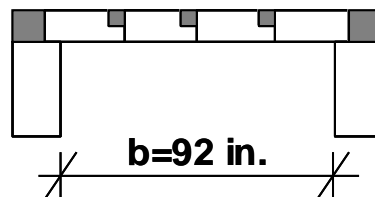


Figure B. 12 Section through short dimension of the diaphragm.

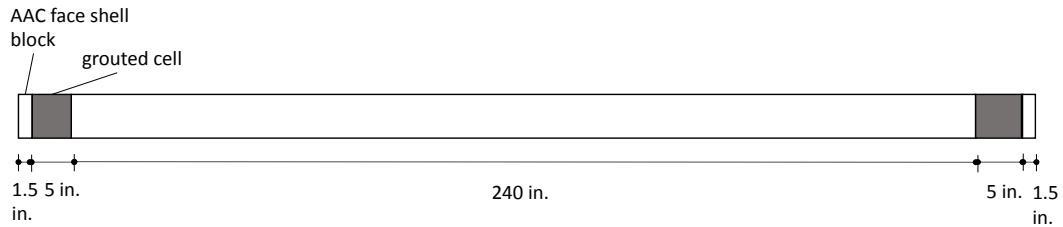


Figure B. 13 Section through long dimension of the diaphragm.

a) Design diaphragm for flexure

$$M_u = \frac{F_u l}{4} = \frac{18,000 \text{ lb} \cdot 92 \text{ in.}}{4} = 414,000 \text{ lb-in.}$$

$$T = A_s f_y = 2 \cdot 0.31 \cdot 60000 = 37,200 \text{ lb}$$

### Tensile force that can develop within the bond beam

Determine the depth of the equivalent stress block.

$$a = \frac{C}{0.85 f'_{grout} b} = \frac{37,200 \text{ lb}}{0.85(3000 \text{ psi})(7.87 \text{ in.})} = 1.85 \text{ in.}$$

where  $a$  is less than the width of the grouted key, equal to 5 in. No further analysis including the AAC panels is required.

$$d = 240 \text{ in.} + 2.5 \text{ in.} + 5 \text{ in.} = 247.5 \text{ in.}$$

Add the grouted key width on the compression side plus half of the grouted key width on the tension side. Neglect the face shell block around the grouted bond beam in calculations.

$$\begin{aligned} M_n &= \\ A_s f_y \cdot \left(d - \frac{a}{2}\right) &= 2(0.31 \text{ in}^2 \cdot 60000 \text{ lb})(247.5 \text{ in.} - \frac{1.85 \text{ in.}}{2}) \\ &= 9,172,500 \text{ lb-in.} \end{aligned}$$

$$\phi M_n = 0.9(9,172,500) = 8,255,000 \text{ lb-in.} > M_u = 414,000 \text{ lb-in. OK}$$

b) Design diaphragm for shear based on adhesion

**Case 1:** Potential failure at a joint between the panel and grouted key.

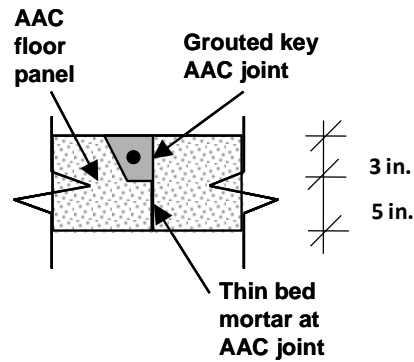


Figure B. 14 Section through the grouted key

The total resistance is the adhesion of the grouted area plus the adhesion of the thin-bed mortar area, as discussed in 7.1.7. The widths (measured vertically) of the grouted and the thin-bed portions of the panel-to-panel joint are as follows:

$$b_{grout} = 3 \text{ in.}$$

$$b_{thin-bed} = 5 \text{ in.}$$

$$V_{grout} = \tau_{grout} b_{grout} l_{panel} = (50 \text{ psi})(3 \text{ in.})(240 \text{ in.}) = 36,000 \text{ lb}$$

(Note:  $\tau_{grout}$  is from ACI 530/530.1).

$$V_{thin-bed} = \tau_{thin-bed} b_{thin-bed} l_{panel} = (18 \text{ psi})(5 \text{ in.})(240 \text{ in.}) = 21,600 \text{ lb}$$

$$V_{total} = V_{grout} + V_{thin-bed} = 57,600 \text{ lb}$$

$$\phi V_{total} = (0.6)(57,600 \text{ lb}) = 34,560 \text{ lb} > \frac{F_u}{2} = 9000 \text{ lb}$$

Use strength reduction factor of 0.6 for seismic based on ACI 318-11, Section 9.3.4.

**Case 2:** Potential failure at a joint between panel and bond beam

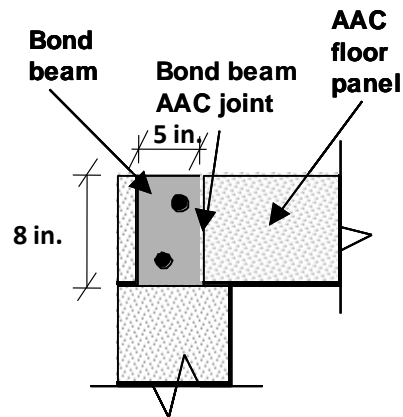


Figure B. 15 Detail of joint between panel and bond beam.

$$b_{grout} = 7.87 \text{ in.}$$

$$V_{grout} = \tau_{grout} b_{grout} l_{panel} = 50 \cdot 7.87 \cdot (240) = 94,440 \text{ lb}$$

(Note:  $\tau_{grout}$  is from ACI 530/530.1).

$$\phi V_{total} = (0.6)(94,440) = 56,660 \text{ lb} > \frac{F_u}{2} = 9000 \text{ lb}$$

Use strength reduction factor of 0.6 for seismic based on ACI 318-11, Section 9.3.4.

c) Design diaphragm for shear based on truss model

One No. 5 bar in each grouted key.

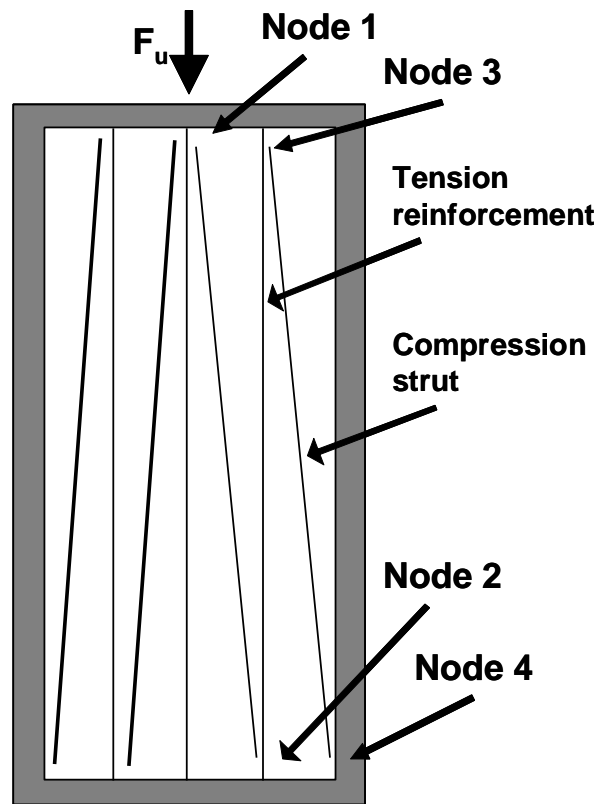


Figure B. 16 Truss model for the diaphragm.

In this model, the compression chords act as diagonal compression members.

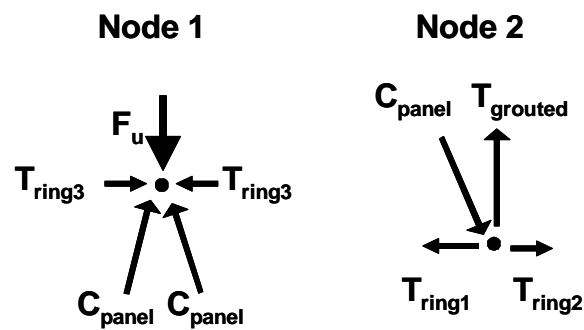


Figure B. 17 Equilibrium of Nodes 1 and 2 in truss model.

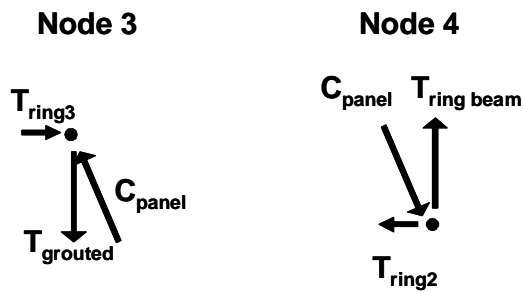


Figure B. 18 Equilibrium of Nodes 3 and 4 in truss model.

Based on equilibrium

$$C_{panel} = 9045 \text{ lb}$$

$$T_{gouted\ key} = 9000 \text{ lb}$$

$$T_{ring1} = 1800 \text{ lb}$$

$$T_{ring2} = 900 \text{ lb}$$

$$T_{ring3} = -900 \text{ lb (Compression)}$$

$$T_{ring\ beam} = 9000 \text{ lb}$$

Check capacity of Node 1: location of concentrated load plus compressive struts and compressive forces in ring beam based on ACI 318-11, Section A.5.1. Use  $\beta_n = 1$  when evaluating the calculated effective stress of the nodal zone because confining cages are present at this node.

The compressive capacity of panel strut

$w_{strut} = 6 \text{ in.}$  (This is one-quarter of the panel width based on experimental results.)

$$T_{panel} = 7.87 \text{ in.}$$

$$C_{panel} = 9045 \text{ lb} < \phi F_{nn} = \phi f_{ce} A_{nz} = 0.75(0.85\beta_n f'_{AAC}) W_{strut} T_{panel} =$$

$$0.75(0.85)(1)(580)(6)(7.87) = 17,460 \text{ lb OK}$$

Check capacity of Node 2: Although three tension ties are located here, they are contained within a confining cage. Use  $\beta_n = 1$ .

$$T_{grouted \text{ key}} = 9000 \text{ lb} < \phi A_s f_y \beta_n = 0.75(0.31)(60,000)1 = 13,950 \text{ lb OK}$$

$$C_{panel} = 9045 \text{ lb} < \phi F_{nn} = \phi f_{ce} A_{nz} = 0.75(0.85\beta_n f'_{AAC}) W_{strut} T_{panel} =$$

$$0.75(0.85)(1)(580)(6)(7.87) = 17,460 \text{ lb OK}$$

$T_{ring1}$  and  $T_{ring2}$  do not control.

Check capacity of Node 3: As with Node 2, the tension ties are contained within a confining cage. Use  $\beta_n = 1$ .

$$T_{grouted \text{ key}} = 9000 \text{ lb} < \phi A_s f_y \beta_n = 0.75(0.31)(60,000)1 = 13,950 \text{ lb OK}$$

$T_{ring1}$  and  $T_{ring2}$  do not control.

Check capacity of Node 4: Unlike the other nodes, a confining cage is not present.

Both tension ties are within the grouted key, so two reinforcing bars are present.

Use  $\beta_n = 0.6$  because two ties are anchored at Node 4.

$$T_{ring \text{ beam}} = 9000 \text{ lb} < \phi A_s f_y \beta_n = 0.75(2)(0.31)(60,000)0.6 = 16,740 \text{ lb OK}$$

Compressive capacity of panel strut

$$C_{panel} = 9045 \text{ lb} < \phi F_{nn} = \phi f_{ce} A_{nz} = 0.75(0.85\beta_n f'_{AAC}) w_{strut} T_{panel} =$$

$$0.75(0.85)(0.6)(580)(6)(7.87) = 10,480 \text{ lb OK}$$

**Example 4: Design of load-bearing vertical wall panel subjected to eccentric gravity and out-of-plane wind loads**

Use AAC4

$$f'_{AAC} = 580 \text{ psi}$$

$$f_y = 80,000 \text{ psi}$$

$$q = 60 \text{ psf}$$

density = 44 lb/ft<sup>3</sup> (with reinforcement)

$$\text{Weight} = (44 \text{ lb/ft}^3) \left( \frac{7.87 \text{ in.}}{12 \text{ in./ft}} \right)$$

$$\text{Weight} = 28.9 \text{ lb/ft}^2$$

Use 0.236 in. (6 mm ) bars for longitudinal steel and transverse steel with 1 in. clear cover.

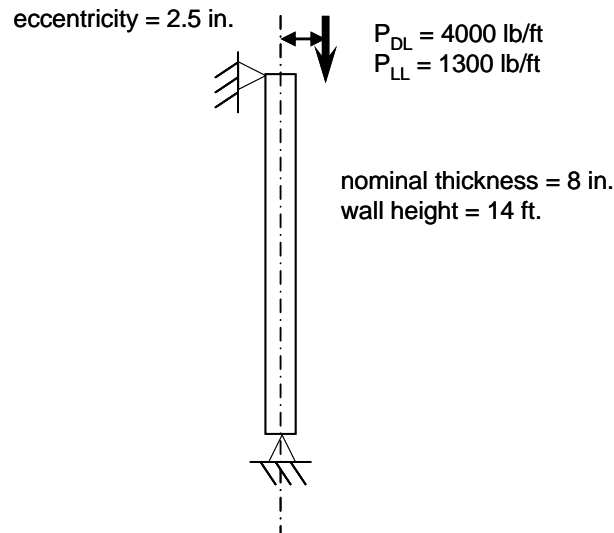


Figure B. 19 Section of AAC bearing wall to be designed

Because flexural capacity increases with axial load and wind loads are much higher than gravity loads, the most critical loading combination is likely  $0.9D + 1.0W$ . Designers should check all critical loading combinations.

$$M_{wind} = \frac{wh^2}{8} = \frac{(60 \text{ lb/ft}^2)(14 \text{ ft})^2}{8} (12 \text{ in./ft}) = 17,640 \text{ lb-in./ft}$$

$$M_{DL}(\text{mid-height}) = \frac{Pe}{2} = \frac{(4000 \text{ lb/ft})(2.5 \text{ in.})}{2} = 5000 \text{ lb-in./ft}$$

$$M_u = 0.9D + 1.0W = 0.9(5000 \text{ lb-in./ft}) + 1.0(17,640 \text{ lb-in./ft}) = 22,140 \text{ lb-in./ft}$$

$$P_u(\text{mid-height}) = 0.9(4000 \text{ lb/ft}) + 0.9\left(\frac{14 \text{ ft}}{2}\right)(28.9 \text{ lb/ft}^2) = 3782 \text{ lb/ft}$$

Check slenderness:

$$\frac{kh}{r} = \frac{h}{r} = \frac{(14\text{ft})(12 \text{ in./ft})}{\frac{7.87 \text{ in.}}{\sqrt{12}}} = \frac{168 \text{ in.}}{2.27 \text{ in.}} = 73.9 < 99$$

$$\therefore \text{Factor} = \left[1 - \left(\frac{h}{140r}\right)\right]^2 = \left[1 - \left(\frac{168 \text{ in.}}{140(2.27 \text{ in.})}\right)\right]^2 = 0.721$$

This slenderness factor affects the pure axial capacity of the panel as defined in ACI 530/530.1. The interaction diagram will be capped at a value of  $0.721P_n$ .

Continue with factored design actions:

$$P_u = 3782 \text{ lb/ft} \quad \text{and} \quad M_u = 22,140 \text{ lb-in./ft}$$

Construct moment interaction diagram:

Consider two 0.236 in.(6 mm) bars for longitudinal steel. Use 1 in. clear cover.

$$A_{\text{bar}} = 0.049 \text{ in.}^2/\text{bar}$$

$$A_s = (0.049)(2 \text{ bars/ft}) = 0.098 \text{ in.}^2/\text{ft}$$

$$d = h - \text{cover} - \frac{d_b}{2} = 7.87 \text{ in.} - 1 \text{ in.} - 0.12 \text{ in.} = 6.75 \text{ in.}$$

$$A_{smin} = \frac{4\sqrt{f'_{AAC}} b_w d}{f_y} = \frac{4\sqrt{580} \cdot 12 \text{ in.} \cdot 6.75 \text{ in.}}{80,000} = 0.0975 \text{ in.}^2 \quad \text{OK}$$

Compare factored loads with strength interaction diagram:

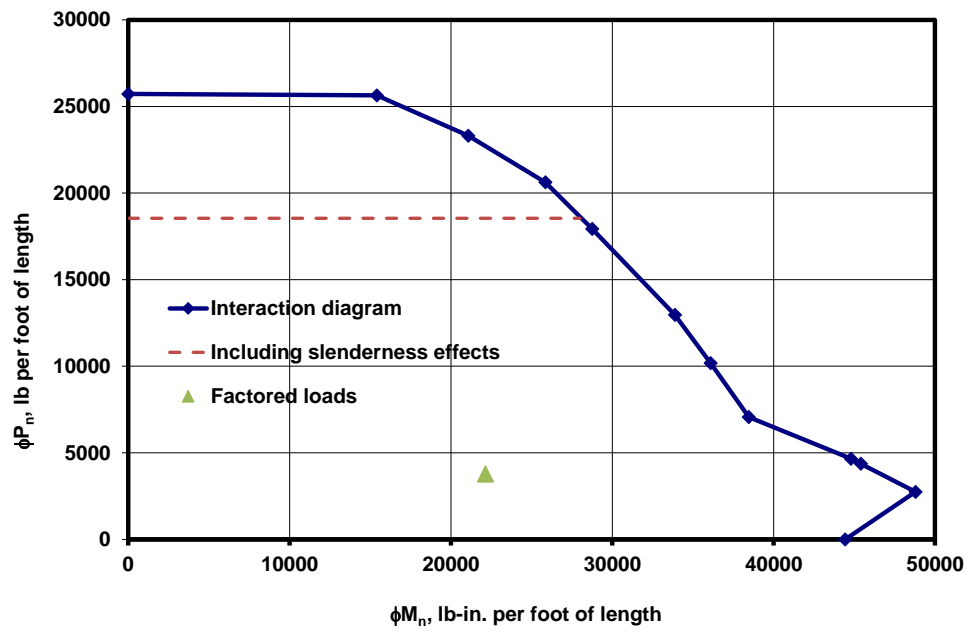


Figure B. 20 force interaction for 8 in. nominal AAC is bearing wall with two 0.236 in. (6 mm) diameter bars as longitudinal reinforcement.

Table B. 1 Values for interaction diagram

	$c/d$	$c$	$C_{AAC}$	$f_s$	$\phi$	$\phi M_n$	$\phi P_n$	$\phi P_u$ with 0.721 cap
Points controlled by steel	0.01	0.0696	276	– 80,000	0.90	22,316	–6808	–6808
	0.1	0.696	2759	– 80,000	0.90	30,536	–4573	–4573
	0.2	1.392	5517	– 80,000	0.90	38,569	–2090	–2090
	0.2842	1.978	7840	– 80,000	0.90	44,435	0	0
	0.4	2.784	11,035	– 80,000	0.86	48,794	2742	2742
	0.5	3.48	13,794	– 80,000	0.73	45,403	4366	4366
	0.521	3.626	14,372	– 80,000	0.71	44,799	4659	4659
Points controlled by AAC	0.600	4.176	16,552	– 58,000	0.65	38,462	7065	7065
	0.7	4.872	19,311	– 37,286	0.65	36,091	10,177	10,177
	0.8	5.568	22,070	– 21,750	0.65	33,882	12,960	12,960
	1	6.96	27,587	0	0.65	28,752	17,932	17,932
	1.15	8.004	31,726	0	0.65	25,853	20,622	18,547
	1.3	9.048	35,864	0	0.65	21,072	23,311	18,547
	1.43	9.9528	39,450	0	0.65	15,406	25,643	18,547
pure axial load						0	25,724	18,547

Critical actions at midheight of the wall:

$$P_u = 3782 \text{ lb/ft and } M_u = 22,140 \text{ lb-in./ft}$$

Action is inside moment-axial force interaction, and the design is satisfactory if P-delta effects are not considered.

Check secondary moments based on 11.3.5.5 (P-delta effect):

Determine if  $M_u < M_{cr}$

Evaluate section properties for this panel section assuming that it is uncracked.

$$f_t = 2 \cdot 2.4 \sqrt{f'_{AAC}} = 2 \cdot 2.4 \sqrt{580 \text{ lb/in.}^2} = 115.6 \text{ lb/in.}^2$$

$$f_r + \frac{P_u}{A} = 115.6 + \frac{3782 \text{ lb}}{12 \cdot 7.87 \text{ in.}^2} = 155.6 \text{ psi}$$

Determine uncracked transformed  $I_{ut}$  and  $M_{cr}$ :

$$E_{AAC} = 6500(f'_{AAC})^{0.6} = 6500(580)^{0.6} = 295,800 \text{ lb/in.}^2$$

$$n = \frac{E_s}{E_{AAC}} = \frac{29,000,000 \text{ psi}}{296,000 \text{ psi}} = 98.0$$

$$A_s = 0.049 \text{ in.}^2/\text{bar}$$

$$nA_s = (0.049)(2 \text{ bars/ft})(98.0) = 9.61 \text{ in.}^2/\text{ft}$$

Because compression steel is laterally unsupported, neglect this in calculations. Continue to calculate the uncracked transformed moment of inertia about the neutral axis.

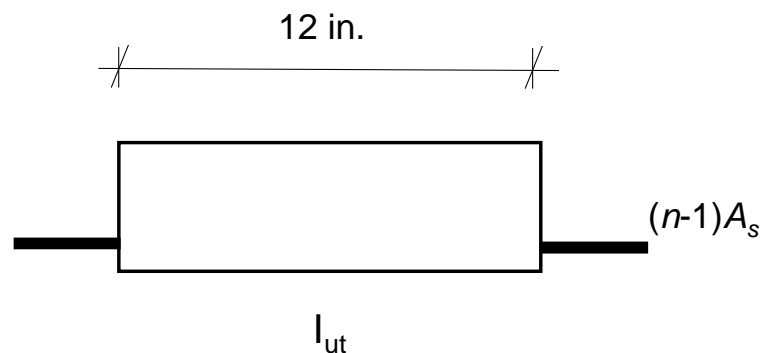


Figure B. 21 Horizontal section through 1 ft wide strip of uncracked AAC bearing wall.

$$d = h - \text{cover} - \frac{d_b}{2} = 7.87 \text{ in.} - 1 \text{ in.} - 0.118 \text{ in.} = 6.75 \text{ in.}$$

$$I_{ut} = \frac{bh^3}{12} + \left[ (n-1)A_s \left( \frac{h}{2} - d_c \right)^2 \right]$$

$$I_{ut} = \frac{12 \text{ in./ft} \times (7.87 \text{ in.})^3}{12} + \left[ 9.51 \text{ in.}^2/\text{ft} \left( \frac{7.87}{2} - 1.118 \text{ in.} \right)^2 \right]$$

$$I_{ut} = 562.9 \text{ in.}^4/\text{ft}$$

$$M_{cr} = \left[ \frac{I_{ut}}{h/2} \right] \left[ f_{rAAC} + \frac{P_u}{A} \right] = \frac{(562.9 \text{ in.}^4/\text{ft})}{7.87 \text{ in.}/2} \left[ 115.6 \text{ psi} + \frac{3782 \text{ lb}}{12 \cdot 7.87 \text{ in.}^2} \right] = 21,990 \text{ lb-in./ft}$$

Because of  $M_u > M_{cr}$ , calculate and use the cracked transformed moment of inertia.

Locate neutral axis and calculate transformed a moment of inertia:

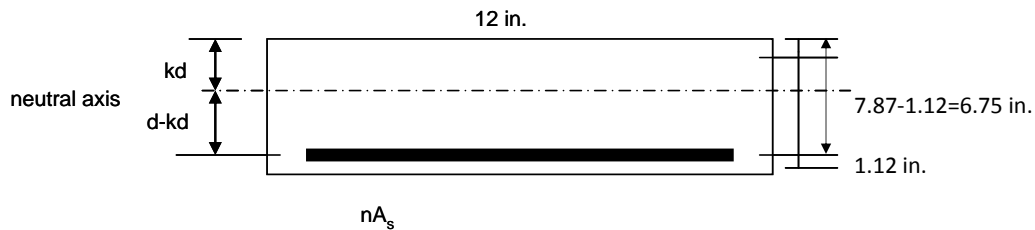


Figure B. 22 Horizontal section through 1 ft wide strip of cracked AAC bearing wall.

Now that the section is cracked use  $nA_s$  to solve for the neutral axis.

$$(bkd) \left( \frac{kd}{2} \right) = nA_s (d - kd)$$

$$k^2 + 2n\rho k - 2n\rho = 0$$

$$k = -n\rho \pm \sqrt{n^2\rho^2 + 2n\rho}$$

In this case,

$$\rho = \frac{A_s}{bd} = \frac{2 \cdot 0.049 \text{ in.}^2}{12 \text{ in.} \cdot 6.75 \text{ in.}} = 1.21 \cdot 10^{-3}$$

$$\rho n = 0.119$$

$$k = -0.119 \pm \sqrt{0.119^2 + 2 \times 0.119} = 0.383$$

$$kd = 0.383 \times 6.75 \text{ in.} = 2.584 \text{ in.}$$

$$I_{cr,t} = \frac{b(kd)^3}{3} + nA_s (d - kd)^2$$

$$I_{cr,t} = \frac{12 \times 2.584^3 \text{ in.}^4/\text{ft}}{3} + 9.608 \text{ in.}^2/\text{ft} (6.75 \text{ in.} - 2.584 \text{ in.})^2$$

$$I_{cr,t} = 235.8 \text{ in.}^4/\text{ft}$$

Use the moment magnifier approach to determine the moment due to P-delta effects:

Based on ACI 530/530.1

$$P_e = \frac{\pi^2 E_{AAC} I_{cr}}{h^2} = \frac{3.14^2 \cdot 296,000 \text{ psi} \cdot 235.8 \text{ in}^4/\text{ft}}{(168 \text{ in.})^2} = 24,390 \text{ l}$$

$$\Psi = \frac{1}{1 - \frac{P_u}{P_e}} = \frac{1}{1 - \frac{3782 \text{ lb}}{24,390 \text{ lb}}} = 1.184$$

$$M_u = \Psi M_{u,0} = 1.184 \cdot 22,140 \text{ lb-in.} = 26,200 \text{ lb-in.}$$

Even with P-delta effects, the factored loads are still within the interaction diagram.

Determine anchorage requirements for reinforcing steel:

$$M_u = 26,200 \text{ lb-in./ft}$$

$$T = A_s f_y = 0.098 \text{ in.}^2/\text{ft} (80,000 \text{ lb/in.}^2) = 7840 \text{ lb/ft}$$

$$T = C = 0.85 f'_{AAC} a b_w = 0.85(580 \text{ lb/in.}^2) a (12 \text{ in./ft}) = 5916 a \cdot \text{lb/in-ft}$$

$$a = \frac{7840}{5916 \text{ lb}} = 1.325 \text{ in.}$$

Because the internal AAC reinforcement is smooth, the bond is developed by bearing on the cross wires. Calculate a number of cross wires required to develop a tensile force of  $T = 7840 \text{ lb}$  in a 1 ft wide strip:

$$T_{demand} = \frac{T_u}{\phi} = \frac{7840}{0.9} = 8710 \text{ lb/ft}$$

Consider a total of 10 cross wires or five in each half of the panel based on Eq. (7.2.1b).

Each cross wire has a 0.157 in. (4 mm) diameter and length of 22 in.

$$T_{capacity} = n_{cross} d_{cross} l_{cross} f'_{AAC} = 5 \cdot 0.157 \cdot 22 \cdot 580 = 10,020 \text{ lb}$$

Based on 7.2.3, at least 50 percent of the cross wires should be located in each end zone.

For this design, three cross wires are required in the end zone, and another two are required between the end zone and the center of the panel.

$$\text{Length of end zone} = 2h = 2(7.87 \text{ in.}) = 15.7 \text{ in.}$$

Shear capacity:

Because most of the shear comes from wind, use  $0.9D + 1.0W$  load combination.

$$V_{wind} = \frac{1}{2} \times 60 \text{ lb/ft}^2 \times 14 \text{ ft} = 420 \text{ lb/ft}$$

$$V_{eccentric} = \frac{Pe}{\ell} = \frac{(4000 \text{ lb/ft})(2.5 \text{ in.})}{14 \text{ ft} \times 12 \text{ in./ft}} = 59.5 \text{ lb/ft}$$

$$V_u = 0.9D + 1.0W = 0.9(59.5 \text{ lb/ft}) + 1.0(420 \text{ lb/ft}) = 474 \text{ lb/ft}$$

$$V_n = 0.8\sqrt{f'_{AAC}}bd = 0.8\sqrt{5800 \text{ psi}} \cdot 12 \text{ in.} \cdot 6.75 \text{ in.} = 1619 \text{ lb} \quad \text{Eq. (7.5.1c)}$$

$$\phi V_n = 0.75 \cdot 1619 \text{ lb} = 1214 \text{ lb}$$

$$V_u = 474 \text{ lb} < \phi V_n = 0.75 \cdot 1619 \text{ lb} = 1214 \text{ lb}$$

Shear capacity is satisfactory.

Check deflections at service level loads:

Because lateral loads are not sustained loads, neglect long-term creep. Use long-term creep factor = 0. Evaluate service level moments at midheight of the wall. In this case, deflections due to eccentric gravity loads are larger than wind, the critical load. Because wind load is significantly higher than gravity loads, the most extreme load combination is  $D + 0.6W$ . Designers should consider alternate load cases such as  $D + 0.75L' + 0.75(0.6W)$ .

$$M_{wind} = 0.6 \cdot 17,640 \text{ lb-in./ft}$$

$$M_{DL} = 5000 \text{ lb-in./ft} \quad \text{Dead load moment at midheight of the wall.}$$

$$M_a = 0.6(M_{wind}) + M_{DL} = 0.6(17,640) + 5000 = 15,580 \text{ lb-in./ft}$$

$$M_a = 15,580 \text{ lb-in./ft} < 22,020 \text{ lb-in./ft} = M_{cr}$$

Use uncracked transformed moment of inertia,  $I_{ut}$ .

$$\delta = \frac{5w\ell^4}{384E_{AAC}I_{eff}} + \frac{Pe\ell^2}{16E_{AAC}I_{eff}}$$

$$\delta = \frac{0.6 \cdot 5 \cdot 60 \text{ lb/ft}^2 \cdot 14^4 \text{ ft}^4 \cdot 1728 \text{ in.}^3/\text{ft}^3}{384 \cdot 295,780 \cdot 563.7 \text{ lb-in.}^2/\text{ft}} + \frac{5000 \text{ lb in.} \cdot (14 \text{ ft} \cdot 12 \text{ in./ft})^2}{16 \cdot 295,780 \cdot 563.7 \text{ lb-in.}^2/\text{ft}}$$

$$\delta = 0.187 + 0.053 = 0.24 \text{ in.}$$

$$\delta_{allow} = \frac{\ell}{240} = \frac{14 \text{ ft} \cdot 12 \text{ in./ft}}{240} = 0.70 \text{ in.}$$

$$\delta = 0.24 \text{ in.} < 0.70 \text{ in.} = \delta_{allow}$$

Deflection is satisfactory.